SYSTEM IDENTIFICATION AND MODELING OF GYRO-STABILIZED IR/EO GIMBAL SYSTEM IN FREQUENCY DOMAIN

A THESIS SUBMITTED TO
THE GRADUATE SCHOOL OF NATURAL AND APPLIED SCIENCES
OF
MIDDLE EAST TECHNICAL UNIVERSITY

BY

GÖKHAN ÖZDOĞAN

IN PARTIAL FULFILLMENT OF THE REQUIREMENTS
FOR
THE DEGREE OF MASTER OF SCIENCE
IN
ELECTRICAL AND ELECTRONICS ENGINEERING

JULY 2014

Approval of the thesis:

SYSTEM IDENTIFICATION AND MODELING OF GYRO-STABILIZED IR/EO GIMBAL SYSTEM IN FREQUENCY DOMAIN

submitted by **GÖKHAN ÖZDOĞAN** in partial fulfillment of the requirements for the degree of **Master of Science in Electrical and Electronics Engineering Department, Middle East Technical University** by,

Prof. Dr. Canan Özgen _____
Dean, Graduate School of **Natural and Applied Sciences**

Prof. Dr. Gönül Turhan Sayan _____
Head of Department, **Electrical and Electronics Engineering**

Prof. Dr. Kemal Leblebicioğlu _____
Supervisor, **Electrical and Electronics Eng. Dept., METU**

Examining Committee Members:

Prof. Dr. Kemal Özgören
Mechanical Engineering Dept., METU _____

Prof. Dr. Kemal Leblebicioğlu
Electrical and Electronics Engineering Dept., METU _____

Prof. Dr. Gülbin Dural Ünver
Electrical and Electronics Engineering Dept., METU _____

Prof. Dr. Tolga Çiloğlu
Electrical and Electronics Engineering Dept., METU _____

Dr. Oğuzhan Çifdalöz
MGEO, ASELSAN _____

Date: _____

I hereby declare that all information in this document has been obtained and presented in accordance with academic rules and ethical conduct. I also declare that, as required by these rules and conduct, I have fully cited and referenced all material and results that are not original to this work.

Name, Last Name: GÖKHAN ÖZDOĞAN

Signature :

ABSTRACT

SYSTEM IDENTIFICATION AND MODELING OF GYRO-STABILIZED IR/EO GIMBAL SYSTEM IN FREQUENCY DOMAIN

Özdoğan, Gökhan
M.S., Department of Electrical and Electronics Engineering
Supervisor : Prof. Dr. Kemal Leblebicioğlu

July 2014, 115 pages

The field of system identification takes a fundamental place in control engineering. In order to design an efficient robust controller, one requires an accurate mathematical model with its uncertainty for the dynamical system of interest. It is crucial that experiments are well designed so that parameters to be estimated through statistical methods result in least possible bias and minimum variance.

In this study, four axis gyro stabilized Infrared Electro Optic gimbal system is modeled in the frequency domain through experimental investigation. The input and output signals are logged using xPC Target of MATLAB with a sampling frequency of 3kHz. The communication with real system is realized with RS-422 protocol.

In system identification, the first step is experiment design. Various perturbation signals are analyzed and compared. A cost function is offered to optimize power spectrum for the input excitation signal while satisfying device specific constraints. Second step is frequency response function measurement. By averaging techniques, it is possible to reduce the variance of frequency response function measurement and

decrease the error. Moreover, the averaging in the frequency domain provides the nonparametric noise model of the system. Periodic excitation signals are used and an integer number of signal periods have been measured. Before passing to the next step, a robust method to detect and quantify nonlinear distortion on frequency response functions measurements is studied. In the final step, real system is modeled by its parametric transfer function with plenty of different estimation techniques and their efficiencies, convergence properties, bias errors are compared and discussed.

Keywords: System identification, excitation signal design, frequency response function measurement, nonparametric noise model, nonlinearity detection, gyro stabilized gimbal

ÖZ

CAYRO İLE KARARLILAŞTIRILMIŞ IR/EO GİMBAL SİSTEMİNİN FREKANS BÖLGESİNDE MODELLENMESİ

Özdoğan, Gökhan
Yüksek Lisans, Elektrik ve Elektronik Mühendisliği Bölümü
Tez Yöneticisi : Prof. Dr. Kemal Leblebicioğlu

Temmuz 2014 , 115 sayfa

Sistem tanılama, kontrol mühendisliğinde önemli bir yer tutar. Gürbüz bir kontrolcü tasarlayabilmek için, dinamik sistemin hassas bir matematiksel modeline ve bu modelin belirsizlik bilgisine ihtiyaç duyulmaktadır. Frekans tepki fonksiyonu ölçüm düzeneğinin ve uyarı sinyalinin iyi tasarlanması, parametrik model kestirimindeki sistematik hataların ve varyansın minimize edilebilmesi için çok önemlidir.

Bu çalışmada, cayro ile stabilize edilmiş dört eksen gimbal yapılı elektro optik sistem, frekans bölgesinde deneysel yöntemlerle adım adım modellenmiş, çalışmanın sonuçları sunulmuştur. Girdi ve çıktı sinyalleri, MATLAB'ın xPC Target araç seti kullanılarak, 3kHz örnekleme frekansında kaydedilmiştir. Gerçek sistem ile haberleşme, RS-422 protokolü ile gerçekleştirilmiştir.

Sistem tanılanması çalışmasında, ilk adım, deney düzeneğinin hazırlanmasıdır. Uyarı sinyalleri çeşitlerinin analizi ve karşılaştırılması yapılmıştır. Uyarı sinyalinin güç spektrumunu, cihaza özgü kıstasları ihlal etmeden, ilgilenilen frekans aralığında optimize

etmek için bir maliyet fonksiyonu önerilmiştir. İkinci adım, frekans tepki fonksiyonu ölçümüdür. Ortalama alma yöntemleri ile, frekans tepki fonksiyonu ölçümündeki varyansı ve hatayı düşürmek mümkündür. Buna ek olarak, frekans bölgesinde gerçekleştirilen ortalama alma teknikleri, frekans tepki fonksiyonu ölçümündeki parametrik olmayan gürültü modelinin elde edilmesini sağlar. Bu çalışmada periyodik uyarı sinyalleri tercih edilmiş ve zaman bölgesinde periyodun tam sayı katı süre ölçüm gerçekleştirilmiştir. Bir sonraki adıma geçmeden önce, frekans tepki fonksiyonu ölçümlerindeki doğrusal olmayan bozulmaları tespit eden gürbüz bir metod çalışılmıştır. Son adımda, gerçek sistem, parametrik transfer fonksiyon ile birçok farklı kestirim yöntemi ile modellenmiş, bu kestirim yöntemlerinin yakınsama özellikleri ve sabit hataları karşılaştırılmış, tartışılmıştır.

Anahtar Kelimeler: Sistem tanılama, uyarı sinyali tasarımı, frekans tepki fonksiyonu ölçümü, parametrik olmayan gürültü modeli, doğrusal olmayan bozulma tespiti, cayro stabilize gimbal

To

My Beloved Family, Grandparents and Fiancée

ACKNOWLEDGMENTS

I would like to express my special thanks to my supervisor Prof. Dr. Kemal Leblebicioğlu for his priceless guidance and valuable comments throughout this study. His knowledge, teachings and effective feedbacks helped me to complete this work.

I am also grateful to my co-workers in ASELSAN, Akın Günönü, Murat Kalkan and Kadir Hakan Biçer for their advices, criticism and encouragements towards the realization of this thesis work, Murat Müminoğlu for helping out with xPC Target setup and Dr. Oğuzhan Çifdalöz for introducing the beautiful typesetting system, LaTeX.

I am very grateful to my family for their endless support not only during my thesis preparation, but also throughout my life.

Finally, I would like to thank my love and future wife, Sinem, for her great support and understanding at every stage of this study. Without her endless support, I could not finish this work.

TABLE OF CONTENTS

LIST OF FIGURES

FIGURES

LIST OF SYMBOLS

$\mathbb{N}$	The set of natural numbers
$\mathbb{Z}$	The set of integer numbers
$\mathbb{Q}$	The set of rational numbers
$\mathbb{R}$	The set of real numbers
$\mathbb{C}$	The set of complex numbers
$\lim_{x \to p} f(x) = L$	The limit of f, as x approaches p, is L
$O(x)$	Big O notation, describing the limiting behavior of an arbitrary function when the argument x tends to 0. The limiting behavior has the property $\lim_{x \to 0} \lvert O(x)/x \rvert < \infty$
subscript 0	True value
superscript T	Matrix transpose
superscript H	Complex conjugate matrix transpose
superscript $-$	Inverse of the square matrix
$x^{[l]}$	lth realization of a random process x
$Re()$	Real part of the complex number
$Im()$	Imaginary part of the complex number
$\lvert A \rvert$	$\sqrt{(Re(A))^2 + (Im(A))^2}$, magnitude of a complex number A
$\underline{/A}$	Phase of the complex number A
$\lVert A \rVert_p$	p-norm
$\bar{x}$	Denotes the complex conjugate of x
$\hat{x}$	The estimated value of x
$\mathbb{E}\{x\}$	Mathematical expectation of random vector x
$\mu_x = \mathbb{E}\{x\}$	Mean value of x
$\hat{x} = \frac{1}{M} \sum_{m=1}^{M} x^{[m]}$	Sample mean of M realizations (experiments) of x
$var(x)$	$\mathbb{E}\{\lvert x - \mathbb{E}\{x\} \rvert^2\}$, variance of x
$\sigma_x^2 = var(x)$	Variance of the x
$\hat{\sigma}_x^2 = \frac{1}{M-1} \sum_{m=1}^{M} \lvert x^{[m]} - \hat{x} \rvert^2$	Sample variance of M realizations of x
$covar(x, y)$	$\mathbb{E}\{(x - \mathbb{E}\{x\})(y - \mathbb{E}\{y\})\}$, covariance of x and y

$\sigma_{xy}^2 = covar(x, y)$	Covariance of the x and y
$\hat{\sigma}_{xy}^2 = \frac{1}{M-1} \sum_{m=1}^{M} (x^{[m]} - \hat{x})\overline{(y^{[m]} - \hat{y})}$	Sample covariance of M realizations of x and y
s	Laplace transform variable
z	Z-transform variable
t	Continuous or discrete time variable
Ω	Generalized transform variable: Laplace domain $\Omega = s$, Z-domain $\Omega = z^{-1}$
Ω_k	Generalized transform variable evaluated at DFT frequency k: Laplace domain $\Omega_k = j\omega_k$, Z-domain $\Omega_k = e^{-j\omega_k T_s}$
$DFT(x(t))$	Discrete Fourier transform of the samples $x(t)$, $t = 1, 2, \ldots, N-1$ (See definition 3.3.1)
$E(k)$	Discrete Fourier transform of the samples $e(tT_s)$, $t = 0, 1, \ldots, N-1$
f	Frequency
M	Number of repeated experiments
f_s	Sampling frequency of the system
T_s	Sampling time of the system
f_0	Frequency resolution of the frequency response function (FRF) measurement
T_0	Excitation signal period
T_w	Waiting time for frequency response function (FRF) measurement system to reduce transient effects below to noise level
T	Transient free measurement duration
L	Length of the transient free measurement signal
F	Number of frequency domain data samples
τ	Time delay
$\omega = 2\pi f$	Angular frequency
$u(t),\ y(t)$	Input and output time signals of the system
$U(e^{j\omega T_s}),\ Y(e^{j\omega T_s})$	Fourier transform of $u(tT_s)$ and $y(tT_s)$
$U(k),\ Y(k)$	Discrete Fourier transform of the samples $u(tT_s)$ and $y(tT_s)$, $t = 1, 2, \ldots, N-1$ (See definition 3.3.1)
$U(j\omega),\ Y(j\omega)$	Fourier transform of $u(t)$ and $y(t)$
$U(s),\ Y(s)$	One-sided Laplace transform of $u(t)$ and $y(t)$

$n_u(t),\ n_y(t)$	Time domain noise signals on input and output respectively.
$N_u(k),\ N_y(k)$	Discrete Fourier transform of $n_u(t)$ and $n_y(t)$
$Cr(u)$	Crest factor of the signal $u(t)$ (See section 3.2)
$G(j\omega)$	Frequency response function
G_{BLA}	Best linear approximation of a nonlinear system (See section 5.4)
$G_0(j\omega_k)$	The transfer function of true underlying linear system (See section 5.4)
$G_B(j\omega_k)$	The bias or systematic, deterministic nonlinear contributions independent of the phases of the input signal (See section 5.4)
$G_S(j\omega_k)$	Stochastic nonlinear contribution (See section 5.4)
θ	Vector of plant model parameters (see Equations 6.3, 6.6)
$A(\Omega,\theta) = \sum_{r=0}^{n_a} a_r \Omega^r$	Denominator polynomial plant model
$B(\Omega,\theta) = \sum_{r=0}^{n_b} b_r \Omega^r$	Numerator polynomial plant model
$G(\Omega,\theta) = \dfrac{B(\Omega,\theta)}{A(\Omega,\theta)}$	Parametric plant model (See Eqn. 6.2)
$n_a,\ n_b$	Order of the polynomials $A(\Omega,\theta)$ and $B(\Omega,\theta)$
n_θ	Dimension of the parameter vector θ
$Z(k) = \begin{bmatrix} Y(k) & U(k) \end{bmatrix}$	Data vector, measured input-output DFT spectra
$V(\theta, Z)$	Cost function

LIST OF ABBREVIATIONS

BLA	Best Linear Approximation
DFT	Discrete Fourier Transform
EO	Electro-Optic
FFT	Fast Fourier Transform
FRF	Frequency Response Function
HIL	Hardware-In-the-Loop
IMU	Inertial Measurement Unit
IR	Infrared
IWLS	Iterative Weighted Linear Least Squares
LOS	Line-of-Sight
LS[1]	Least Squares
LS[2]	Linear System
LTI	Linear Time-Invariant
MIMO	Multiple-Input, Multiple-Output
ML	Maximum Likelihood
NLS[1]	Nonlinear Least Squares
NLS[2]	Nonlinear System
NPR	Non-causal Power Ratio
pdf	probability density function
PRBS	Pseudo Random Binary Sequence
rms	root mean square value
SISO	Single Input, Single Output
SNR	Signal-to-Noise Ratio
ZOH	Zero-Order Hold

CHAPTER 1

INTRODUCTION

1.1 Background and Motivation

This study considers the very practical problem of system identification of an unknown dynamic system in the frequency domain. System identification is a common term in engineering which refers to the building of mathematical models of dynamical systems from measured noisy data by experiments. The field of system identification takes a fundamental place in control engineering.

Gimbal systems have a wide application area concerning the angular stabilization of camera, gun or telescope in an inertial coordinate system. For this study, the dynamic system chosen is the four axis gyro stabilized Infrared (IR) Electro-Optic gimbal system. Although all the experiments are realized using IR/EO gimbal system, the measurement techniques explained and identification methods discussed in this study are applicable to all SISO dynamic systems. This device under investigation is generally used to inertially stabilize an IR camera on moving platforms such as fighter aircrafts. Mechanical stabilization in inertial space is necessary to avoid blur and jitter in a thermal video image. In order to avoid blur and jitter, a good robust controller is required. In order to design an efficient robust controller, one requires an accurate mathematical model (parametric model, see Definition 1.1.2) with its uncertainty which best represents the dynamical system of interest. Mathematical models for dynamic systems are useful for time domain simulation, frequency domain analyses, controller design, stability analysis and prediction purposes. The necessity of mathematical models for these aforementioned purposes is the motivation of this study.

Mathematical models are obtained from measured noisy data by experiments describing the input-output relationship; strictly speaking, from nonparametric measurements (see Definition 1.1.1). The success of parametric system model estimation heavily depends on the quality of nonparametric measurements. Therefore, it is crucial that experiments are well designed so that parameters to be estimated through statistical methods result in least possible bias and minimum variance. All mechanical systems are inherently nonlinear in nature. However, nonlinear model building is difficult to accomplish and time consuming while the profits are usually small. For this reason, it is appealing to select a linear mathematical model around operating points. On the other hand, knowing the nonlinear distortion error contribution on the frequency response function (FRF) measurements helps the robust controller designer to set the uncertainty bounds on a linear model and improve the existing controller.

With the help of xPC Target, hardware-in-the-loop simulation is performed on the device under investigation. xPC Target is a MATLAB product which enables you to execute Simulink models on a target computer for hardware-in-the-loop (HIL) simulations, and other real-time testing applications. In this study, the experiments are realized and the input and output signals are logged in xPC Target environment. The communication with system is realized with RS-422 protocol and 921600 baud rate. Sampling time of the system is 3kHz.

Definition 1.1.1 (Nonparametric Model) *In the nonparametric model representation, the system is characterized by measurements of the frequency response at numerous frequencies. There is no relation between the measurements at various frequencies.*

Definition 1.1.2 (Parametric Model) *In a parametric model, the system is described using a finite number of parameters. An example of a parametric model is the transfer function of a filter described by its poles and zeros.*

1.2 Objectives, Contributions and Outline of the Thesis

The main objective of this study will be to measure nonparametric FRF and its uncertainty efficiently, quantify nonlinear distortions, apply various system identification

techniques and accurately model the plant. The plant under investigation is the inner azimuth gimbal of IR/EO four axis gyro stabilized gimbal system. The results of this study allows the control engineer to realize time domain simulations, frequency domain analyses, controller design, stability analysis and prediction.

There are several contributions of this study. First of all, the crest factors (see Definition 3.2 on page 17) and the FRF measurement qualities of several general purpose periodic broadband excitation signals are compared. The theoretical knowledge and practical experiences are shared in order to obtain best nonparametric measurements. As a original contribution, a new cost function is suggested for the optimization of excitation signal which best fits the specific application. Power spectrum of the excitation signals can be optimized in an offline study to achieve better SNR in the frequency band of interest while satisfying device specific constraints. Experimental illustrations of nonlinear distortion quantification techniques are given, summarizing their advantages and drawbacks. Several optimization techniques are implemented in order to find a parametric plant model which best represents dynamic system. The performances of the implemented identification techniques are compared in terms of their efficiencies, convergence properties and bias errors. It turns out that "Maximum Likelihood" estimator which weights the cost with respect to the nonparametric noise model, provides statistically better results.

System identification is an iterative process. A flowchart of the iterative system identification cycle is presented in Fig 1.1 (this flowchart is modified from reference [1]).

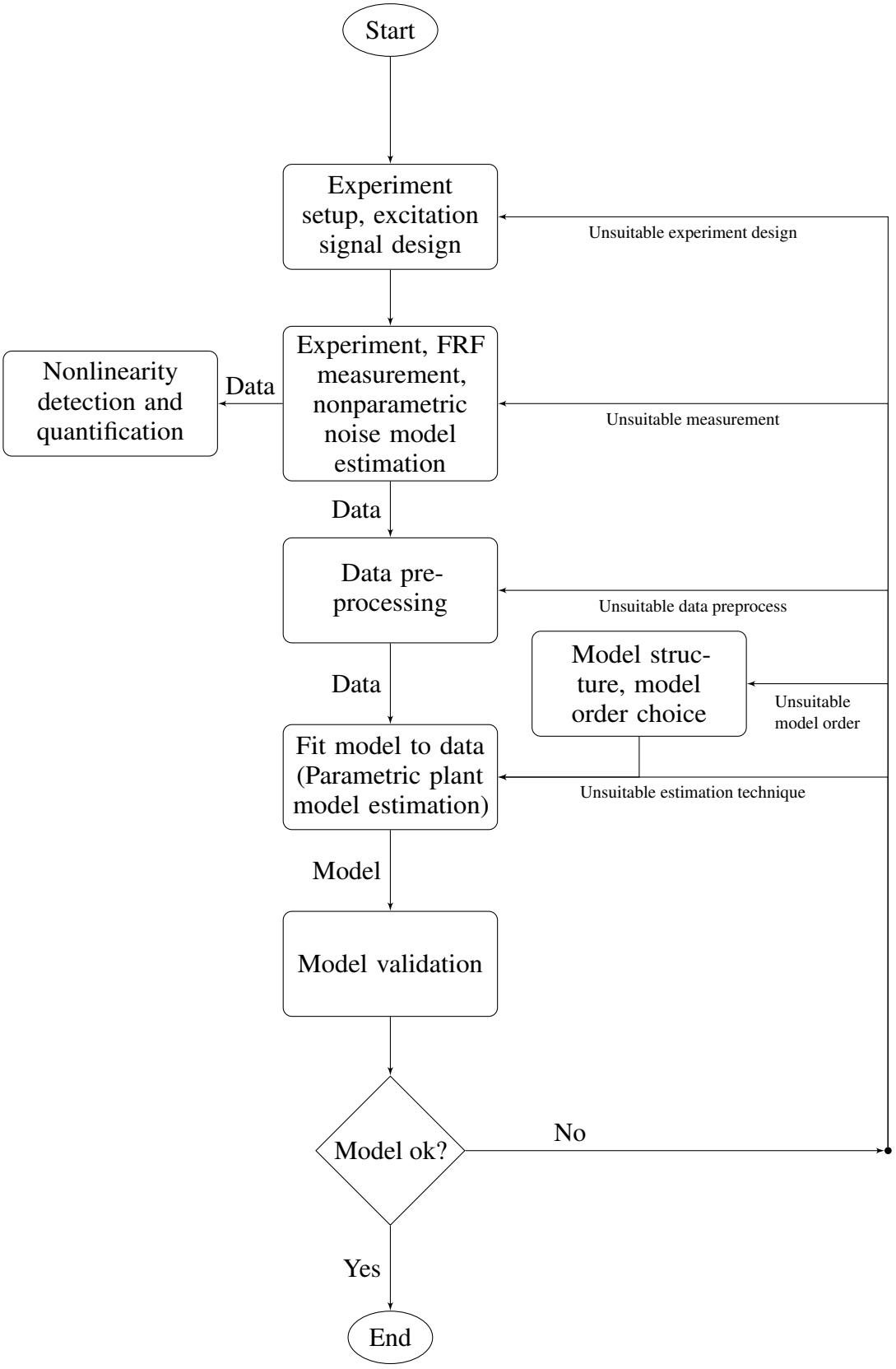

Figure 1.1: A schematic view of the system-identification cycle.

The organization of chapters in this study mainly follows the flowchart in Fig 1.1.

- Chapter 1 covers the background of the problem, motivation, main goal of the study and contributions.

- Chapter 2 introduces the device under investigation, explains the experimental setup and describe the big picture before diving into FRF measurement experiments and system identification algorithms. This chapter starts with the description of IR/EO four axis gimbal system. The mechanical implementation of excitation and measurement of output signal are explained. Device specific restrictions are mentioned which are highly critical when designing excitation signals in Chapter 3. Note that, although the device chosen here is a gimbal system, the measurement techniques explained and identification methods discussed in this study are applicable to all SISO dynamic systems operating in open loop.

- In Chapter 3, design of excitation signals are discussed. Crest factor property is introduced which is used to measure the quality of the excitation signal in terms of SNR. The broadband excitation signal and the stepped sine excitation signal are compared in terms of FRF measurement time to reach a specified accuracy. Three different broadband excitation signal categories are analyzed: transient signals, non-transient aperiodic signals and periodic signals. It turns out that the class of periodic excitation signals should be the first choice. Three general purpose periodic broadband excitation signals are designed which will be used in FRF measurement experiments in Chapter 4. Finally, an optimization procedure is suggested to achieve better SNR in the frequency band of interest while satisfying device specific constraints.

- In Chapter 4, nonparametric FRF measurements are studied. Averaging methods both in the time domain and in the frequency domain are given. The estimation of nonparametric noise spectrum is shown. Before realizing FRF measurements, system behavior is observed under zero input. The FRF measurement experiments designed in Chapter 3 are realized. Comparison of three experiments are given and discussed in detail.

- The aim of Chapter 5 is to detect and measure nonlinear distortions in FRF measurements. First, detection techniques for nonlinear distortions are discussed. Next, the class of perturbation signals used in this chapter are defined. Next, the theory of linear representations of nonlinear systems are given for continuous systems operating in open loop. A practical technique, called "Robust Method" for measuring the best linear approximation (BLA), its noise variance, and the level of nonlinear distortion is described. Finally, a robust method is applied on the real system and the experimental results are analyzed.

- Chapter 6 explains the parametric plant model used in Chapter 7. The parametric model discussed in this chapter is valid only for systems under periodic excitations. The relationship between input and output spectra for periodic signals is given. The parametric plant model definition with and without time delay, parameter vector and related notations are given. Lastly, the nonparametric noise model concept is discussed.

- Chapter 7 presents a case study of identification techniques in order to find a parametric model from the nonparametric measurements of Chapter 4. Search methods such as "Linear Least Squares", "Iterative Weighted Linear Least Squares" and "Genetic Algorithms" are implemented. After generating good starting values with one of those minimizers, efficient local minimum algorithms are studied to estimate better parametric plant models: "Nonlinear Least Squares", "Nonlinear Logarithmic Least Squares", "Maximum Likelihood". In each identification method, the estimated plant model and the measured FRF are compared by a visual inspection on a Bode plot and by residual analysis. The performances of all the identification techniques are compared in detail. This chapter ends with a discussion of model order selection and validation.

- Chapter 8 concludes the thesis with a brief summary, mentions the publications from this study and discusses some possible future work.

CHAPTER 2

DESCRIPTION OF THE DEVICE UNDER INVESTIGATION

2.1 Introduction

This chapter introduces the device under investigation, describes the experimental setup and describe the big picture before diving into FRF measurement experiments and system identification algorithms. Gimbal systems have a wide application area concerning the angular stabilization of camera, gun or telescope in the inertial coordinate system. For this study, the dynamic system chosen is a four axis gyro stabilized Infrared (IR) Electro-Optic gimbal system. This device is used to inertially stabilize the IR camera on the moving dynamic platforms such as fighter aircrafts. Inside the inner-most two axes, an IR camera and an IMU are mounted. Outer axes accomplish most of the angular positioning with their large rotational capacity, but possess low controller bandwidth. On the other hand, inner axes have few degrees of freedom but possess high controller bandwidth. Therefore, inner gimbals are used for fine tuning and hence efficient for angular stabilization of the IR camera in the inertial coordinate system. Stabilization of gimbal system removes the undesired rotational vibrations and holds the line-of-sight (LOS) of the camera steady. Although all the experiments are realized using IR/EO gimbal system, the measurement techniques explained and identification methods discussed in this study are applicable to all SISO dynamic systems operating in open loop.

This chapter starts with the description of experimental device in Section 2.2. The purpose of the gimbal system is stated and four axis gimbal mechanism is explained on a schematic figure. In this section, gimbal rotational mechanical limits are given.

Next, in Section 2.3 measurement setup is described. The reason of choosing inner azimuth gimbal as a case study is explained. The ideal transfer function and expected frequency response of the plant (inner azimuth gimbal) is given. The mechanical implementation of excitation signals, measurements of output signals, units of them and data logging platform are explained in detail. Digital system sampling frequency, the communication protocol and other used products such as xPC Target are mentioned. The differences between process noise and measurement noise are pointed out. Device specific restrictions are mentioned in Section 2.4 which are highly critical in the design of excitation signals.

2.2 IR/EO Four-Axis Gimbal System

In this study, the device under investigation is a four axis gyro stabilized Infrared (IR) Electro-Optic (EO) gimbal system. The purpose of this device is to perform inertial stabilization of an IR camera on moving platforms such as fighter aircrafts. Mechanical stabilization in inertial space is necessary to avoid blur and jitter in a thermal video image. The four axis gimbal mechanism has four links joined by revolute joints. A revolute joint provides one degree-of-freedom (single axis) rotation. Since gimbals are arranged in succession, the motion of outer most gimbal affects the angular positions of 2^{nd}, 3^{rd} and 4^{th} axes. The angular motion of 2^{nd} gimbal affects the 3^{rd} and 4^{th} gimbals and so on. Gimbal order from outer to inner is given in (2.1) and four axis gimbal schematic is sketched in Fig. 2.1.

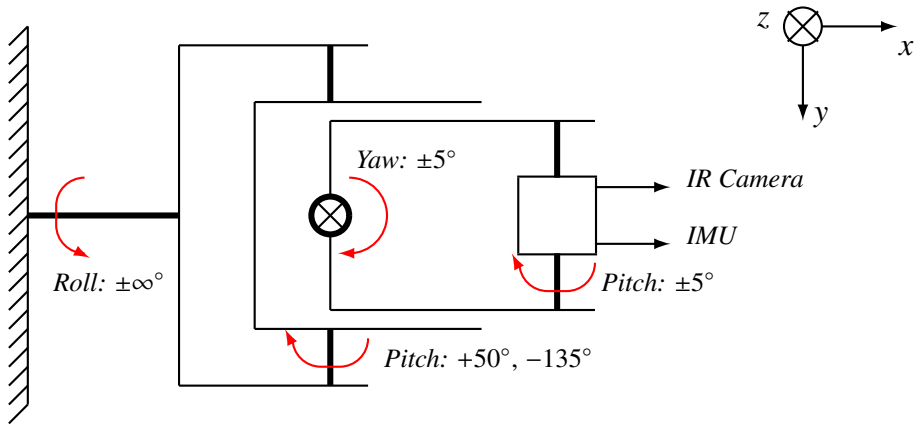

Figure 2.1: Gimbal schematics - Up view, the four joints are marked

$$Roll(\phi) \rightarrow OuterElevation(\theta_o) \rightarrow InnerAzimuth(\psi_i) \rightarrow InnerElevation(\theta_i) \tag{2.1}$$

Outer gimbals: Outer gimbals are roll gimbal and outer elevation gimbal. Roll gimbal has no mechanical constraint and can rotate 360° continuously. However outer elevation gimbal has mechanical limits between +50°, −135°. The angular positioning is mostly accomplished with outer gimbals since they have large rotational capacity. However, the controller bandwidth of outer gimbals are low and hence they are not effective for angular stabilization in inertial coordinate system.

Inner gimbals: Inner gimbals are inner azimuth gimbal and inner elevation gimbal. Both inner gimbals have angular mechanical limitations, ±5°. Due to this limited orientation capacity, they are ineffective for angular positioning. However, the controller bandwidth of inner gimbals are relatively much larger compared to outer gimbals and hence they are very much capable of performing angular stabilization inertially. There is an IMU next to IR camera which are located in inner gimbals (see Fig. 2.1). The azimuth gyro of IMU senses the rotational speed of the inner azimuth gimbal and the elevation gyro of IMU senses the rotational speed of the inner elevation gimbal (more details in Section 2.3).

2.3 Measurement Setup and SISO Plant

Experiment setup for FRF measurement is given in Fig. 2.2. Description of system, plant (inner azimuth gimbal) and related signals are given below.

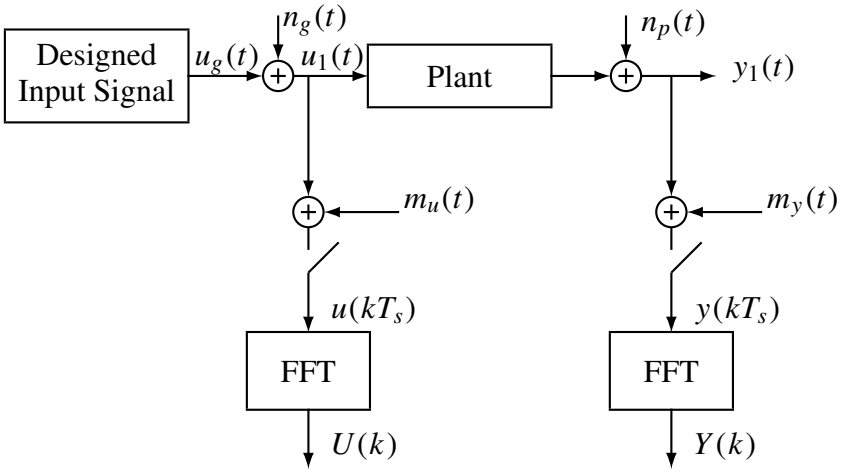

Figure 2.2: Measurement setup and notations for periodic signals

- ***Plant***: Device under investigation is a four axis gyro stabilized Infrared Electro Optic gimbal system. In this study, inner azimuth gimbal of the system is excited and frequency response function is measured. There are a few reasons for choosing the inner azimuth gimbal as a case study. Inner gimbal rotational speed sensors have more bandwidth than the outer gimbals. In addition, the inner azimuth gimbal has more interesting frequency response than the inner elevation gimbal frequency response (there is a mechanical resonance in the inner azimuth gimbal which will be observed in Chapter 4). Therefore, inner azimuth gimbal measurements are presented in this study since larger frequency bandwidth can be measured and spectacular FRF measurements are obtained.

  During inner azimuth gimbal experiments, only the inner azimuth gimbal is excited and other three gimbals (roll, outer elevation, inner elevation) are kept under zero input. The coupling effects between inner azimuth gimbal and other gimbals are assumed to be negligible. Therefore, although the complete system is MIMO (four inputs and four outputs for each gimbal), the inner azimuth gimbal is considered to be a SISO system thanks to the fact that coupling effects are small.

  The ideal transfer function of the plant (gimbal) is considered to be $\frac{J}{s}$ (given in Eqn. 2.2) by Newton's law of motion. Here, J is the inertia of gimbal. The

input signal is the acceleration caused by a motor torque and the output signal is the rotational speed measured by gyro and hence, the frequency response of a gimbal is expected to have a magnitude slope of -20dB/dec with 90° phase.

$$G_{ideal}(s) = \frac{J}{s} \tag{2.2}$$

- ***Measurement System***: With the help of xPC Target, hardware-in-the-loop simulation is performed on a real system. xPC Target is a MATLAB product which enables you to execute Simulink models on a target computer for hardware-in-the-loop (HIL) simulation, and other real-time testing applications. The communication interface between xPC target computer and the device under investigation is RS-422 protocol with 921600 baud rate. Digital system loop frequency is 3kHz. Sampled time domain signals $u(kT_s)$ and $y(kT_s)$ are recorded at system frequency at 3kHz without any missing data. Time domain input data and gyro output data are logged in real-time with the xPC Target toolbox.

- ***Input Signal***: The input signal, $u_1(t) = u_g(t) + n_g(t)$ (a ZOH-reconstructed signal) is applied to the plant (inner azimuth gimbal system) using a motor driver card in units of volt. The designed excitation signal in xPC Target computer is sent to a motor driver card with RS-422 communication protocol in 3kHz sampling time. The input signal has a range between ±179.0 numeric value which is scaled to ±10.0 volts in the motor driver card. Motor driver card controls the inner azimuth gimbal and generates a torque with respect to the commanded input signal resulting in angular acceleration of the system.

- ***Output Signal***: The output signal, $y_1(t)$ is the rotational speed of the inner azimuth gimbal. This signal is sensed from azimuth gyro sensor in units of degree/second. Azimuth gyro sensor is located in an inertial measurement unit (IMU), namely LN-200. IMU is an electronic device which measures the three axis accelerations and three axis rotational speeds. The sampling rate of LN-200 is 400Hz. This means that the bandwidth of the azimuth gyro is 200Hz which is the half of the sampling rate. Due to this limited bandwidth, the FRF measurements realized in this study are intended to cover a bandwidth up to 250Hz. Actually, the results of this study will be used for controller design

purposes. Considering the controller bandwidth of inner azimuth gimbal which is usually less than 60Hz, the gyro sensor sampling rate is sufficiently high for this application.

- ***Noise***: $m_u(t)$, $m_y(t)$ are measurement noises respectively on input and output signals. In this study, input signal is exactly known: because, FRF measurements are realized with the digital hardware and input signals are stored in computer memory. Therefore, input measurement noise, $m_u(t)$ is set to zero ($m_u(t) = 0$). The output measurement noise, $m_y(t)$ is related to the gyro sensor noise and it is different from zero. Generator noise on input signal is illustrated with $n_g(t)$. Generator noise in this study, is related to quantization noise. Input signal is designed as a 32-bit floating number while applied input signal in units of volts is represented with 12-bit number resulting in reduced sensitivity and quantization error. The process noise, $n_p(t)$, is related to the plant under investigation subjected to undesired disturbances. These disturbances in measurement will cause random angular speed deviations.

2.4 Inner Gimbal Constraints

Usually, in every application, there are various restrictions on the input signal. Most common restrictions on the input signal are the maximal allowed amplitude and maximum user specified derivative of the input signal. In this study, for the device under investigation, there are two particular constraints:

(i). The first constraint is, “the input signal should not exceed ±179 volts command in magnitude”.

(ii). The second constraint is, “the angular position of the gimbal should not change more than ±2° degrees”. The inner azimuth gimbal has a range of ±5° degrees from the outer gimbal. If the perturbation signal for the inner azimuth gimbal is designed to cause movements more than ±2° degrees, there is a high possibility of hitting edges of the mechanical system.

The first constraint can be checked easily since user has full control over the applied input signal. Examining the second constraint, however, is a bit more complicated. In order to check the second constraint, parametric model of the system is required (see Definition 1.1.2 on page 2). In Chapters 6 and 7, estimation of the parametric model is explained in detail. Using the parametric model, it is possible to simulate the time response of a continuous or discrete linear time invariant system to designed excitation signals. The second constraint is checked by observing the integral of the gyro output signal, obtained in the simulation. Integral of the gyro output signal represents the angular position of the gimbal with some offset.

CHAPTER 3

DESIGN OF EXCITATION SIGNALS

3.1 Introduction

Excitation signal design is a fundamental and very critical step in system identification. The dynamic behavior of a mechanical system is obtained from input and output signals, strictly speaking, nonparametric measurements (see Definition 1.1.1 on page 2). Instead of exciting the system frequency by frequency and measuring system response independently, a broadband excitation spectrum can be applied to system enabling to gather all system frequency response in a single measurement (see Section 3.4). In the literature, many types of broadband perturbation signals are proposed. These perturbation signals can be categorized in three groups: transient signals; non-transient aperiodic signals; periodic signals [2].

(i). Transient signals: Examples of transient signals are random burst signal and impulse signal. A random burst signal is a noise sequence that is imposed on the system during the first part of the measurement, and a zero input is applied for the rest of the measurement period. In the second part of measurement where zero input is applied, the system response is expected to be damped out so that spectral leakage errors disappear in FRF analyses.

(ii). Non-transient aperiodic signals: Non-transient aperiodic signal example is random noise signal.

(iii). Periodic signals: Examples of periodic signals are swept sine signal, Schroeder multisine signal, random phase multisine signal and pseudorandom binary

sequence signals. Periodic signal class is the main excitation signal group used in this study.

It is important that no spectral leakage error appears during the analysis of the measurements. Non-transient aperiodic signals cause spectral leakage in FRF analysis. Therefore non-transient aperiodic signals are not favored (see Section 3.3). On the other hand, the transient signals cause no spectral leakage, but controlling the power spectrum is difficult. The frequencies outside the frequency band of interest are also excited which is an undesirable property in most cases. As a result, transient signals are not preferred either. Periodic signals as a choice, shaping the power spectrum is usually easy and straightforward. Additionally, periodic signals introduce no spectral leakage when an integer number of signal periods are measured (see Section 3.3) and it is possible to efficiently reduce noise variance in FRF measurements with averaging methods (see Section 4.3 on page 39). After all, periodic excitation signal becomes the first choice considering many advantages.

For excitation signals, signal to noise ratio (SNR) is an extremely important property. In all experiments, the desired signal to be measured is disturbed by undesired background noise. In frequency response function measurements, the time it takes to reach a specified accuracy is inversely proportional to the square of SNR [2,3]. In other words, a decrease of 6 dB for SNR, increases the time of measurement to reach the same accuracy by a factor of four. Even worse than that, in some cases, low SNR would introduce bias errors in frequency response function measurements which can not be compensated by increasing measurement time [4]. By averaging the measurements, the random errors can be reduced, but systematic bias errors will remain. Therefore, a good excitation signal should provide as high power spectrum as possible without exceeding normal operation conditions. Crest factor property explained in Section 3.2 can be used to quantify the quality of excitation signal in that sense. The low crest factor indicates that excitation signal can provide high SNR while satisfying normal operation conditions.

In the experiments realized in this chapter, three general purpose periodic excitation signals are constructed: swept sine, also called periodic chirp; Schroeder multisine excitation; pseudo random binary sequences (see Sections 3.5, 3.6, 3.7). General pur-

pose means that, no optimization is executed on excitation signal to deal with specific restrictions. General purpose excitation signals are able to excite the system with an almost flat power spectrum in a frequency range of interest. The main parameters to be selected are the frequency bandwidth of interest, overall magnitude spectrum, and the frequency resolution of the measurement. After designing the excitation signal, simulations are performed to see whether aforementioned two restrictions are satisfied (see Section 2.4 on page 12). If not satisfied, overall power spectrum is decreased iteratively, sacrificing from SNR.

It is important to satisfy restrictions on excitation signal while providing high SNR. General purpose signals are usually sufficient for this scope and can be applied directly. However, if design time is not an issue, the excitation signal that best fit the application can be searched. Power spectrum of the excitation signals can be optimized to achieve better SNR in the frequency band of interest while satisfying device specific constraints (see Section 2.4 on page 12). Optimization routine is performed in an offline study. The optimization procedure applied in this study usually takes a few minutes to reach a satisfactory local minimum solution on an average computer (Intel Core 2 Duo CPU, @2.0GHz, 32 bit operating system). Since the computer power increases day by day with technology, the efforts and time spent in optimization should be motivated. This concept is explained in detail with an example in Section 3.8.

3.2 Crest Factor

Definition 3.2.1 (Crest Factor) *The crest factor $Cr(u)$, is a measure of an excitation signal $u(t)$, showing the ratio of peak amplitude u_{peak}, to its rms value u_{rmse} in the frequency band of interest.*

$$Cr(u) = \frac{u_{peak}}{u_{rmse}} = \frac{\max\limits_{t\in[0,T]} |u(t)|}{u_{rms}\sqrt{P_{int}/P_{tot}}} \quad with \quad u_{rms}^2 = \frac{1}{T}\int_0^T u^2(t)\,\mathrm{d}t \tag{3.1}$$

with T the measurement time, u_{rms} the rms value of the signal, P_{tot} the total power of the signal, and P_{int} the power in the frequency band of interest [3].

The crest factor is a dimensionless quantity, being a positive real number. The minimum possible crest factor is 1. The crest factor of a pure sine wave is $\sqrt{2} = 1.41$. Small

crest factor is an indication of good quality for the excitation signal. It is crucial for the excitation signal to provide high SNR without exceeding maximum specified amplitude value. This limit value for the experiments in this study is ±179 volt command (see Section 2.4 on page 12).

3.3 Minimizing Spectral Leakage Error by Measuring an Integer Number of Signal Periods

Input signals are designed to excite a certain frequency band of interest while satisfying some special restrictions (see Section 2.4 on page 12). Power spectrum is carefully designed to perturb the frequency band with high SNR. However, if an unsuitable excitation signal is applied to the system, the resulting power spectrum can be completely different from what was intended at first. Misused excitation signals may result in poor SNR during the measurement process.

One common example for wrong application is, applying non-integer number of signal periods in a measurement. For instance, consider a periodic excitation signal with period $T_0 = 2$ seconds. Then, the total measurement time T, should be an integer number of signal periods $T = MT_0$, $M \in \mathbb{N}$. Otherwise, fractional signal period will be measured instead of full one. This situation causes spectral leakage error in frequency response function measurement (FRF). From signal period, the frequency resolution f_0 can be derived as $f_0 = 1/T_0 = 0.5$ Hz. So, the measured (sampled) frequencies in the discrete Fourier transform (DFT) should correspond to multiples of frequency resolution, $f = [0.5,\ 1,\ 1.5,\ \ldots,\ rf_0,\ \ldots]$ Hz, $r \in \mathbb{N}$. Measuring an integer number of signal periods ensures this correspondence.

The discrete Fourier transform (DFT) is explained in Definition 3.3.1.

Definition 3.3.1 (DFT) *Consider a finite length sequence $u(nT_s)$ of length N samples such that $u(nT_s) = 0$ outside the range $0 \leq n \leq N-1$. The DFT relations between the*

frequency and time domain sequences are given in the following formulae (3.2) [3, 5].

$$\begin{aligned} \textit{Analysis equation: } U(k) &= \sum_{n=0}^{N-1} u(nT_s)e^{-j2\pi kn/N} \\ \textit{Synthesis equation: } u(nT_s) &= \frac{1}{N}\sum_{k=0}^{N-1} U(k)e^{j2\pi kn/N} \end{aligned} \tag{3.2}$$

To each finite-length sequence of length N, the finite sequence can always be associated with a periodic sequence (see Eqn. 3.3) [5].

$$\tilde{u}(nT_s) = \sum_{r=-\infty}^{\infty} u((n+rN)T_s) \tag{3.3}$$

$\tilde{u}(nT_s)$ is a periodic sequence[1] with period N, so that $\tilde{u}(nT_s) = u((n+rN)T_s)$ for any integer value of n and r. Discrete Fourier transform assumes periodicity of the signal in the time domain. In other words, the DFT assumes that the finite data set $u(nT_s)$ for $n = 0, 1, \ldots, N-1$, is one period of a periodic signal $\tilde{u}(nT_s)$. So the two endpoints, $u(0)$ and $u(NT_s)$ are interpreted as though they were connected together. When this assumption is violated, in FRF analysis, spectral leakage occurs (Example: Non-transient aperiodic signals such as random noise excitation signal). In [6], windowing techniques are analyzed to reduce leakage errors when random excitations are used, but systematic errors will not completely disappear. Therefore, whenever possible, it is advised to use periodic excitation signals and measure an integer number of signal periods.

To illustrate spectral leakage example, a periodic signal with period $T_0 = 2$ seconds, frequency resolution $f_0 = 1/T_0 = 0.5$ Hz is designed. Designed excitation signal contains sine waves with equal amplitudes from 2 Hz to 250 Hz ($f = [2,\ 2.5,\ 3,\ \ldots 250]$Hz). Sampling frequency of the discrete system is $f_s = 3000$ Hz, so no aliasing effect occurs. In Fig. 3.1, the amplitude spectrum of two input measurements are displayed. On the left, an integer number of signal period is measured $T = 1 \cdot T_0 = 2$ seconds, so no leakage errors exist. On the right, non-integer number of signal period is measured $T = 1.2 \cdot T_0 = 2.4$ seconds, resulting in spectral leakage in magnitude spectrum.

[1] tilde (˜) emphasizes here that sequence is periodic

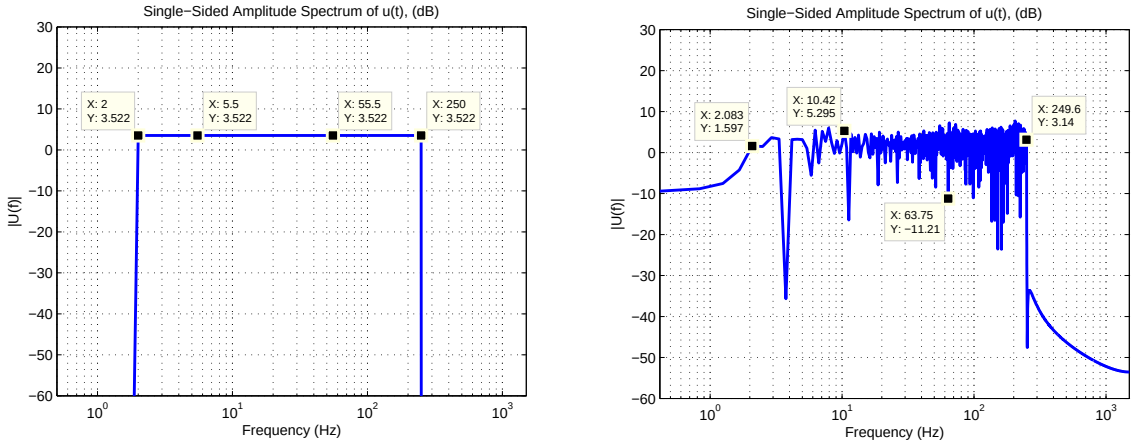

Figure 3.1: *Left Figure*: An integer number of periods measured. No leakage error. $T = T_0 = 2$ seconds. *Right Figure*: The presence of spectral leakage due to non-integer number of signal period measurement. $T = 1.2 \cdot T_0 = 2.4$ seconds.

3.4 The Comparison Between Stepped Sine and Broadband Excitation Signals

The purpose of experiments realized in this study is, measuring the frequency response function in a fixed time while maximizing accuracy. In the meantime, the restrictions mentioned in Section 2.4 on page 12 should be satisfied (maximal allowed amplitude on input signal and maximal allowed angular position of gimbal). While designing an excitation signal, two alternatives can be considered. The system can be excited with either stepped sine signal or broadband signal:

(i). In the stepped sine excitation, the system is excited frequency by frequency. The number of frequencies at which system response observed, equals to the number of independent measurements, M. See Fig. 3.2 for an overview of stepped sine excitation signal measurement setup. Between each measurement step, sufficient time, T_w, is waited in order to reduce transient effects due to frequency shift. In every measurement step, P signal periods are measured so that with enough averages, the output noise can be decreased (see Section 4.3 on page 39 for averaging method).

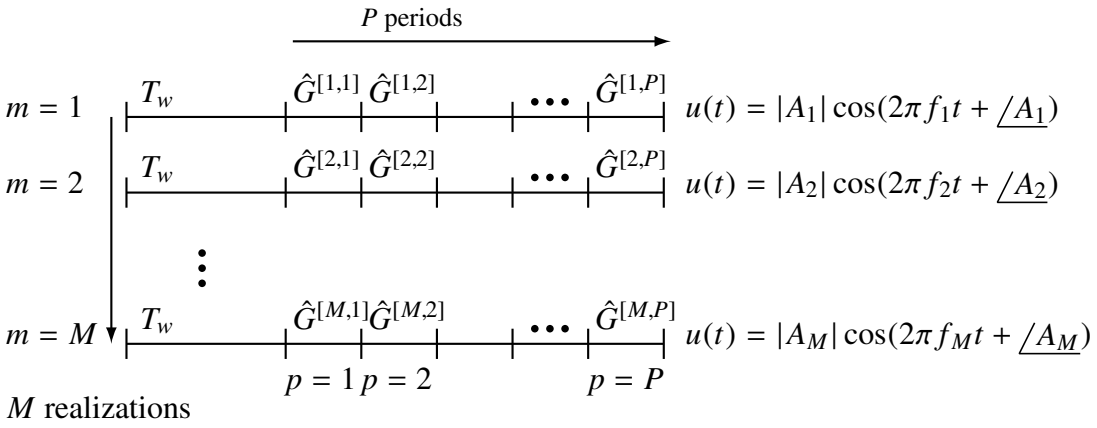

Figure 3.2: *Stepped Sine measurement overview*: Realizing M different (independent) single sine experiments in a consecutive manner and each time measuring P periods after a waiting time T_w to reduce transient effects.

(ii). In broadband excitation, the system is excited with all frequency harmonics of interest, simultaneously. It is possible to gather all system frequency response in a single measurement. As discussed in Section 3.1, many types of broadband perturbation signal are possible. In Fig. 3.3, an overview of measurement setup with broadband multisine signal example is given. Before starting the measurement, a suitable time, T_w, is waited for the output to reach steady state. P signal periods are measured so that with enough averages, the output noise can be decreased (see Section 4.3 on page 39 for averaging method).

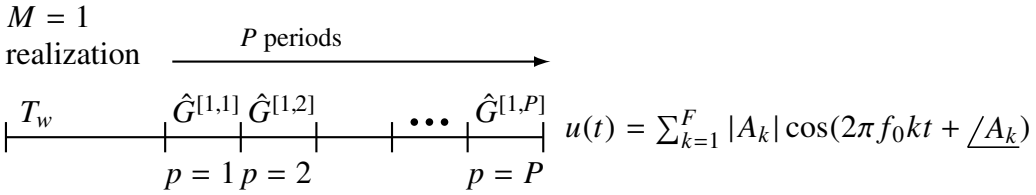

Figure 3.3: *Broadband measurement overview*: Measuring P periods after a waiting time T_w to reduce transient effects. One realization is adequate for measuring the response of all excited frequency band.

For the stepped sine excitation signal, at each measurement step, all the power is focused on a single frequency so that SNR is maximized without much effort. Max-

imizing SNR means minimizing systematic bias errors which is very crucial. With enough averages, the variance can be reduced as well and an excellent accuracy can be obtained. However, due to frequency shifts at each step, a total of MT_w seconds should be waited. Especially for lightly damped mechanical systems, T_w needs to be bigger due to long transients resulting in an excessive measurement time. On the other hand, for broadband excitation signals, the time T_w is waited only once, at the start of measurements. The critical issue about broadband excitation signals is that, maximizing SNR is not as straightforward as for the stepped sine. In this chapter, general purpose excitation signals are shown which usually provide sufficient SNR. It is also demonstrated how to further optimize broadband signals and reach high SNR in the frequency band of interest.

In [7], the conditions under which broadband measurements are faster than stepped sine measurements are analyzed deeply. From this analysis, it is stated that, for a measurement with high SNR (Example: SNR > 40dB), a well designed broadband excitation signal requires significantly less time to reach a specified accuracy compared to a stepped sine. For a measurement with low SNR (Example: SNR<20dB), the required time to reach a specified accuracy is approximately the same for both, but broadband excitation signals are still slightly better.

To sum up, the most important deciding factor is the available SNR in the frequency band of interest. Whenever a broadband signal which provides as high SNR as stepped sine provides, can be designed, broadband excitation signal should be preferred. Because for the same SNR, broadband is always superior to stepped sine in terms of measurement time to reach a specified accuracy. However, it is not always possible to design a sufficiently high SNR with a broadband excitation signal. For instance, for the device under investigation in this study (inner azimuth gimbal of electro optic system), for the low frequency band of [0.5, 4]Hz, the broadband signal could not provide enough SNR resulting in systematic bias errors (more details are in Chapters 4 and 5). The reason broadband signals fail in this low frequency band is the restriction specific to device under investigation: “The maximal allowed angular position is ±2° degrees”. On the other hand, for the high frequency band of [4.5, 500]Hz, broadband signals could provide pretty high SNR resulting in an excellent accuracy in a pretty small time compared to stepped sine signals. As a result, concerning the device under

investigation, stepped sine excitation signal is optimal for the low frequency band [0.5, 4]Hz and broadband excitation signal is optimal for the high frequency band [4.5, 500]Hz. As a suggestion, frequency response functions (FRFs) of the low and high frequency bands can be measured independently and the two results can be combined later.

3.5 Schroeder Multisine

Definition 3.5.1 (Schroeder Multisine) *A Schroeder multisine is a sum of harmonically related sine waves*

$$u(t) = \sum_{k=1}^{F} A\cos(2\pi f_k t + \phi_k) \tag{3.4}$$

with Schroeder phases $\phi_k = -k(k-1)\pi/F$ *and* $f_k = l_k f_0$ *with* $l_k \in \mathbb{N}$ [3].

For the device under investigation, a Schroeder multisine excitation signal is designed such that the two constraints aforementioned in Section 2.4 on page 12 are satisfied. This signal will be used later in multisine experiment in Subsection 4.4.2 on page 45. Designed perturbation signal has following properties.

- Signal period is $T_0 = 2$ seconds. Frequency resolution f_0 is 0.5 Hz from $f_0 = 1/T_0$.
- Sampling frequency of the system, f_s is 3 kHz and sampling period is 1/3000 seconds from $T_s = 1/f_s$.
- Number of waves is $F = 500$. Discrete grid is $l_k = 1 : F = [1, 2, 3 \ldots 500]$ Therefore, from $f_k = l_k f_0$ excited frequency band is between 0.5Hz and 250Hz.
- Magnitude of the signal, A is chosen to be $A = 1500/F = 3$ volt command. A is tuned in order to keep line of sight angular position of the system between $\pm 2^\circ$ degrees which is the nominal operating condition.
- Offset phase ϕ_k is 0.2793 rad. This phase is tuned in order to keep the line of sight angle of system around zero position.
- The crest factor for the frequency band of interest [0.5, 250]Hz, is calculated to be $Cr(u) = 1.73$ (see Section 3.2).

The designed multisine excitation signal power spectrum can be examined from Fig. 3.4 and in the time domain from Fig. 3.5. For the designed multisine signal in this section, the ratio of the power in the frequency range of interest to the total power is $\frac{P_{int}}{P_{tot}} = 1$. This feature shows the superiority of the multisine signal. In general, for multisine signals, shaping the magnitude spectrum of excitation signal is very easy since for each frequency component, the amplitude depends on an individual sine wave. On the other hand, choosing the phases of each sine wave is not trivial. Note that, a multisine signal with Schroeder phases provide low crest factor (≈ 1.7) only when flat amplitude spectrum excitation is desired. However, when magnitude spectrum is not constant over the excited frequency bandwidth, Schroeder phases result in poor excitation signal with high crest factor. In that case, an optimum phase spectrum can be searched as explained in Section 3.8.

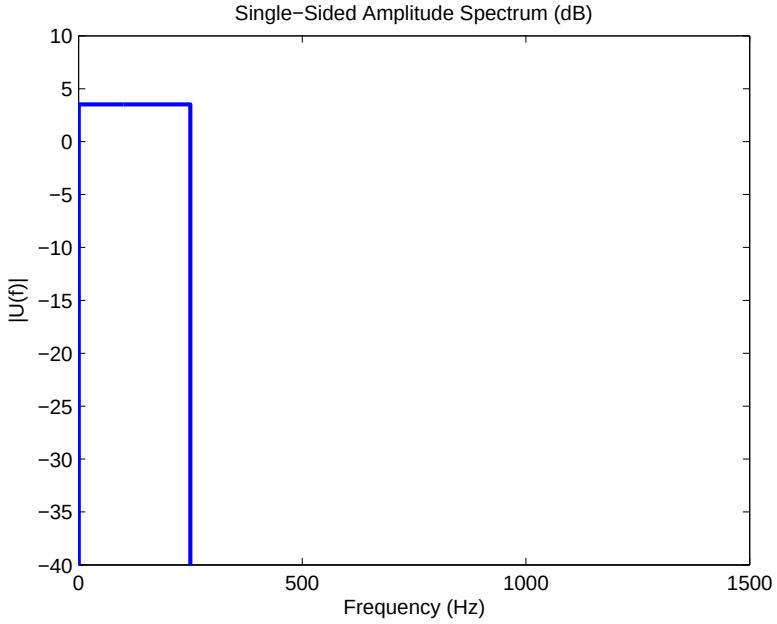

Figure 3.4: Schroeder Multisine experiment signal spectrum

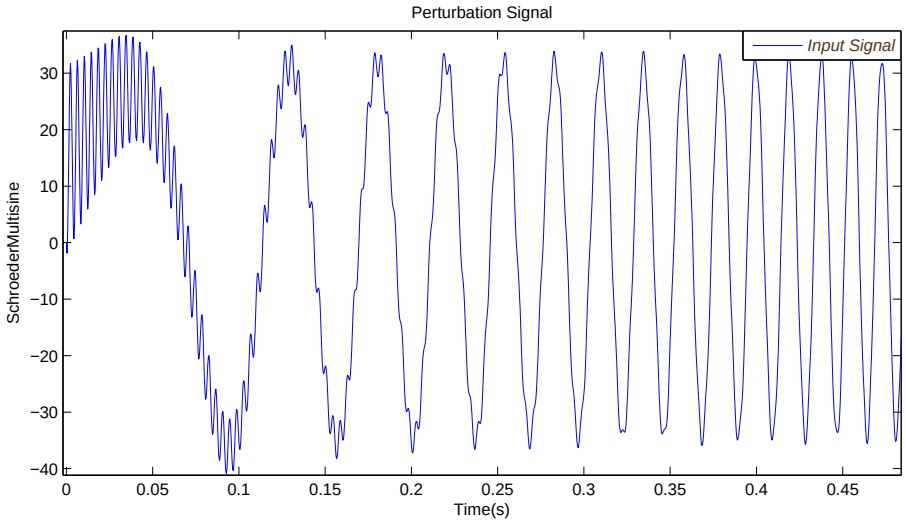

Figure 3.5: Schroeder Multisine experiment signal in the time domain

3.6 Pseudorandom Binary Sequence

Definition 3.6.1 (Pseudorandom Binary Sequence) *A pseudorandom binary sequence (PRBS) is a deterministic, periodic sequence of length N that switches between one level (e.g., +A) and another level (e.g., -A). The switches can occur only on a discrete-time grid at multiples of the clock period* T_c *(*$k_l T_c, kl \in \mathbb{N}$*)* [3].

For the device under investigation, a PRBS excitation signal is generated such that the two constraints aforementioned in Section 2.4 on page 12 are satisfied. This signal will be used later in pseudo random binary sequence experiment in Subsection 4.4.3 on page 48. Designed perturbation signal has following properties.

- Sampling frequency of the system, f_s is 3 kHz and sampling period is 1/3000 seconds from $T_s = 1/f_s$.
- Most of the power is below $0.4 f_c = 0.4/T_c$ (see Fig. 3.7) [3]. Therefore optimal choice of the clock frequency $f_c = 2.5 f_{max}$ with f_{max} the maximum frequency of interest. In the experiment, maximum frequency of interest is selected as $f_{max} = 300$ Hz. Therefore clock frequency is $f_c = 750$ Hz and $T_c \cong 0.0013$ seconds.

- Binary magnitude of the signal, A is chosen to be 45 volt command. A is tuned in order to keep line of sight angle of the system between $\pm 2^{\circ}$ degrees which is the nominal operating condition.
- In the generation of PRBS signal, a pseudo code suggested in [3] is used. This method generates a PRBS with length N = 4k-1 where N is selected as a prime number (e.g., N = 3, 7, 11, 19, 23, 31, ...). In this PSRB signal, N is chosen to be 1553. For the signal generation setup, see Fig. 3.6. The code is generated by the following MATLAB code:

```
x = -ones(N,1) * A;    x(mod([1 : N].^2, N) + 1) = A;    x(1) = A;
```

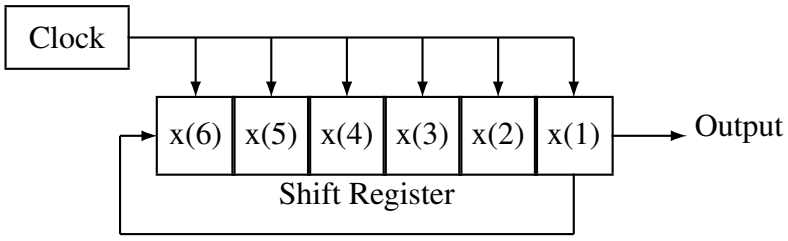

Figure 3.6: Generation of a PRBS signal with a shift register

- Signal period is 2.07 seconds from $T_0 = NT_c$. Frequency resolution f_0 is 0.48 Hz from $f_0 = 1/T_0$.
- The crest factor for the frequency band of interest [0.48, 300]Hz, is calculated to be $Cr(u) = 1.21$ (see Section 3.2).

The designed PRBS excitation signal power spectrum can be examined from Fig. 3.7 and in the time domain from Fig. 3.8. For the designed PRBS signal in this section, the ratio of the power in the frequency range of interest to the total power is found to be $\frac{P_{int}}{P_{tot}} = 0.68$ which is remarkably smaller than 1. Although a considerable part of the total energy lies outside the frequency band of interest, the crest factor is still pretty small. That is because, PRBS excitation signal can inject a lot of power with minimum peak to peak. This feature shows the excellence of the PRBS signal. The disadvantage of this signal would be, designing an arbitrary magnitude spectrum other than a flat magnitude spectrum (constant in a frequency band of interest) is challenging.

In other words, shaping the magnitude spectrum of excitation signal is difficult. Also, the derivative of this PRBS excitation signal is infinity which may cause unexpected troubles in some systems.

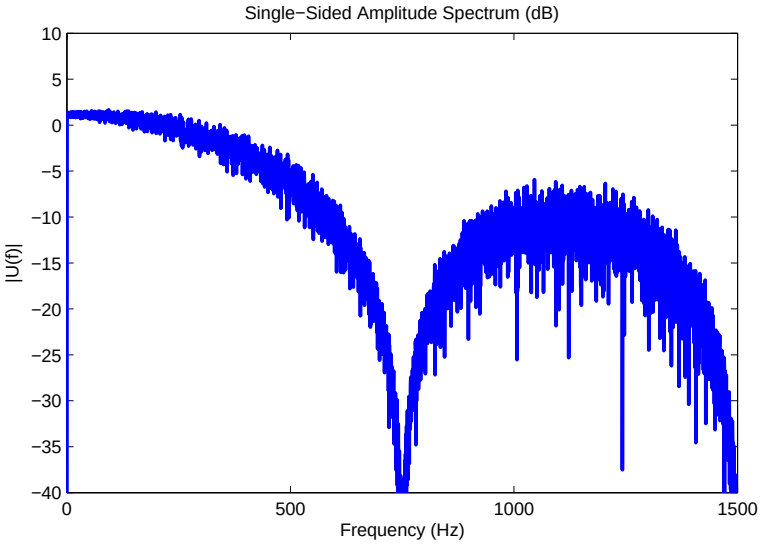

Figure 3.7: PRBS experiment signal spectrum

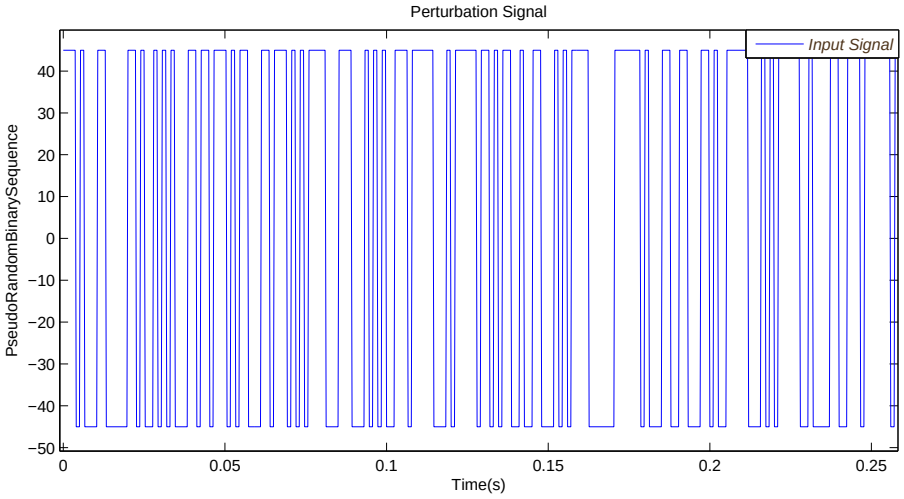

Figure 3.8: PRBS experiment signal in the time domain

3.7 Swept Sine

Definition 3.7.1 (Swept Sine) *A swept sine (also called periodic chirp) is a sine sweep test, where the frequency is swept up or down in one measurement period, and this is repeated in such a way that a periodic signal is created* [3]. Swept sine excitation signal is given in Eqn. (3.5).

$$u(t) = A\sin(2\pi f_i(t)t + \phi), \quad 0 \leq t \leq T_0 \tag{3.5}$$

T_0 is signal period. ϕ is initial phase. Frequency can be swept linearly or logarithmically with respect to time. For linear chirp, $f_i(t)$ is given in equation (3.6).

$$f_i(t) = f_{start} + \beta t, \quad \beta = (f_{end} - f_{start})/T_0 \tag{3.6}$$

For logarithmic chirp, $f_i(t)$ is given in Eqn. (3.7).

$$f_i(t) = f_{start}\beta^t, \quad \beta = (f_{end}/f_{start})^{1/T_0} \tag{3.7}$$

f_{start} and f_{end} are lowest and highest frequencies of interest respectively.

For the device under investigation, a logarithmic swept sine excitation signal is generated such that the two constraints aforementioned in Section 2.4 on page 12 are satisfied. This signal will be used later in swept sine experiment in Subsection 4.4.4 on page 52. Designed perturbation signal has following properties.

- Sampling frequency of the system, f_s is 3 kHz and sampling period is 1/3000 seconds from $T_s = 1/f_s$.
- Chirp method is logarithmic.
- Signal period T_0 is 2 seconds. Frequency resolution f_0 is 0.5 Hz from $f_0 = 1/T_0$.
- Magnitude of the signal, A is chosen to be 16 volt command. A is tuned in order to keep line of sight angle of the system between $\pm 2^\circ$ degrees which is the nominal operating condition.
- Initial phase is $\phi = 45$ degrees.
- Instantaneous frequency at time 0 is $f_{start} = 0.5$ Hz and instantaneous frequency at time T_0 is $f_{end} = 250$ Hz.

- The crest factor for the frequency band of interest [0.5, 250]Hz, is calculated to be $Cr(u) = 1.51$ (see Section 3.2).

The designed swept sine excitation signal power spectrum can be examined from Fig. 3.9 and in the time domain from Fig. 3.10. For the designed swept sine signal in this section, the ratio of the power in the frequency range of interest to the total power is found to be $\frac{P_{int}}{P_{tot}} = 0.99$ which is a favored result. Usually, it is desired to inject more power in frequencies where noise is high so that roughly constant SNR in the frequency band of interest is obtained [4]. However, for the swept sine excitation signal, shaping the magnitude spectrum arbitrarily is not as straightforward as for the multisine excitation signal. The awkwardness in designing the magnitude spectrum can be considired as a drawback of the swept sine excitation signal.

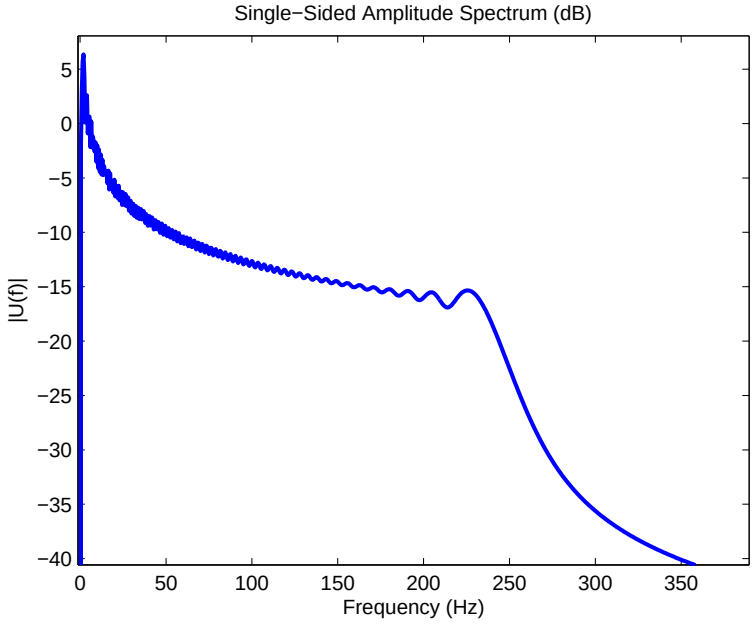

Figure 3.9: Swept Sine experiment signal spectrum

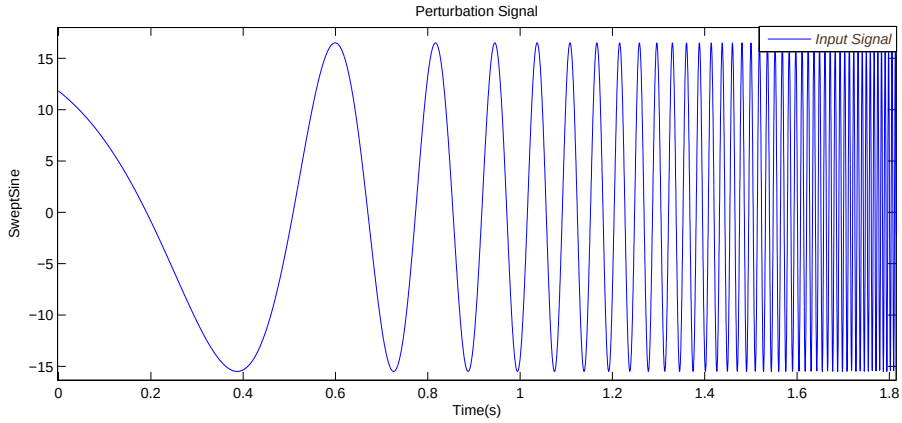

Figure 3.10: Swept Sine experiment signal in the time domain

3.8 Optimized Multisine Design

3.8.1 Discussion

General purpose signals are usually sufficient for the experiments in this study and can be applied directly. Still, when design time is not limited, an excitation signal that best fits the application can be searched. In order to design an optimization algorithm, it is obligatory to specify the final aim. A good excitation signal should provide high SNR while satisfying some constraints. Power spectrum of the excitation signals can be optimized in an offline study to achieve better SNR in the frequency band of interest while satisfying necessary constraints. The requirements imposed on excitation signals vary from system to system.

In literature, some techniques are proposed for excitation signal optimization. These techniques attempt to maximize SNR while limiting the maximum value of excitation signal in the time domain. In reference [8], an efficient method for peak factor minimization using a time-frequency domain swapping algorithm is presented. In reference [9], a method for crest factor minimization using nonlinear Chebyshev approximation is given. It is also shown in [9] that, peak value of an excitation signal can be further reduced by allowing some extra energy at additional frequencies in which designer is not interested. According to [10], the algorithm presented in [9] is

more successful but slower method than the algorithm presented in [8]. The specific restriction imposed on these two algorithms is the maximal allowed amplitude for the input signal in order to maintain plant friendly signals. For the device under investigation in this study, similar restriction exists: "The input signal should not exceed ±179 volt command in magnitude". However, there exists an additional restriction: "The angular position of the gimbal should not change more than ±2° degrees" (see Section 2.4 on page 12 for the reason of extra restriction). Therefore, a different cost function is required for applications in this study.

3.8.2 Problem Formulation

Problem: Consider the multisine excitation signal given in (3.8):

$$u(t) = \sum_{k=1}^{F} |A_k| \cdot \cos(2\pi f_0 k t + \angle A_k) \tag{3.8}$$

Here, $f_0 = \dfrac{1}{T_0}$ is the frequency resolution with T_0 being the signal period. There are F frequency components in $u(t)$ and no DC component. $|A_k|$ defines the magnitude spectrum of excitation signal and it is fixed in pre-design in such a way that sufficiently high SNR for the experiment is satisfied (see Fig. 3.11). The magnitude spectrum of the excitation signal, $|A_k|$ will not change during the optimization process.

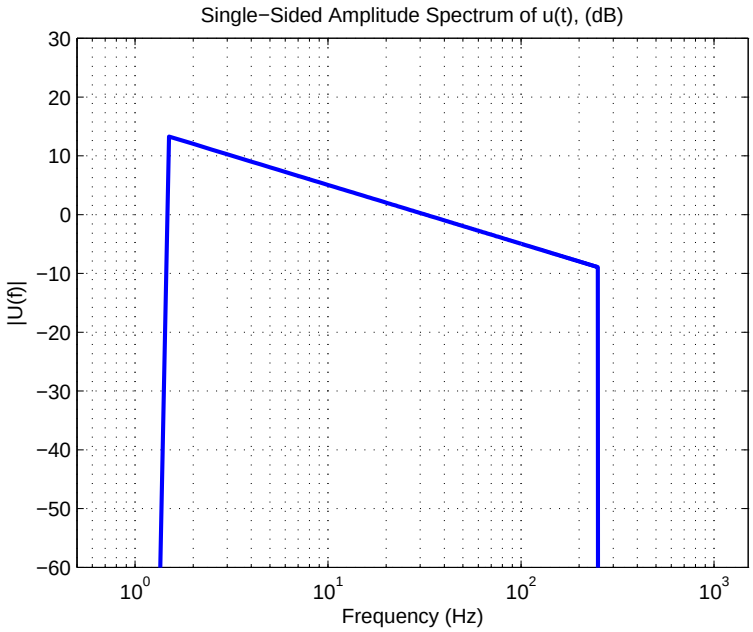

Figure 3.11: Fixed magnitude spectrum of multisine excitation signal

Phases $\phi_k = \underline{/A_k}$ are free design variables and define the phase spectrum of excitation signals. During the optimization process, multisine phases are optimized.

Minimize: There exist two cost values to be minimized, $f_1(\phi_k)$ and $f_2(\phi_k)$:

$$f(\phi_k) = \begin{bmatrix} f_1(\phi_k) \\ f_2(\phi_k) \end{bmatrix} \tag{3.9}$$

The nonlinear least squares algorithm is appropriate for this optimization problem:

$$\min_{\phi_k} \|f(\phi_k)\|_2^2 = \min_{\phi_k} (f_1(\phi_k)^2 + f_2(\phi_k)^2) \tag{3.10}$$

Here, ϕ_k is a $Fx1$ sized vector and $f(\phi_k)$ is a function that returns a $2x1$ sized vector value.

In order to handle the first restriction (see Section 2.4 on page 12), the first cost function is chosen as $f_1(\phi_k) = \tau_1 \cdot Cr(u)$. Here, $Cr(u)$ represents the crest factor (see Section 3.2) and τ_1 is a tuning parameter to weight the cost with respect to $f_2(\phi_k)$.

In order to handle second the constraint (see Section 2.4 on page 12), the parametric model of the system is required (see Definition 1.1.2 on page 2). In Chapters 6 and 7, estimation of the parametric model is explained in detail. Using the parametric model, it is possible to simulate the time response of continuous or discrete, linear, time invariant system to designed excitation signals. The second constraint is checked by observing the integral of the gyro output signal, obtained in the simulation. Integral of the gyro output signal represents the angular position of the gimbal with some offset. Therefore, the second cost function is chosen as $f_2(\phi_k) = \tau_2 \cdot (\Theta_{peak2peak}/2)$. Here, $\Theta_{peak2peak}$ is maximum to minimum difference of expected angular gimbal position during simulations. τ_2 is a tuning parameter to weight the cost with respect to $f_1(\phi_k)$. Simulation setup is given in Fig. 3.12.

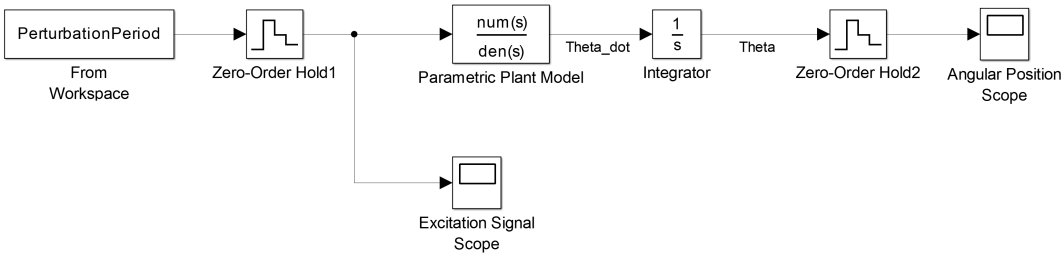

Figure 3.12: Simulation setup: Excitation signal and parametric plant model response

Such that: Optionally, but not necessarily, phases can be restricted to stay in $[0,\ 2\pi)$ for faster convergence: $0 \leq \phi_k < 2\pi, \quad \text{for } k = 0, 1, \ldots, F.$

Starting point: The optimization starts at the point ϕ_0 ($Fx1$ sized phase vector) and finds a minimum of the sum of squares of the functions described in $f(\phi_k)$. In this study, starting point is chosen as $\phi_0 = \underline{/A_0}$ independent, uniformly distributed random phases on $[0,\ 2\pi)$.

3.8.3 Results

The iterative method presented here is based on the cost function (3.10). It is observed that for each random starting point, optimization converges a different local minimum. This indicates that "Nonlinear Least Squares" estimator suffers from the problem of having multiple solutions and local minimums. This is mainly due to the very complex phase dependency of the cost function resulting in many local minimums. Global optimization algorithms can be used to overcome the problem of multiple local minimums. However, these algorithms are usually very time-consuming.

In Fig. 3.13, the evolution of cost function versus iterations is presented. The amount of time necessary to reach a satisfactory local minimum solution depends strongly on the number of excited frequency lines, F. The lower the number of phases to be optimized, the faster the solution converges. For the optimization procedure applied in this study, there are $F = 500$ frequency lines and it takes a few minutes to converge to a local minimum on an average computer (Intel Core 2 Duo CPU, @2.0GHz, 32 bit operating system). Since the computer power increases day by day with technology, time spent in optimization should not be regarded as a drawback.

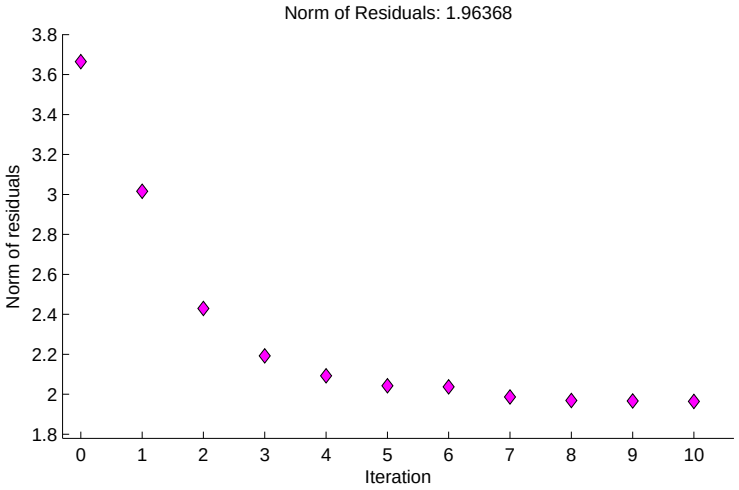

Figure 3.13: The evolution of cost function versus iterations

The initial point in optimization is chosen as a random phase multisine signal (see Subsection 3.8.2). After the optimization procedure, the crest factor is reduced from $Cr(u) = 4.19$ to $Cr(u) = 2.68$ and the peak value of the input signal is reduced from 109.1 to 69.9 (see Fig. 3.14). Meanwhile, in the simulation, the expected peak value of the angular position of the gimbal is reduced from $\pm 1.94^\circ$ to $\pm 1.40^\circ$ degrees which is well below the $\pm 2.0^\circ$ degrees constraint (see Fig. 3.15).

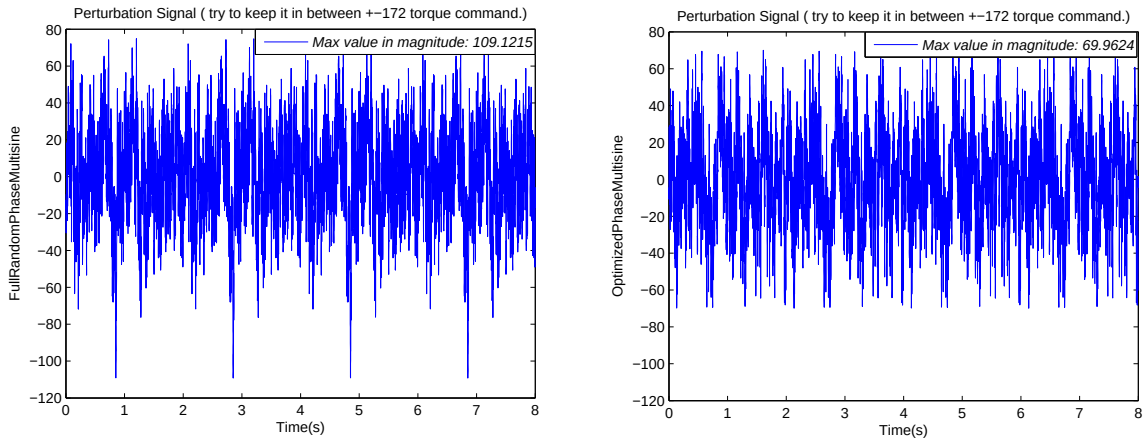

Figure 3.14: *Left Figure*: Initial random phase multisine signal in the time domain. *Right Figure*: Optimized phase multisine signal in the time domain.

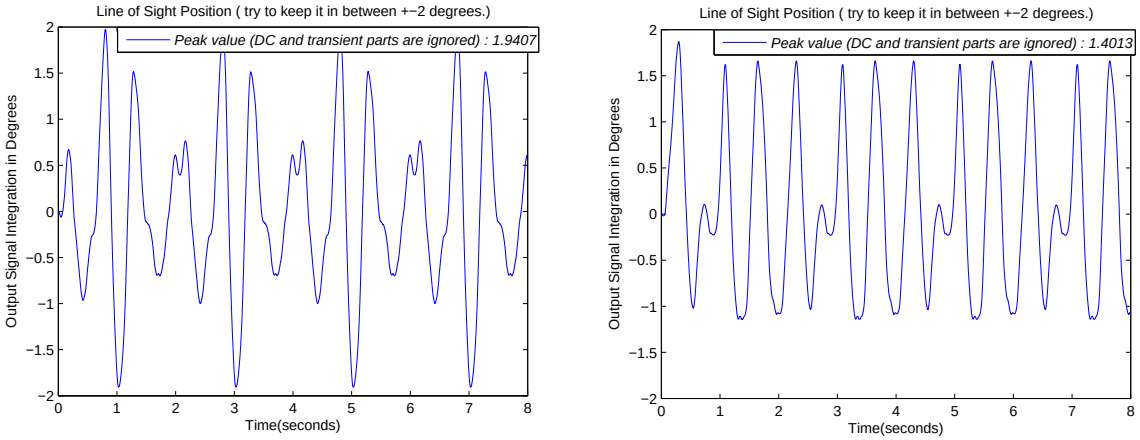

Figure 3.15: *Left Figure*: The expected angular position response to initial random phase multisine signal. *Right Figure*: The expected angular position response to optimized phase multisine signal.

CHAPTER 4

FREQUENCY RESPONSE FUNCTION MEASUREMENT

4.1 Introduction

Frequency response function (FRF) measurement is a fundamental step in process control applications. In order to design a controller and analyze the stability of the system, FRF measurement is the very first data an engineer requires. The explanation of FRF is given in Definition 4.1.1.

Definition 4.1.1 (Frequency Response Function) *Frequency response is a quantitative measure of magnitude and phase of the output spectrum of a system in response to an input signal. Frequency response is a function of frequency and is used to characterize the dynamics of the system.*

The procedure of FRF measurement for a physical system involves exciting the system with an input signal and recording the both input and output signals in the time domain. Then, the data in the time domain can be converted to frequency domain with fast Fourier transform (FFT) and this allows the frequency response function to be estimated with several methods. The excitation signal design topic is discussed in Chapter 3. The constructed input signal mostly excites a specific frequency band of interest. Therefore, in FRF measurement, the frequencies in which input magnitude spectrum is below a predetermined threshold level should be automatically rejected. This rejection procedure ensures the adequate signal to noise ratio (SNR) in the measured frequency band. In [11], calculation of uncertainty bounds on FRF measurements for input SNR is shown.

All measurements are subject to varying degrees of measurement error and measurement uncertainty. Estimation of measurement uncertainty is a priceless tool for robustness analyses. This chapter not only explains FRF measurements but also demonstrates the estimation of nonparametric variance (noise) spectrum.

In this chapter, the device under investigation is a four axis gyro stabilized Infrared (IR) Electro-Optic gimbal system. This device is used to inertially stabilize the IR camera on moving dynamic platforms such as fighter aircrafts. The FRF measurements are realized on the inner azimuth gimbal of the system using the periodic excitation signals designed in Chapter 3.

This chapter starts with the theory of FRF estimation in Section 4.2. It is possible to improve FRF measurements with well designed averaging techniques when periodic excitation signals are used. Averaging methods both in time domain and frequency domain are given in Section 4.3. The averaging method in the frequency domain produces additional information about the system: the nonparametric noise model. This noise model provides the robust controller designer a good insight about the reliability of FRF measurements and set the uncertainty bounds on a linear model and improves the existing controller. Before realizing FRF measurements, system behavior is observed under zero input in Subsection 4.4.1. The rest of the chapter explains the FRF measurement experiments and discusses the results. The FRF measurements realized use the periodic excitation signals designed in Chapter 3. The comparison and discussion of three experiments are given in Subsection 4.4.5.

4.2 FRF Estimation

The time domain signals are transformed to the frequency domain using the discrete Fourier transform (DFT), implemented as an FFT (fast Fourier transform). In the experiments presented in this chapter, an integer number of periods is measured so that no spectral leakage errors appear (see Section 3.3 on page 18). The FRF measurement at frequency f_k is given by (4.1):

$$\hat{G}(j\omega_k) = Y(k)/U(k) \tag{4.1}$$

Here, if L denotes the length of the measured record, then the measurement duration is $T = LT_s$ (T_s being sampling period). Here, the frequency components are $f_k = k/T$ for $k = 1, 2, \ldots, L$. This process is disturbed at different points with noise as shown in Fig. 2.2 on page 10. After the DFT we find, at frequency f_k

$$U(k) = U_0(k) + N_u(k) \tag{4.2}$$

$$Y(k) = Y_0(k) + N_y(k) \tag{4.3}$$

where $N_u(k)$ and $N_y(k)$ are the contributions of the noise to the measured Fourier coefficients. In this study, the input signal is exactly known, because it is stored in the memory of a computer. Therefore we deal with exactly known inputs. So measurement noise $m_u(t)$ is set to zero and $N_u(k) = 0$.

4.3 Averaging Methods for Periodic Excitations and Estimation of Nonparametric Noise Model

When the excitation signal is periodic and the noise is random, it is possible to enhance the SNR by averaging the periodic measurements. In general, averaging a signal reduces the noise proportional to the square root of the number of averaged samples. Averaging can be realized in either time domain or frequency domain. Averaging method in the frequency domain provides extra information which is extremely valuable. This additional benefit is the estimation of noise (co)variances, or in other words, the nonparametric noise model of the measurement.

All FRF averaging techniques start from M input-output data blocks $u^{[l]}(t), y^{[l]}(t), l = 1,2,\ldots, M$. The M input-output time domain data blocks can be collected in two different ways. Data collection can be realized either from M independent experiments which would take a long time (not feasible), or from a single experiment with M consecutive periods under certain assumptions (more practical). Under Assumptions 1 and 2, it is possible to collect M successive periods (with length N_p) and to average the measurements in the time or frequency domain over these repeated periods [3].

Assumption 1 (Disturbing Noise) *The disturbing noise $N_u(k), N_y(k)$ is independent of the true signals $U_0(k), Y_0(k)$.*

Assumption 2 (Measurement Data Blocks) *The correlation length of the noise should be much smaller than the total measurement time.*

Excitation signal is periodic with period T_0, and $u_0(nT_s) = u_0((n + N_p)T_s)$. This assumption indicates that signal period is a multiple of the sampling period $T_0 = N_pT_s$, preventing undesired leakage errors. Well implemented averaging techniques reduce the variance (and reduces the bias if input signal is noisy [3,4]) of FRF measurements. In practice, the number of averages, M is determined by the maximum measurement time T and the minimum frequency resolution f_0: $M = T/T_0 = Tf_0$. For more smooth and improved FRF measurements, averaging is strongly recommended. The more the signal is averaged, the better the SNR becomes. The trade off is, averaging more also requires longer measurement time for a fixed frequency resolution, $T = M/f_0$.

4.3.1 Averaging in the time domain

Consider M input-output data blocks $u^{[l]}(t)$, $y^{[l]}(t)$, $l = 1,2,\ldots,M$. In practice, these data blocks are gathered from a single experiment under periodic excitation with M consecutive periods satisfying Assumptions 1 and 2. Input signal period length is N_p, signal period duration is $T_0 = N_pT_s$. Then, the time domain average can be realized as in (4.4), (4.5):

$$\hat{u}(n) = \frac{1}{M}\sum_{l=0}^{M-1} u(n+lN_p) = \frac{1}{M}\sum_{l=1}^{M} u^{[l]}(n) \quad \text{with} \quad u^{[l]}(n) = u(n+(l-1)N_p) \tag{4.4}$$

$$\hat{y}(n) = \frac{1}{M}\sum_{l=0}^{M-1} y(n+lN_p) = \frac{1}{M}\sum_{l=1}^{M} y^{[l]}(n) \quad \text{with} \quad y^{[l]}(n) = y(n+(l-1)N_p) \tag{4.5}$$

The DFT's of $\hat{y}(n)$ and $\hat{u}(n)$ are, respectively denoted by: $\hat{Y}(k) = DFT(\hat{y}(n))$ and $\hat{U}(k) = DFT(\hat{u}(n))$. The FRF estimate is

$$\hat{G}_{ML}(j\omega_k) = \frac{\hat{Y}(k)}{\hat{U}(k)} \tag{4.6}$$

$\hat{G}_{ML}$ is the maximum likelihood solution for Gaussian disturbances if the repeated measurements $u^{[l]}, y^{[l]}$ can be considered to be independent over l [3]. It is known from the "Law of large numbers" and "Law of iterated logarithm" that, the noise is reduced as $1/\sqrt{M}$; and hence, asymptotically:

$$a.s. \lim_{M\to\infty} \hat{G}_{ML}(j\omega_k) = \frac{a.s. \lim_{M\to\infty} \hat{Y}(k)}{a.s. \lim_{M\to\infty} \hat{U}(k)} = \frac{Y_0(k)}{U_0(k)} = G_0(j\omega_k) \tag{4.7}$$

$$\hat{G}_{ML}(j\omega_k) = G_0(j\omega_k) + O_p(M^{-1/2}) \tag{4.8}$$

4.3.2 Averaging in the frequency domain and the estimation of noise (co)variance

Averaging in the frequency domain is computationally more costly; however, this cost is insignificant with today's PC technology. Furthermore, studying in the frequency domain provides very valuable information about the system, the estimation of noise (co)variances.

The DFTs of each subrecord is calculated seperately in (4.9):

$$U^{[l]}(k) = DFT(u^{[l]}(n)), \quad Y^{[l]}(k) = DFT(y^{[l]}(n)) \tag{4.9}$$

Then, calculation of the sample mean is given in (4.10):

$$\hat{U}(k) = \frac{1}{M}\sum_{l=1}^{M} U^{[l]}(k), \quad \hat{Y}(k) = \frac{1}{M}\sum_{l=1}^{M} Y^{[l]}(k), \quad with \quad \hat{G}_{ML}(j\omega_k) = \frac{\hat{Y}(k)}{\hat{U}(k)} \tag{4.10}$$

The calculations of the sample (co)variances are given in (4.11):

$$\hat{\sigma}_U^2(k) = \frac{1}{M-1}\sum_{l=1}^{M}|U^{[l]}(k) - \hat{U}(k)|^2$$
$$\hat{\sigma}_Y^2(k) = \frac{1}{M-1}\sum_{l=1}^{M}|Y^{[l]}(k) - \hat{Y}(k)|^2 \tag{4.11}$$
$$\hat{\sigma}_{YU}^2(k) = \frac{1}{M-1}\sum_{l=1}^{M}(Y^{[l]}(k) - \hat{Y}(k))\overline{(U^{[l]}(k) - \hat{U}(k))}$$

Calculating the sample noise variance (in other words, uncertainty) of maximum likelihood FRF estimate, $\hat{G}_{ML}(j\omega_k)$ gives

$$\hat{\sigma}_G^2(k) = \frac{1}{M-1}\sum_{l=1}^{M}|G^{[l]}(k) - \hat{G}_{ML}(k)|^2 \tag{4.12}$$

where $\hat{G}_{ML}(k)$ is given in (4.10) and $G^{[l]}(k) = Y^{[l]}(k)/U^{[l]}(k)$.

4.4 Measurement Results

4.4.1 Zero input experiment, a simple noise analysis

Before realizing FRF measurements, it makes sense to observe system behavior under zero input. When plant is not excited (zero input), the process noise, $n_p(t)$ declines almost to zero. The output signal, $y(t)$ consists mostly of the sensor measurement noise, $m_y(t)$ (see Fig. 2.2 on page 10). This zero input case can not be considered as normal operating conditions; therefore noise calculated here would be misleading. But still, it gives a good insight about the output sensor noise, $m_y(t)$.

In this experiment, zero input is applied to the system and the output signal is measured in the time domain for 50 seconds. The input and output signals in units of "degree/sec" are given in Fig. 4.1. The measurement system sampling frequency $T_s = 3000$ Hz is higher than the gyro sensor update rate, 400 Hz. Therefore, Fig. 4.1 resembles a zero-order hold (ZOH) graph. From this figure, it is observed that peak to peak of output signal is approximately between ±0.050 degree/seconds.

For a further examination, the DFT of output signal is calculated. Magnitude spectrum of the output signal, $y(t)$ in decibels, is given in Fig 4.2 with frequency resolution $f_0 = 0.02$ Hz. The variance of the output signal, $\hat{\sigma}_Y^2(k)$, with number of averages $M = 25$ and frequency resolution $f_0 = 0.5$ Hz, is given in Fig. 4.3. It is observed that, noise level is decreasing as frequency increases in the frequency band of interest. At certain frequencies, small peaks are observed on the output magnitude spectrum. After examining the measurement setup, it is concluded that the cooling fan at the backward of the mechanical system, turning at around $f = 30.9$Hz is the reason of peaks in magnitude spectrum.

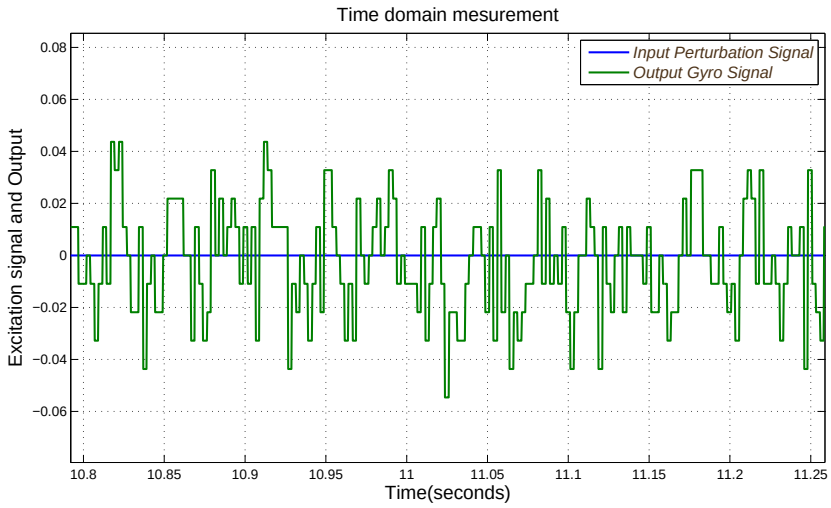

Figure 4.1: Output signal, $y(t)$ in the time domain under zero input signal which gives an idea about output noise peak to peaks

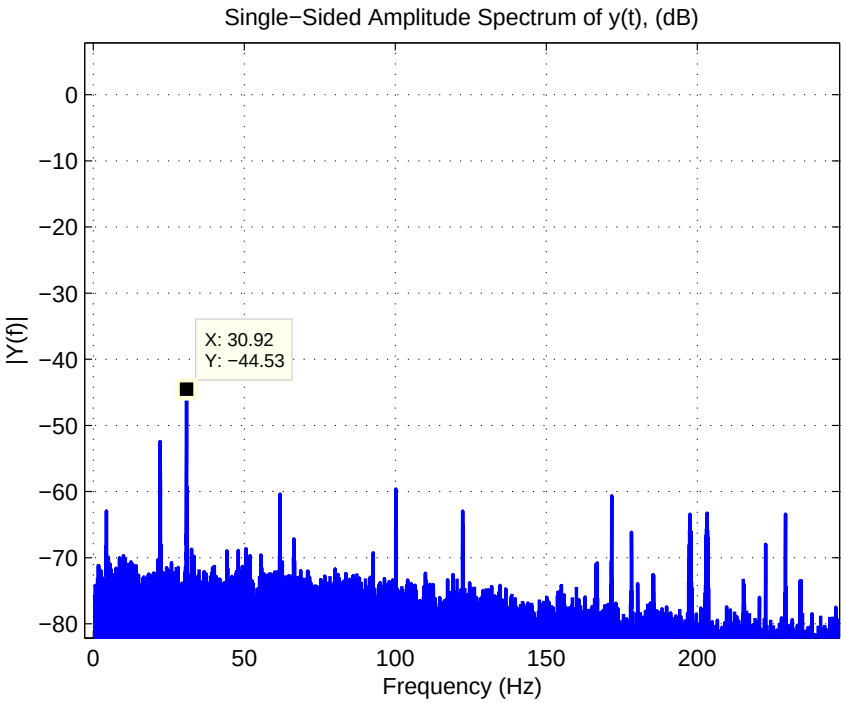

Figure 4.2: Output magnitude spectrum under zero input which gives an idea about output noise

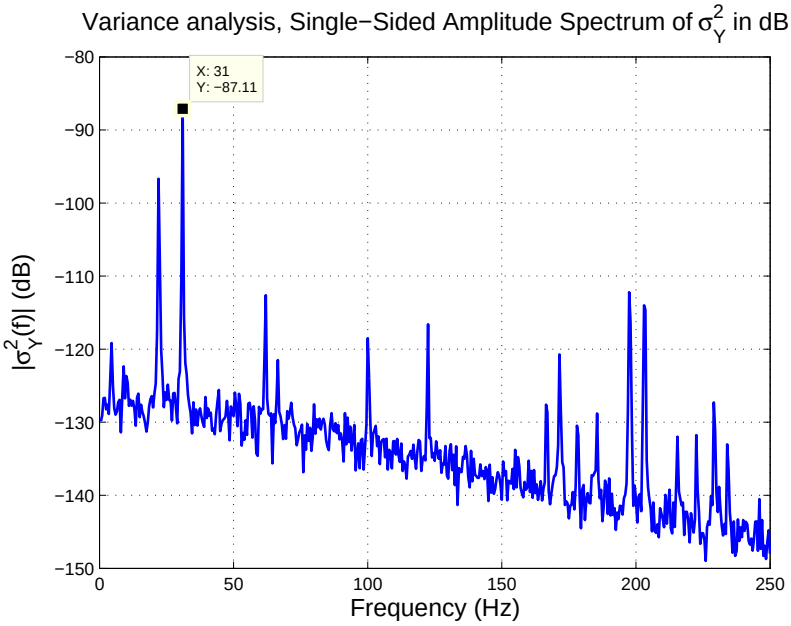

Figure 4.3: Output variance spectrum under zero input with frequency resolution $f_0 = 0.5$ Hz

4.4.2 Multisine experiment

In this experiment, the excitation signal setup explained in Section 3.5 on page 23 is used. Under the perturbation signal, first, $T_w = 15$ seconds are waited, allowing the transients of the plant and the measurement system to disappear. After the waiting time, $M = 75$ signal periods are applied resulting in $T = MT_0 = 150$ seconds transient free measurement duration. Length of the transient free measured signal is $L = T/T_s = 450000$. In Fig. 4.4, some part of the time domain input and output signals are displayed. In Fig. 4.5, the integral of the gyro output signal is displayed which shows the position of inner azimuth gimbal in degrees. The perturbation signal used in this experiment excites a limited frequency bandwidth ([0.5, 250] Hz in this experiment, see Section 3.5 on page 23); therefore the frequencies outside the bandwidth are discarded. In Figures 4.6, 4.7, 4.8, 4.9 the noise variances are displayed. Note that, since input is known exactly, σ_U^2 and σ_{YU}^2 are zero. After FFTs and averaging, measured frequency response function can be seen in Fig. 4.10. The comparison of this measurement with other nonparametric FRF measurements is given in Fig. 4.25. The comparison of the estimated FRF variances is shown in Fig. 4.26.

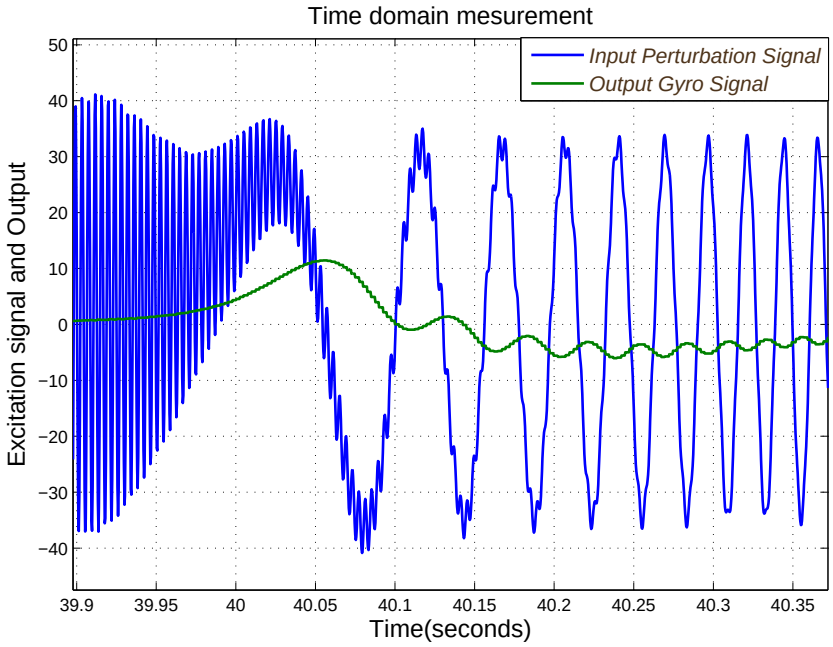

Figure 4.4: Multisine experiment time domain input and output signals

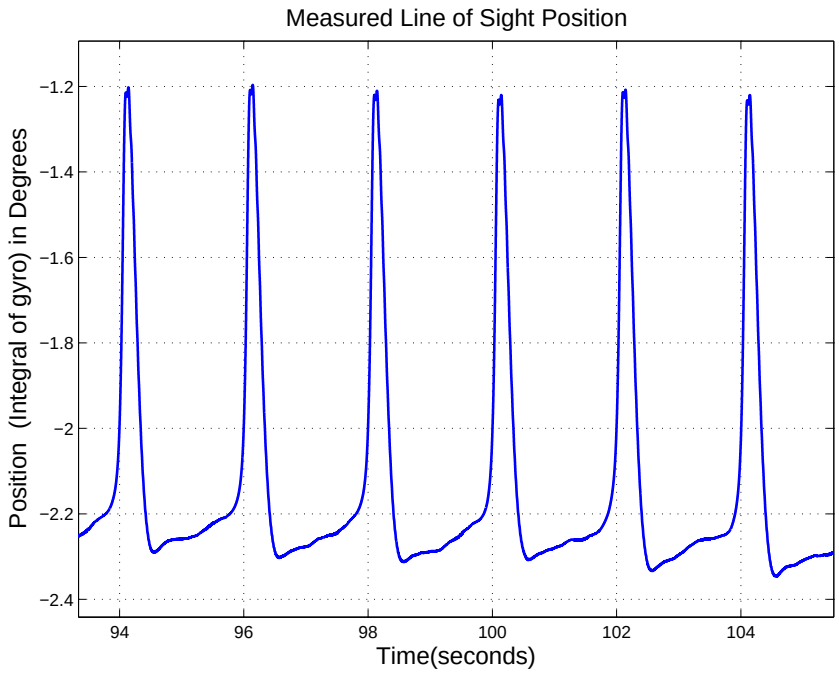

Figure 4.5: Multisine experiment integral of the gyro output which shows the position of inner azimuth gimbal

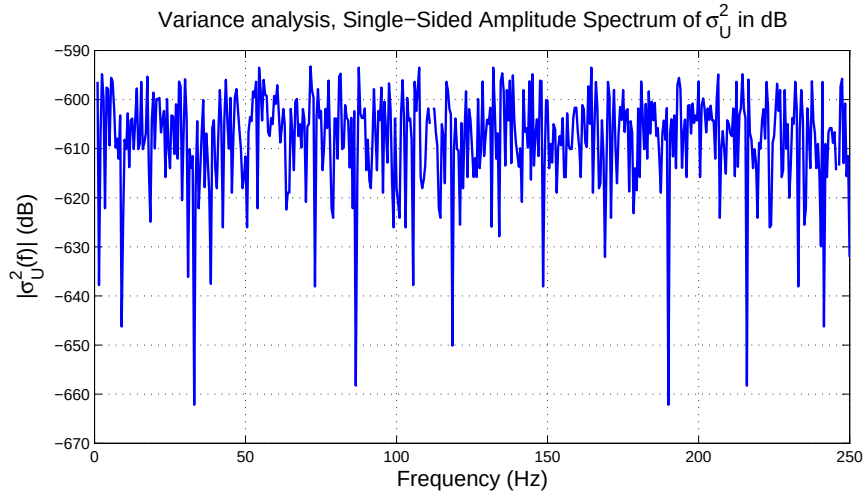

Figure 4.6: Multisine experiment input noise variance

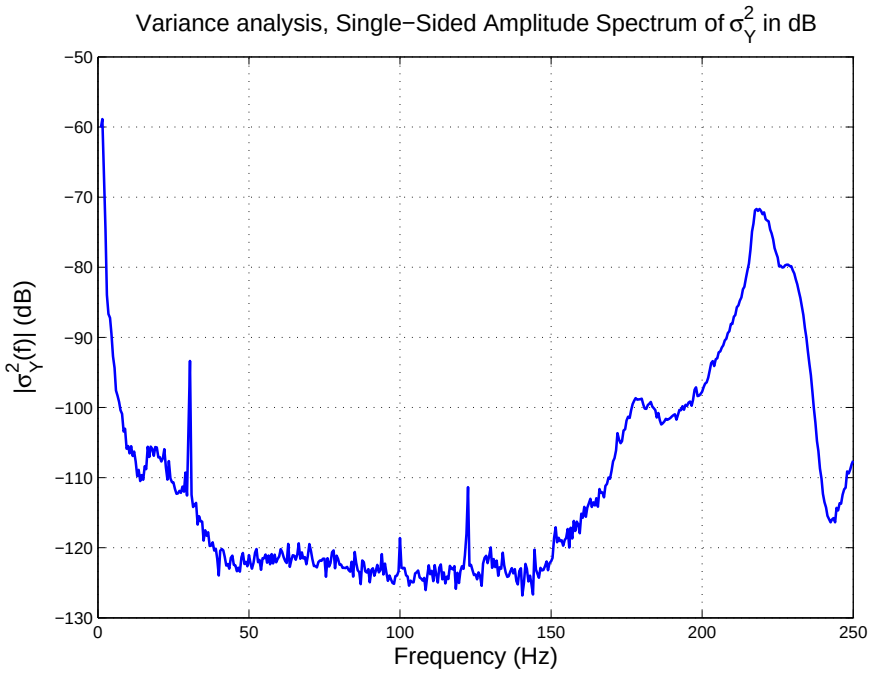

Figure 4.7: Multisine experiment output noise variance

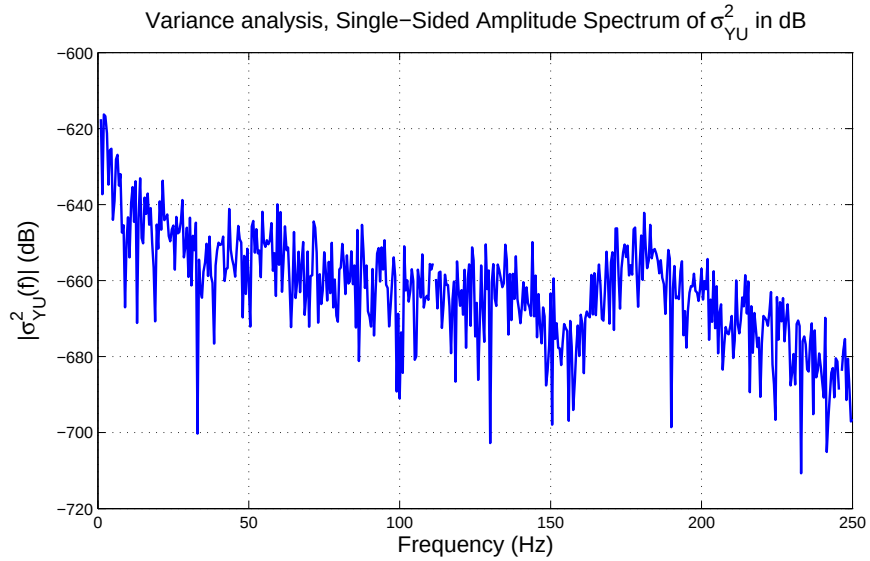

Figure 4.8: Multisine experiment input-output noise covariance

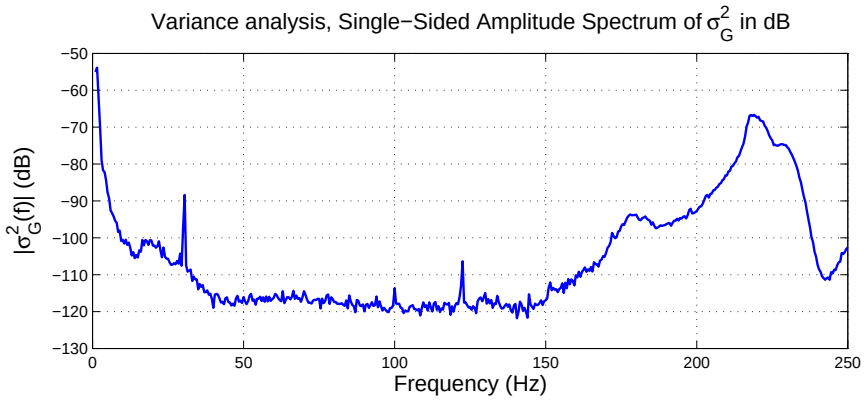

Figure 4.9: Multisine experiment input-output noise covariance

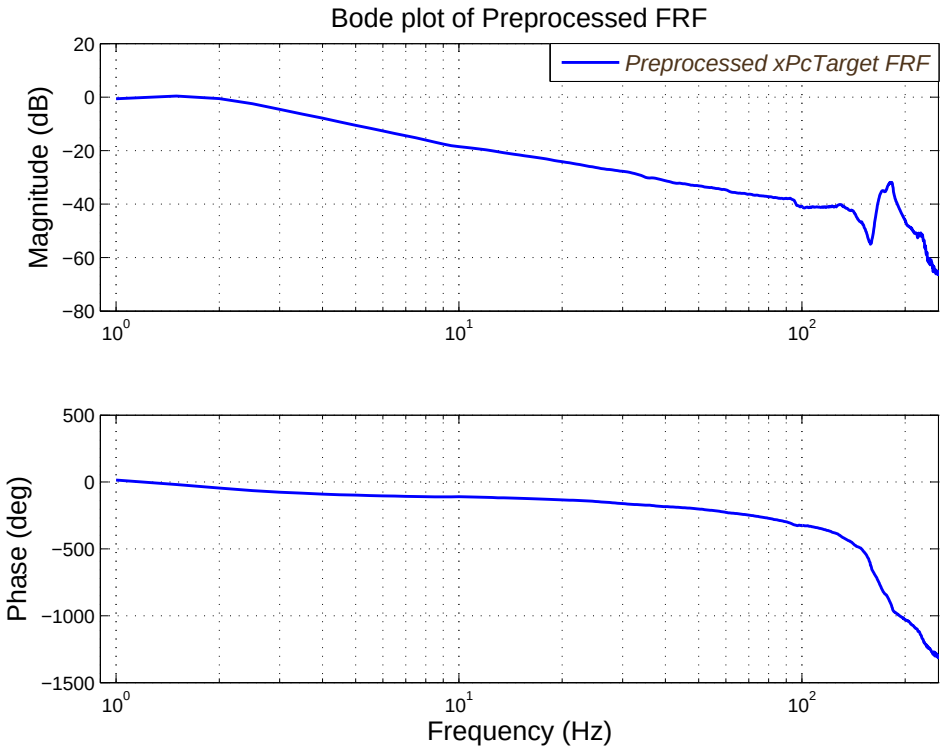

Figure 4.10: Multisine experiment frequency response function measurement

4.4.3 Pseudo random binary sequence experiment

In this experiment, the excitation signal setup explained in Section 3.6 on page 25 is used. Under the perturbation signal, first $T_w = 15$ seconds are waited allowing the

transients of the plant and the measurement system to disappear. After the waiting time, $M = 75$ signal periods are applied resulting in $T = MT_0 = 155.3$ seconds transient free measurement duration. Length of the transient free measured signal is $L = T/T_s = 465900$. In Fig. 4.11, some part of the time domain input and output signals are displayed. In Fig. 4.12, the integral of gyro output signal is displayed which shows the position of inner azimuth gimbal in degrees. The perturbation signal used in this experiment excites a limited frequency bandwidth ([0.48, 300] Hz in this experiment, see Section 3.6 on page 25); therefore the frequencies outside the bandwidth are discarded. In Figures 4.13, 4.14, 4.15, 4.16 the noise variances are displayed. Note that, since input is known exactly, σ_U^2 and σ_{YU}^2 are zero. After FFTs and averaging, measured frequency response function can be seen in Fig. 4.17. The comparison of this measurement with other nonparametric FRF measurements is given in Fig. 4.25. The comparison of the estimated FRF variances is shown in Fig. 4.26.

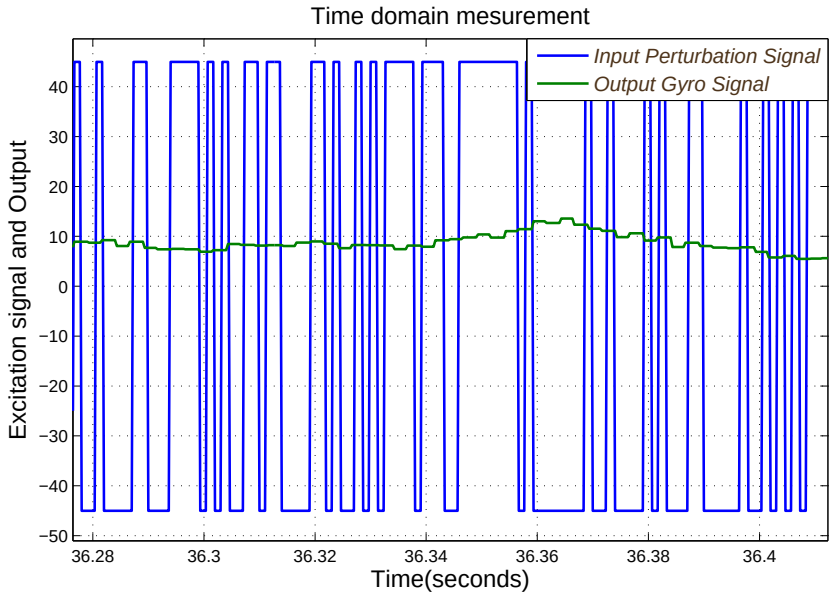

Figure 4.11: PRBS experiment time domain input and output signals

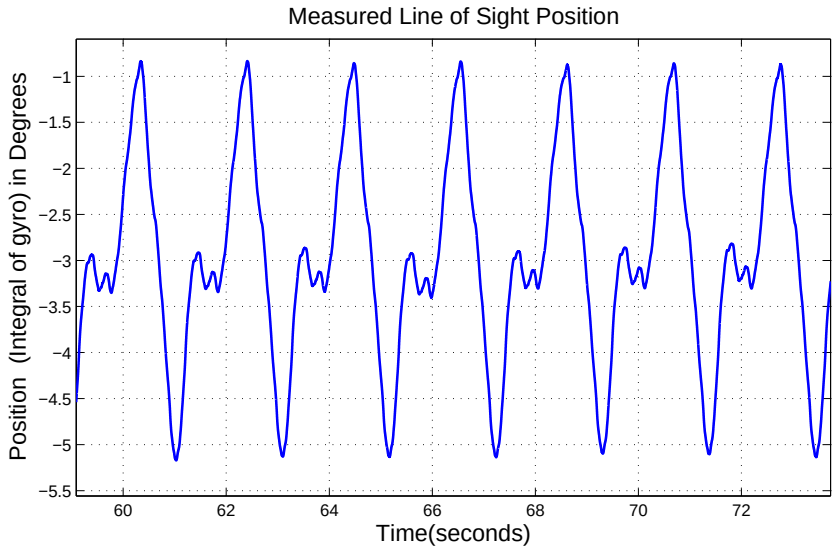

Figure 4.12: PRBS experiment integral of the gyro output which shows the position of inner azimuth gimbal

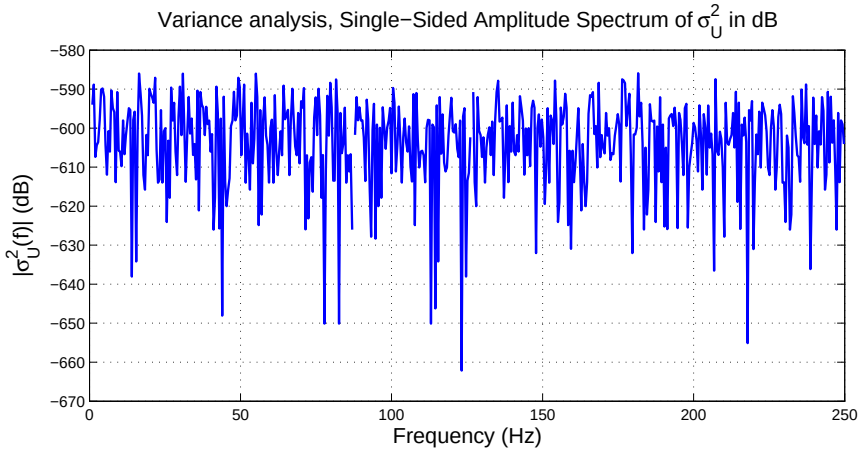

Figure 4.13: PRBS experiment input noise variance

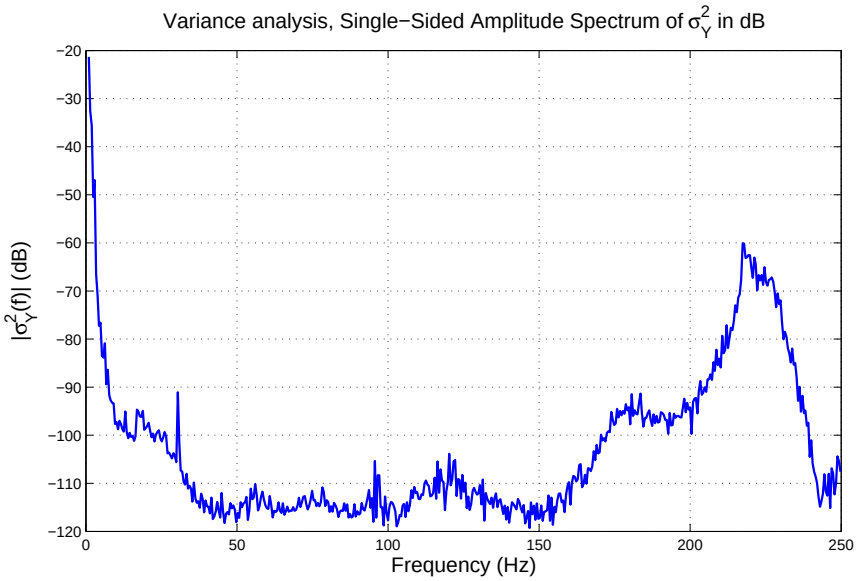

Figure 4.14: PRBS experiment output noise variance

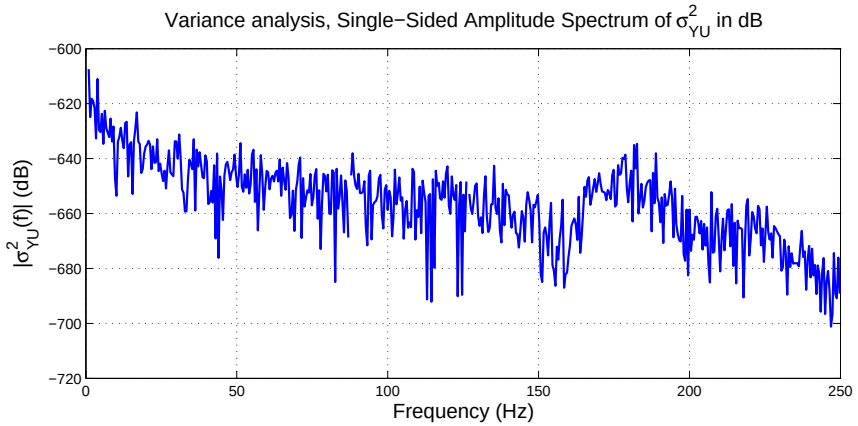

Figure 4.15: PRBS experiment input-output noise covariance

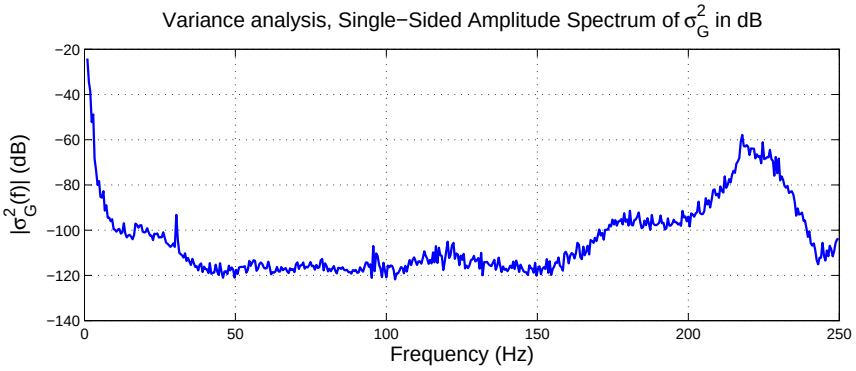

Figure 4.16: PRBS experiment input-output noise covariance

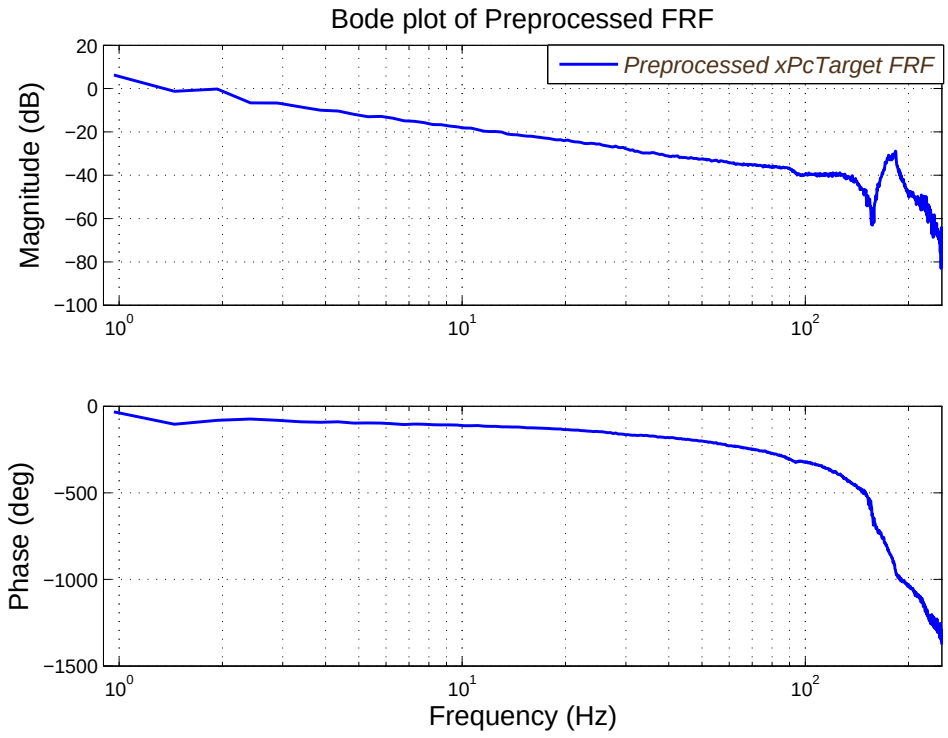

Figure 4.17: PRBS experiment frequency response function measurement

4.4.4 Swept sine experiment

In this experiment, the excitation signal setup explained in Section 3.7 on page 28 is used. Under the perturbation signal, first $T_w = 15$ seconds are waited allowing the transients of the plant and the measurement system to disappear. After the waiting

time, $M = 75$ signal periods are applied resulting in $T = MT_0 = 150$ seconds transient free measurement duration. Length of the transient free measured signal is $L = T/T_s = 450000$. In Fig. 4.18, some part of the time domain input and output signals are displayed. In Fig. 4.19, the integral of gyro output signal is displayed which shows the position of inner azimuth gimbal in degrees. The perturbation signal used in this experiment excites a limited frequency bandwidth ([0.5, 250] Hz in this experiment, see Section 3.7 on page 28); therefore the frequencies outside the bandwidth are discarded. In Figures 4.20, 4.21, 4.22, 4.23 the noise variances are displayed. Note that, since input is known exactly, σ_U^2 and σ_{YU}^2 are zero. After FFTs and averaging, measured frequency response function can be seen in Fig. 4.24. The comparison of this measurement with other nonparametric FRF measurements is given in Fig. 4.25. The comparison of the estimated FRF variances is shown in Fig. 4.26.

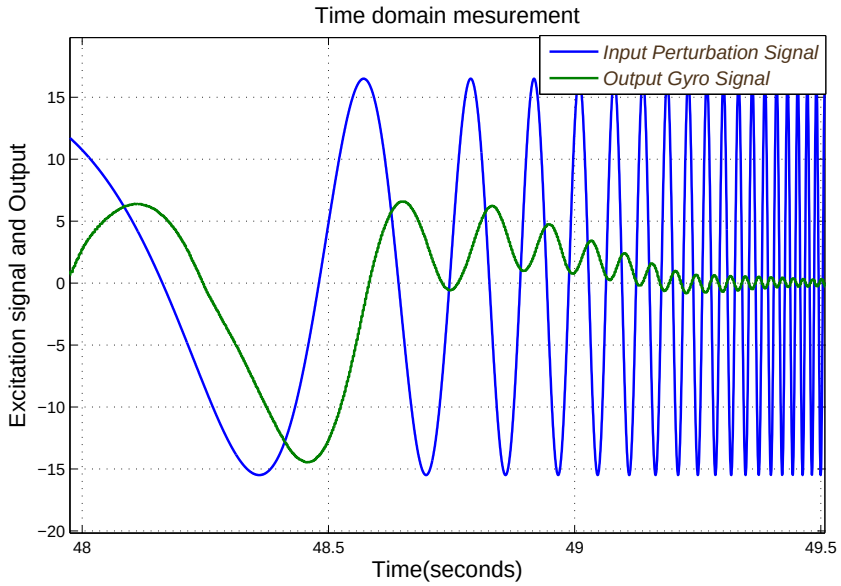

Figure 4.18: Swept Sine experiment time domain input and output signals

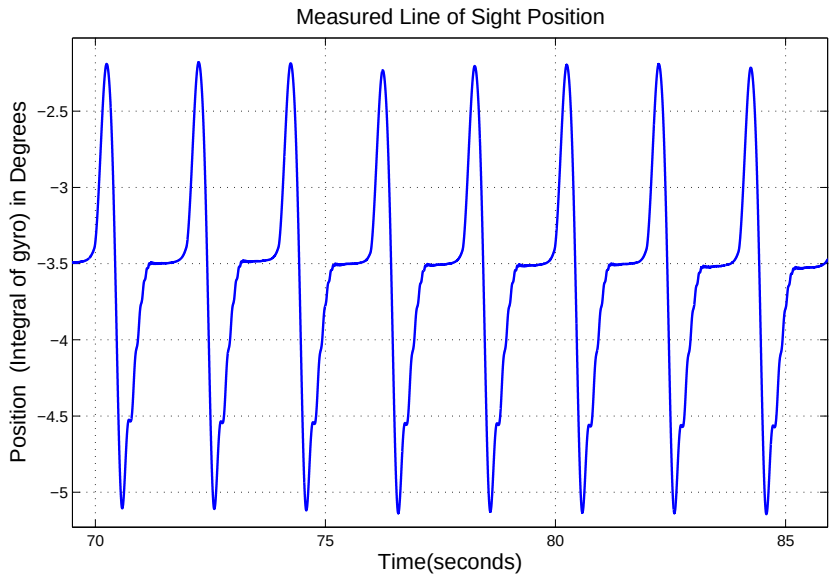

Figure 4.19: Swept Sine experiment integral of the gyro output which shows the position of inner azimuth gimbal

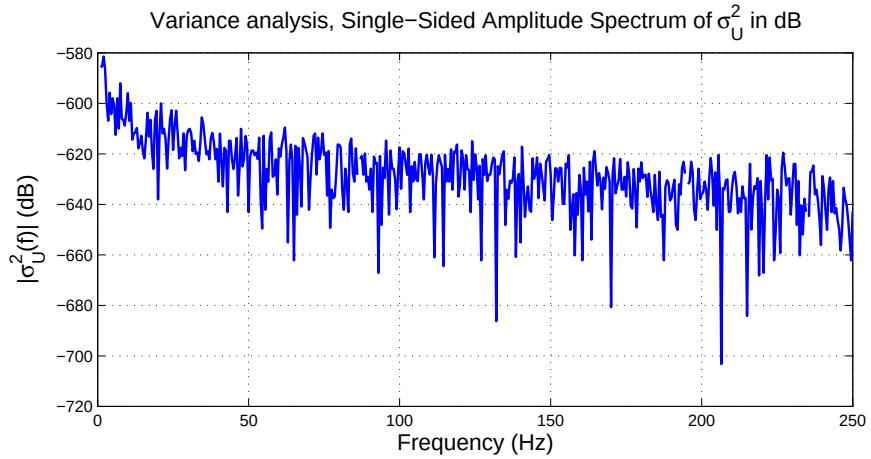

Figure 4.20: Swept Sine experiment input noise variance

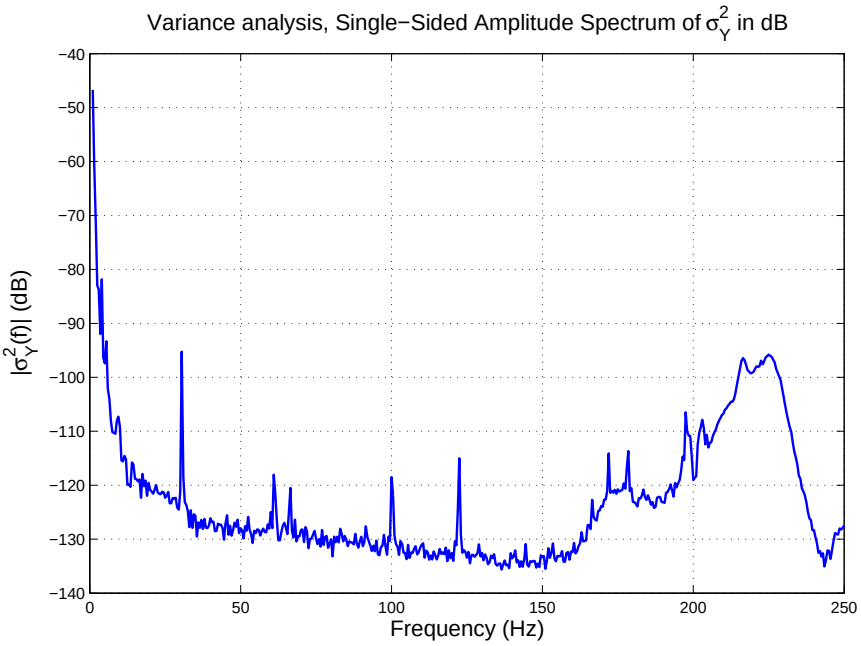

Figure 4.21: Swept Sine experiment output noise variance

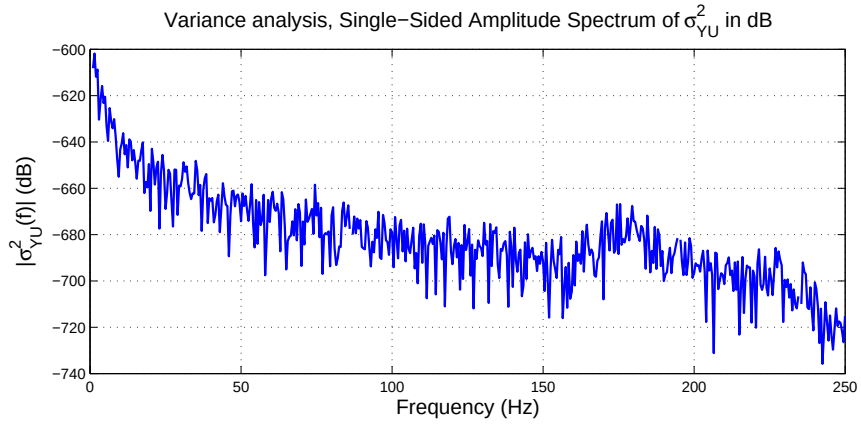

Figure 4.22: Swept Sine experiment input-output noise covariance

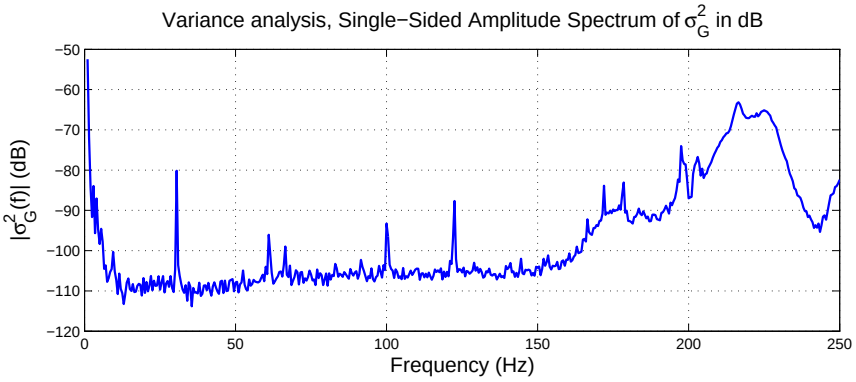

Figure 4.23: Swept Sine experiment input-output noise covariance

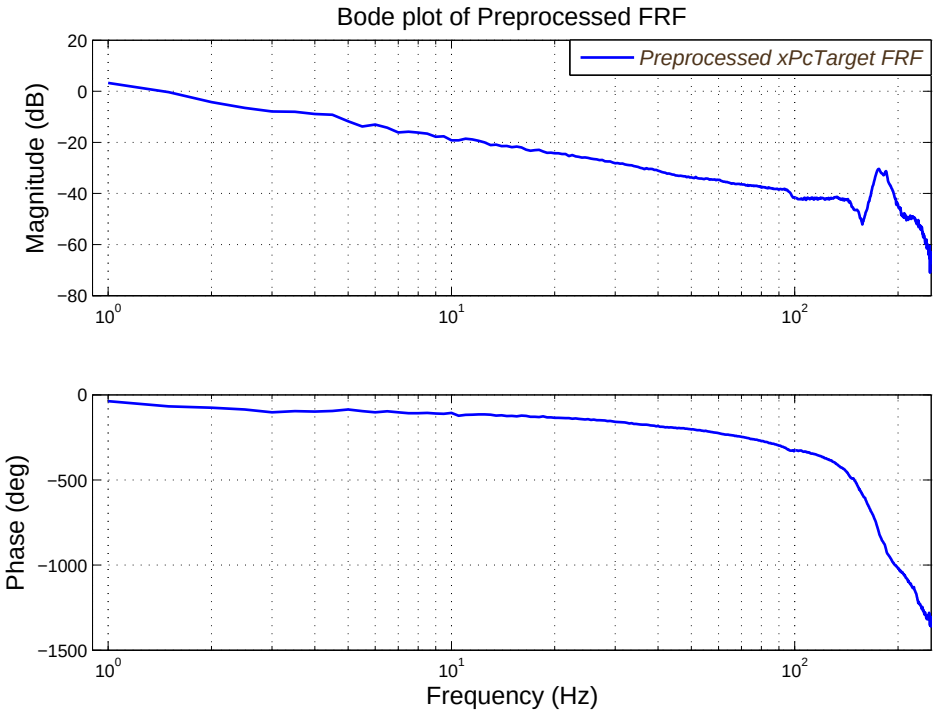

Figure 4.24: Swept Sine experiment frequency response function measurement

4.4.5 Comparisons of measurements

In this section, Schroeder multisine, PRBS and swept sine experiments are compared. The comparison of nonparametric FRF estimates, $\hat{G}(j\omega_k)$ is given in Fig. 4.25. From the figure of magnitude spectrum, it is observed that amplitude decays with a slope of

−20 dB/decade. At the frequency around 179 Hz, there exists a mechanical resonance region in which the plant responds with a higher amplitude than it does at other frequencies. In the phase spectrum, it should be noted that, the phase rapidly drops at higher frequencies. This fast phase drop at higher frequencies indicates the existence of a time delay in the system (this delay will be estimated later in Chapter 7). The noise (variance) spectrum of FRF estimates can be examined in Fig. 4.26. In the noise spectrum, notice that at frequency $f = 30.9$ Hz, a small peak is observed. After examining the measurement setup, it is concluded that the cooling fan at the backward of mechanical system, turning at around $f = 30.9$Hz is the reason of peaks in the noise spectrum.

The three FRF measurement results overlap in most of the frequency band of interest except at low frequencies ($f < 5$ Hz). That is because, at low frequencies, process noise due to undesired disturbances (such as friction) dominates and for the output signal, SNR becomes poor. Noise spectrum clearly shows the increased variance at lower frequencies ($f < 5$ Hz) in Fig. 4.26. In order to achieve better FRF measurements (with minimum variance and bias), SNR should be kept high enough over all frequency band of interest, while satisfying device specific constraints. The optimization of excitation signal concept in terms of crest factor and other device specific criteria is deeply analyzed in Section 3.8 on page 30.

Considering the noise spectra in Fig. 4.26, the success of each experiment can be compared in terms of uncertainty of the FRF measurements. It is observed that at low frequency interval $f < 28$ Hz, the swept sine FRF measurement uncertainty is smaller. On the other hand, at higher frequencies $f > 28$ Hz, the Schroeder multisine and PRBS FRF measurement uncertainties are lower. The reason of difference between each noise estimate is mostly due to different levels of SNRs each designed excitation signal provides (periodic signals are designed in Sections 3.5, 3.6 and 3.7). As a summary, the three FRF measurement experiments give mostly similar results. For this reason, experimenter can choose one of the general purpose periodic excitation signal depending on his or her preference. The crucial point is, designed signal should provide adequately high SNR without exceeding normal operating conditions. Another critical point is, excitation signal should be periodic in order to minimize spectral leakage errors (leakage error concept is discussed in Section 3.3 on page 18).

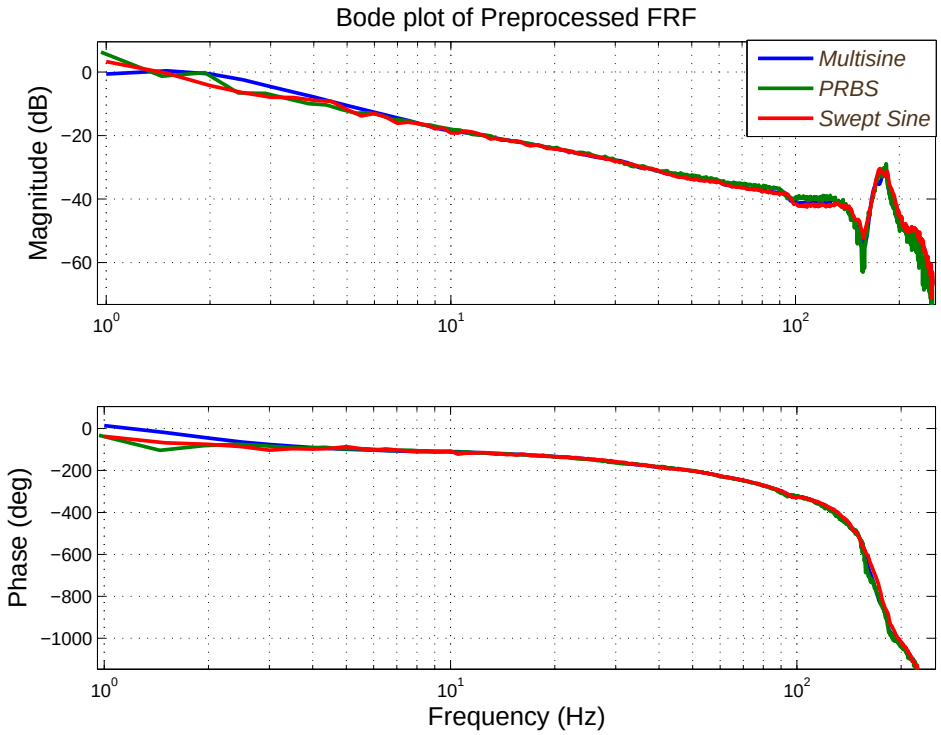

Figure 4.25: Comparison of nonparametric FRF of Multisine, PSRB and Swept Sine experiments

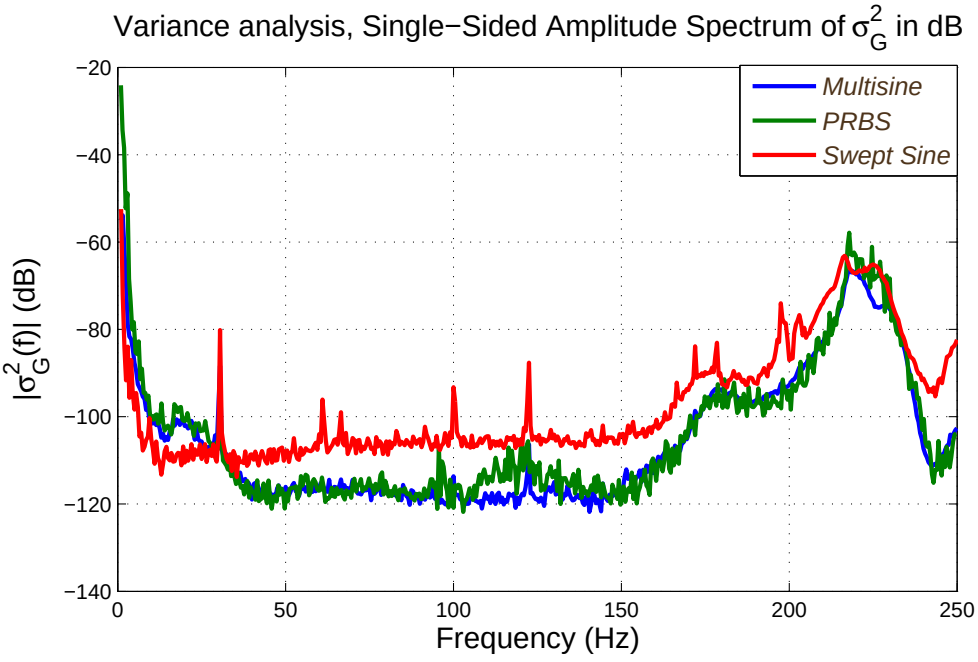

Figure 4.26: Comparison of frequency response measurement variance of Multisine, PSRB and Swept Sine experiments

CHAPTER 5

DETECTION AND QUANTIFICATION OF NONLINEAR DISTORTIONS

5.1 Introduction

All mechanical systems are inherently nonlinear in nature. The aim of this chapter is not to model nonlinear systems, but to detect and measure them. Nonlinear model building is possible using describing functions or Volterra series [12], but difficult to manage and time consuming while the profits are usually small. For this reason, it is appealing to approximate the nonlinear system by linear equations around the operating point of interest. Detecting and measuring the nonlinear distortions allow a better understanding and gives an intuitive insight of the error sources on frequency response function (FRF) measurements. Knowing the nonlinear distortion error contribution on FRF measurement helps a robust controller designer to set the uncertainty bounds on a linear model and improve the existing controller.

Note again that, this study does not deal with nonlinear model building, but it covers the detection and quantification of nonlinear distortions on FRF measurements. The sources of nonlinear distortions include the followings:

- The static and kinetic frictions in servomechanisms are usually a major concern in FRF measurements. In Section 5.6, it is observed that, in low frequencies, stochastic nonlinear distortions are the dominant error source which indicates strong presence of friction.
- Unbalance of gimbal is another nonlinear distortion. It happens when the center

of rotation does not coincide with the center of mass.

- Spring torques from cable wraps may behave as nonlinear distortion error sources.

- Around mechanical resonance frequencies, nonlinear distortions are usually huge.

- If the angular position of the inner azimuth gimbal exceeds ±5°, gimbal will hit the mechanical edge of the system and another nonlinear distortion will arise (see Section 2.4 on page 12).

This chapter is structured as follows. First, the detection techniques for nonlinear distortions are discussed. Next, the class of perturbation signals used in this chapter is defined. The theory of linear representation of nonlinear systems is given for continuous systems operating in open loop. A practical technique, called "Robust Method" for measuring the best linear approximation (BLA), its noise variance, and the level of nonlinear distortion is described. Finally, a robust method is applied on the real system and the experimental results are analyzed.

5.2 Literature Review for Nonlinearity Detection Methods

A nonlinearity detection method answers the following questions: "Is the system under investigation linear or nonlinear?" and "What is the level of the nonlinear distortions present in this system?". In [13, 14], many nonlinear system detection techniques for single-input-single-output plants are described. Here, only a few of them will be briefly discussed, summarizing their advantages and disadvantages.

The Superposition Principle: A simple method is to scale the input $u(t) \rightarrow \lambda u(t)$ and check whether the output also scales with λ. The *superposition principle* states that, for all linear systems, the net response at a given time caused by two or more inputs is the sum of the responses which would have been caused by each input individually. The homogeneity and additivity properties together are

called the superposition principle.

$$F(x_1 + x_2 + \ldots) = F(x_1) + F(x_2) + \ldots \qquad Additivity \qquad (5.1)$$

$$F(\lambda x) = \lambda F(x) \qquad Homogeneity \qquad (5.2)$$

A system behaves nonlinearly when this superposition principle is violated. Drawbacks of this method are, it is time consuming since a lot of measurements with different excitation levels are needed and it is extremely sensitive to all possible measurement errors due to no noise identification process.

Stepped Sine Test: *Stepped Sine* test is a very simple method for detecting nonlinear distortion where the plant is excited with a single sinusoidal signal with frequency f. If the system under investigation is linear, in the output frequency spectrum we should observe response only at the frequency f (besides noise among other frequencies). The presence of higher harmonics $(2f, 3f, \ldots)$ in the output frequency response spectrum is an indicator of nonlinear behavior of the system.

This method is tested on the inner azimuth gimbal of the real mechanical system. System is perturbed with a single sinusoidal signal with frequency $f = 1.5$Hz. Under perturbation signal, $T_w = 6$ seconds are waited allowing the transients of the plant and the measurement system to disappear. After waiting for 6 seconds, system is measured for $T = 80$ seconds. Sampling frequency of the system, f_s is 3kHz and sampling period is 1/3000 seconds from $T_s = 1/f_s$. Hence, the length of the transient free measured signal is $L = T/T_s = 240000$. $M = 4$ averages is applied on the output spectrum to reduce the influence of noise . Figure 5.1 shows the results of the experiment. At higher excitation levels, the contribution of the 2nd and 3rd harmonic components ($2f = 3$Hz and $3f = 4.5$Hz) in the output spectrum can be observed. For instance, 2nd harmonic reveals that nonlinearity distortion at 3Hz is approximately 40dB higher than the noise while 22dB less than the signal magnitude response at the fundamental harmonic $f = 1.5$Hz.

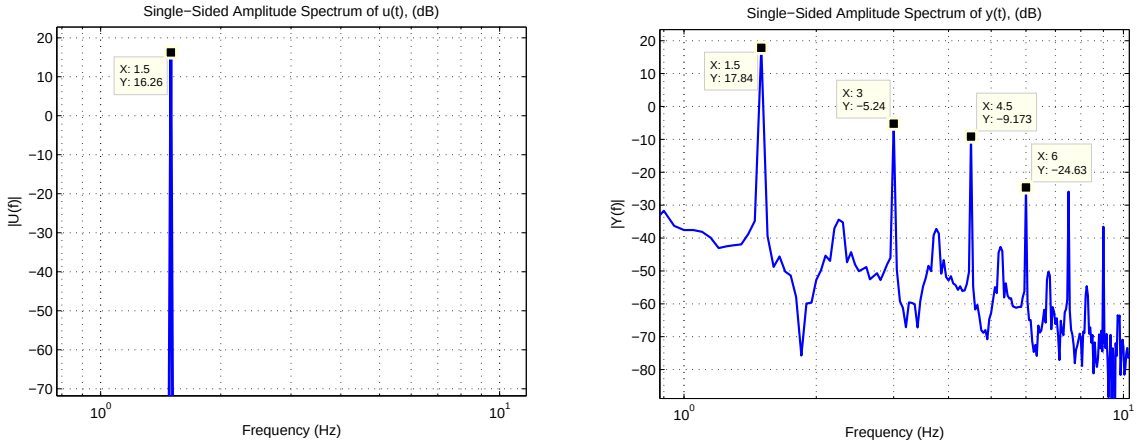

Figure 5.1: *Left Figure*: Input signal magnitude spectrum. Only 1.5Hz is excited. *Right Figure*: The presence of higher-harmonics in the output spectrum points out the nonlinearity distortion

The main drawback of this method is, it is very slow since it requires independent measurements for each frequency component (see Section 3.4 on page 20).

The Coherence Function: *The spectral coherence* is a statistic that can be used to examine the relation between two signals or data sets. It is commonly used to estimate the power transfer between input and output of a linear system. The coherence function measures how much of the output power is coherent (linearly related) with the input power [3]. It is defined as:

$$\gamma^2(\omega) = \frac{|S_{yu}(j\omega)|^2}{S_{uu}(j\omega)S_{yy}(j\omega)}\,, \quad 0 \leq \gamma^2(\omega) \leq 1 \tag{5.3}$$

where $S_{uu}(j\omega)$ and $S_{yy}(j\omega)$ are auto-power spectrum of $u(t)$ and $y(t)$ respectively. $S_{yu}(j\omega)$ is cross-power spectrum of $u(t)$ and $y(t)$. $\gamma^2(\omega)$ is equal to unity in the ideal case. If $\gamma^2(\omega)$ is less than 1, it can be due to presence of following four items [13]:

- Extraneous noise in the measurements,
- Spectral leakage errors of DFT (see Section 3.3 on page 18),
- A nonlinear distortion (only for random excitations),
- Other inputs besides $u(t)$ contributing to the output.

Main disadvantage of this technique is, it is not applicable for periodic excitations. When a periodic perturbation signal is used, in the absence of noise

($\sigma_U^2(k) = 0$, $\sigma_Y^2(k) = 0$ and $\sigma_{YU}^2(k) = 0$) coherence is unity even if the system under investigation is purely nonlinear [3]. Another drawback of this method is that, it does not distinguish noise disturbances from nonlinearity distortions. To overcome this, sufficient number of averages have to be evaluated in order to reduce the influence of extraneous noise in the measurements; so that nonlinearity distortion becomes dominant.

NPR: Non-causal Power Ratio: *The non-causal power ratio* (NPR) method is a causality method that detects and quantifies system nonlinearities in one single number [13]. The method relies on the following decomposition

$$g(t) = \mathrm{DFT}^{-1}\{G(j\omega)\} = g_n(t) + g_c(t) \tag{5.4}$$

where $G(j\omega)$ is the FRF measurement of the system, $g_c(t)$ is the *causal part* and $g_n(t)$ is the *non-causal part* defined by

$$g_c(t) = \begin{cases} g(t), & t \geq 0 \\ 0, & t < 0 \end{cases} \qquad g_n(t) = \begin{cases} 0, & t \geq 0 \\ g(t), & t < 0 \end{cases} \tag{5.5}$$

The non-causal power ratio (NPR), is then defined as the ratio of non-causal power P_n to the total FRF power P [14]. NPR is given by Eqn. (5.6):

$$NPR = \frac{P_n}{P} = \frac{\int_{-\infty}^{0} |g_n(t)|^2 \, \mathrm{d}t}{\int_{-\infty}^{\infty} |g(t)|^2 \, \mathrm{d}t} \qquad 0 \leq NPR \leq 1 \tag{5.6}$$

NPR value grows with increasing nonlinearity, allowing the quantification of the level of nonlinear distortion. The disadvantage of this technique is that, it represents the level of nonlinear distortions in one single number. Therefore, this method provides no information about the relationship between the nonlinearity level and frequency.

In system identification, the prime interest of an engineer is measuring the FRF of the system. Detecting and quantifying nonlinearity distortion is of secondary interest for an engineer. For this reason, the optimal FRF-measurement method should not sacrifice FRF measurement quality in order to detect nonlinearity distortions. Therefore, most of the nonlinearity detection methods in the literature are not suitable for our purpose, since they spend most of the time on detecting nonlinearity, not FRF measurements. However, when random phase multisine excitations are applied, both

FRF measurement and nonlinearity detection is realized in good quality [3]. In the following sections, a nonlinearity test based on random phase multisine excitations will be presented. This method does not suffer from the aforementioned problems.

5.3 Random Phase Multisine Excitation Signals

It is suggested to use random phase multisines as perturbation signals because they provide a better SNR (less sensitive to disturbing noise and stochastic nonlinearities) and the detection of nonlinearities is much easier [15, 16]. This section starts with the definition of random phase multisine which is required in nonlinearity quantification method presented in Section 5.5. Then, a random phase multisine excitation signal is designed and it is applied on the real system.

Definition 5.3.1 (Random Phase Multisine) *A signal $u(t)$ is a normalized random phase multisine if*

$$\begin{aligned} u(t) &= F^{-1/2} \sum_{k=-F,\, k\neq 0}^{F} A_k e^{j2\pi f_0 k t} \\ &= F^{-1/2} \sum_{k=1}^{F} 2|A_k| \cdot \cos(2\pi f_0 k t + \underline{/A_k}) \end{aligned} \tag{5.7}$$

with $A_k = \bar{A}_{-k} = |A_k| e^{j\phi_k}$ ($\bar{x}$ denotes the complex conjugate of x). Phases $\phi_k = \underline{/A_k}$ is the realization of an independent uniformly distributed random process on $[0,\ 2\pi)$ such that $\mathbb{E}\{e^{j\phi_k}\} = 0$. $f_0 = \dfrac{1}{T_0}$ is frequency resolution with T_0 being signal period. There exists F frequency components in $u(t)$ and no DC component. In order to keep excitations with finite power as $F \to \infty$, the signals are scaled with $F^{-1/2}$, [17].

For the experiment of interest, six "Random Phase Multisine" signals are generated, two of them being given in this section. All six random phase multisine signals possess the same magnitude spectrum but have different phase spectra. These signals have the following properties.

- Signal period is $T_0 = 2$ seconds. Frequency resolution f_0 is 0.5 Hz from $f_0 = 1/T_0$.

- Sampling frequency of the system, f_s is 3kHz and sampling period is 1/3000 seconds from $T_s = 1/f_s$.
- Number of waves is $F - 2 = 498$ (0.5Hz and 1Hz frequency components are not excited). Discrete grid is $l_k = 1 : F = [3,4,5,\ldots,500]$ Therefore, from $f_k = l_k f_0$, excited frequency band is between 1.5Hz and 250Hz.
- At each random phase multisine signal generation, phase ϕ_k is independently uniformly distributed on $[0,\ 2\pi)$.
- The magnitude spectrum $|A_k|$ is designed such that signal to noise ratio (SNR) is at an acceptable level (for instance, at least an SNR of 40 dB is aimed for the experiment of interest).
- The crest factor for the "Random Phase Multisine" signal does not have a typical value. For the six experiments, the crest factor vary between $Cr(u) = 2.9$ and $Cr(u) = 3.8$ due to random behavior of phases in the signal (see Section 3.2 on page 17).

Designer may prefer not to excite some frequencies in the frequency band of interest. Non-excited frequency components are discarded in FRF measurements. In this experiment, two of the successive frequencies, 0.5Hz and 1Hz, are not excited, $|A_1| = 0,\ |A_2| = 0$. The reason is, when 0.5Hz and 1Hz are excited, the peak to peak value of line of sight angular position increases too much, exceeding $\pm 2^\circ$ degrees. The designer can avoid this by decreasing the overall magnitude spectrum at the expense of signal to noise ratio (SNR). However, sacrificing from SNR is not a desirable option. Therefore, it is better not to decrease the overall magnitude spectrum but measure the low and high frequency components independently. A_k is tuned in order to keep line of sight angle of the system between $\pm 2^\circ$ degrees which is the nominal operating condition. The magnitude spectrum for all of six random phase multisine signals are the same and can be examined from Fig. 5.2. Note that A_k is designed such that the injected power increases by 10dB/dec as frequency decreases (see magnitude spectrum in Fig. 5.2). It is observed from Fig. 4.26 on page 58 that at low frequencies, uncertainty is high in magnitude; hence it is reasonable to inject more power to low frequencies. The reason for this is to satisfy roughly the same SNR among the excited frequency band [4].

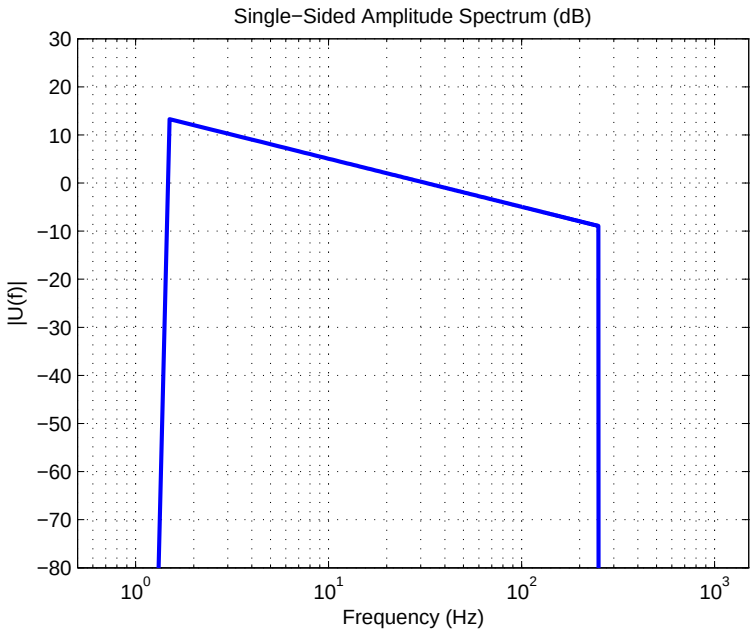

Figure 5.2: Random Phase Multisine signal magnitude spectrum (common for all six experiments)

In practice, the nonlinear distortions are detected in the presence of noise. Therefore, a number of consecutive periods of the steady state response is measured and the level of the total distortion (nonlinearity plus output noise) is compared with the noise sample standard deviation (see Section 5.5 for more details). Under the perturbation signal, $T_w = 6$ seconds are waited allowing the transients of the plant and the measurement system to disappear. After the waiting time, $M = 40$ signal periods are applied resulting in $T = MT_0 = 80$ seconds transient free measurement duration. Length of the transient free measured signal is $L = T/T_s = 240000$. This experiment with aforementioned settings is repeated 6 times using the random phase multisine signal, each signal having a different phase spectrum but the same magnitude spectrum. In Figures 5.3 and 5.5, certain portions of the time domain input and output signals are displayed for two of the six experiments. In Figures 5.4 and 5.6, the integral of gyro output signal is displayed which shows the position of the inner azimuth gimbal in degrees for two of the six experiments. Notice that, although the magnitude spectra are same, due to different phase spectra, excitation signals and system movement responses differ in terms of peak to peak value. As a matter of fact, it is possible to reduce the peak to peak value by optimizing phase spectrum without touching

magnitude spectrum.

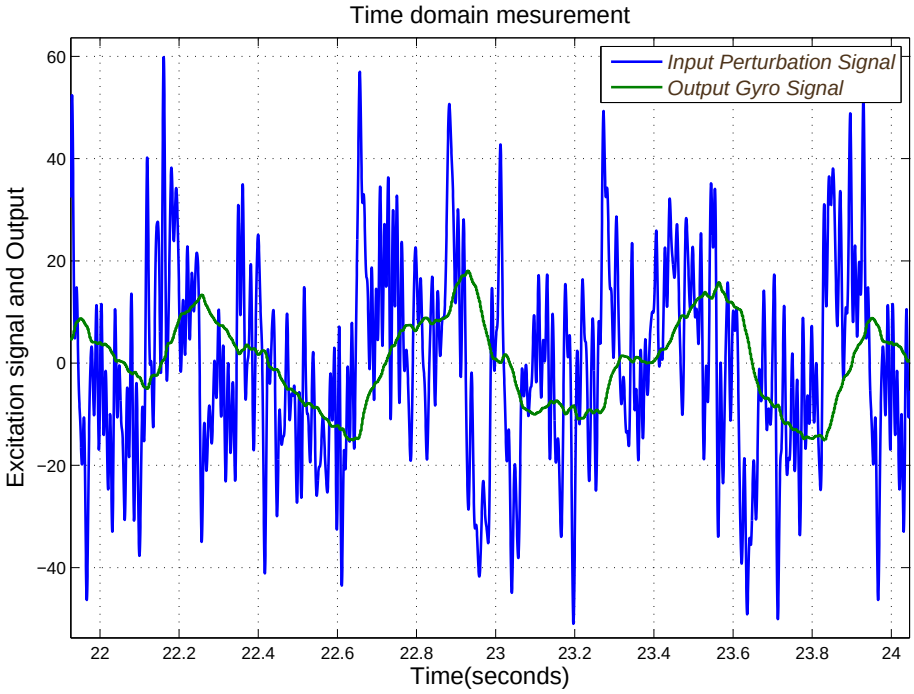

Figure 5.3: Random Phase Multisine experiment, time domain input and output signals for the test "1/6"

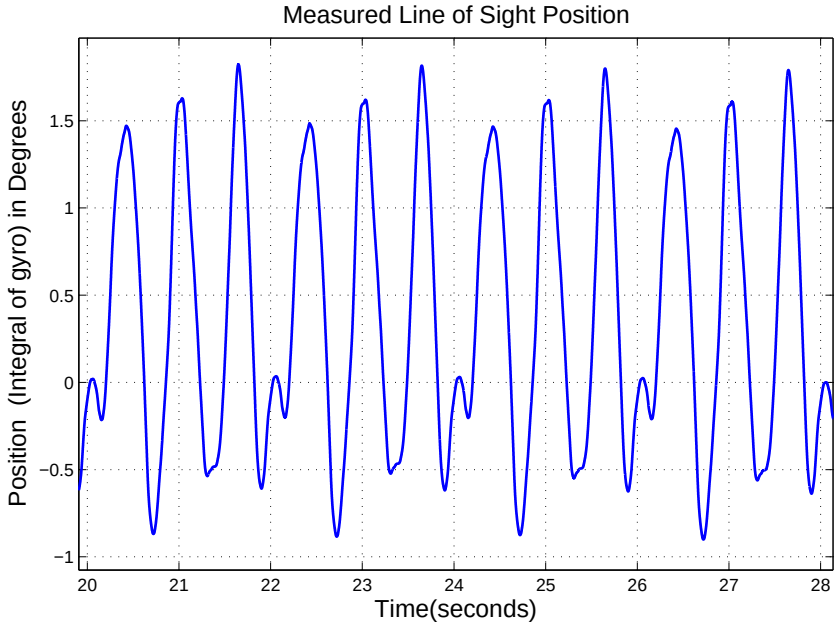

Figure 5.4: Random Phase Multisine experiment, integral of the gyro output which shows the position of inner azimuth gimbal for the test "1/6"

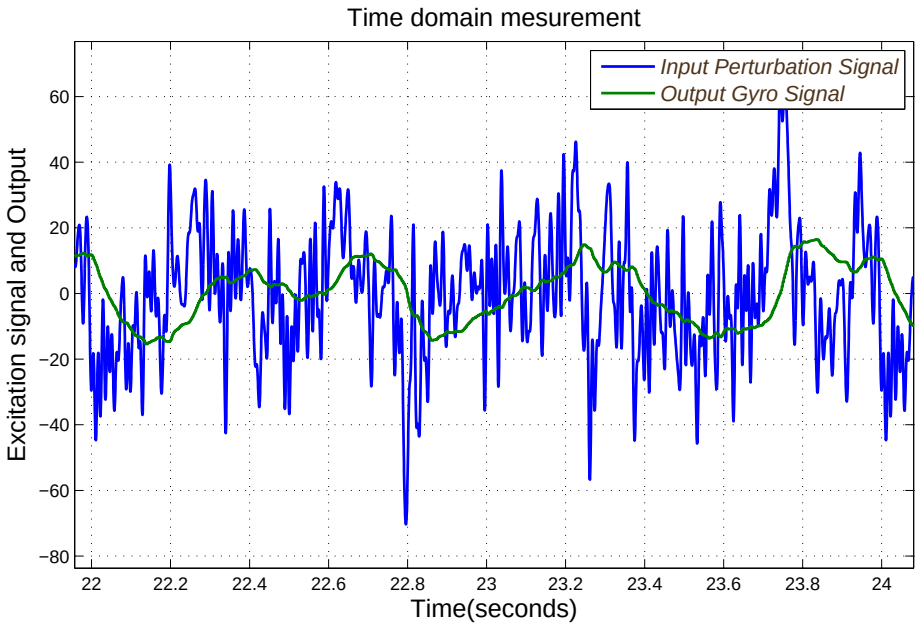

Figure 5.5: Random Phase Multisine experiment, time domain input and output signals for the test “2/6”

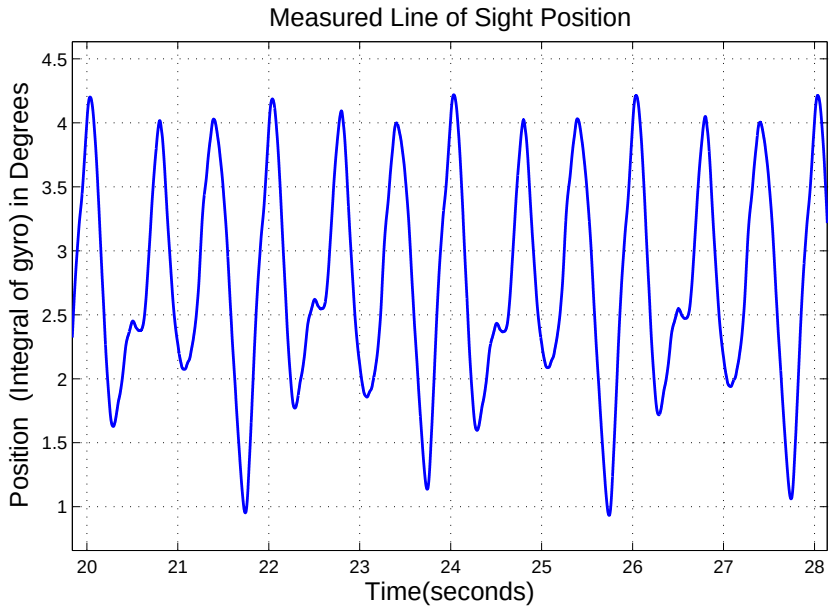

Figure 5.6: Random Phase Multisine experiment, integral of the gyro output which shows the position of inner azimuth gimbal for the test “2/6”

5.4 Linear Representation of a Nonlinear System

In [3, 17], it is shown that the measured output $y(t)$ of a nonlinear system consists of the output of a linear $y_L(t)$ plus a nonlinear $y_{NL}(t)$ contribution (See Fig. 5.7). It is assumed that the linear contribution dominates the nonlinear one for sufficiently small inputs:

$$\lim_{u_{rms}\to 0} \frac{(y_{NL})_{rms}}{(y_L)_{rms}} = 0 \tag{5.8}$$

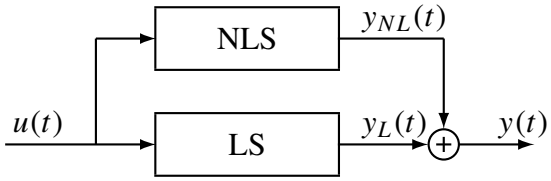

Figure 5.7: Nonlinear system consists of the underlying linear system + the systematic contributions of the nonlinear distortions

The goal of the measurements in this study is not to extract the underlying linear system (LS) in the global system (LS + NLS). The underlying linear system is useful for physical modeling. But our need is a model that describes the relation between the input and output for controller design purposes. Therefore the goal of the measurement is to find the best linear approximation (BLA) to the global system. BLA will be found by linearizing the global system around the operating point.

In [3, 16, 17], it is shown that for random excitations, FRF of a wide class of nonlinear systems can be represented as a sum of linear system + a nonlinear additive "noise source". This means that a nonlinear system given in Fig. 5.8 is equivalent to linear system with a noise source given in Fig. 5.9.

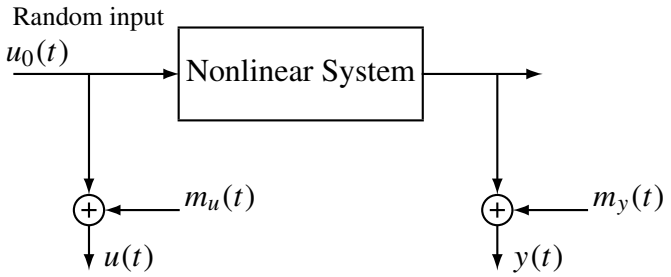

Figure 5.8: Nonlinear system measurement setup: $u_0(t)$ is true random input signal; $m_u(t)$, $m_y(t)$ are the input/output measurement errors.

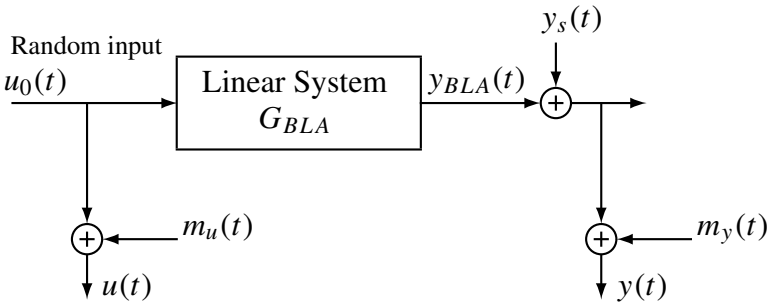

Figure 5.9: Measurement of the best linear approximation $G_{BLA}(s)$ of a nonlinear device: $u_0(t)$ is true random input signal; $m_u(t)$, $m_y(t)$ are the input/output measurement errors; $y_s(t)$ is the zero mean stochastic nonlinear contribution.

The measured FRF, $G(j\omega_k)$, consists of three parts [18, 19]:

$$G(j\omega_k) = G_{BLA}(j\omega_k) + G_S(j\omega_k) + N_G(k) \tag{5.9}$$

(i). $G_{BLA}(j\omega_k)$: Best linear approximation of the nonlinear system. In [20], it is stated that a linear representation of nonlinear system with $G_{BLA}(j\omega_k)$ plus a nonlinear noise source $Y(s)$, is robust for a wide class of excitation signals.

(ii). $G_S(j\omega_k)$: Stochastic nonlinear contribution. Even in the absence of disturbing noise, the FRF measurement is scattered around its expected value, and these deviations do not converge to zero. $G_S(j\omega_k)$ is called stochastic nonlinear contribution because it behaves as uncorrelated noise. But, note that once the excitation signal is fixed, it is not a random signal anymore ($G_S(j\omega_k)$ depends

on the random phases of the input). This means that $G_S(j\omega_k)$ is uncorrelated with - but not independent of - the input $U(k)$. $G_S(j\omega_k)$ is represented by the nonlinear noise source, $y_s(t)$ in Fig. 5.9.

(iii). $N_G(k)$: Errors due to output noise source. The output measurement noise, $m_y(t)$ is given in Fig. 5.9. For simplicity, we assumed that input measurements are noise free (output noise dominates).

The best linear approximation $G_{BLA}(j\omega_k)$ consists of two parts [18],

$$G_{BLA}(j\omega_k) = G_0(j\omega_k) + G_B(j\omega_k) \tag{5.10}$$

(i). $G_0(j\omega_k)$: The transfer function of true underlying linear system.

(ii). $G_B(j\omega_k)$: The bias or systematic, deterministic nonlinear contributions independent of the phases of the input signal.

Remarks:

- The nonlinear distortion contributions to the FRF can be subdivided into two parts. First one, $G_B(j\omega_k)$, consists of contributions that do not depend on the the random phases of the excitation. The second one, $G_S(j\omega_k)$, contains the contributions that depend on the random phases [3]. At the output level, (5.9) and (5.10) becomes

$$\begin{aligned} Y(k) &= G_{BLA}(j\omega_k) \cdot U(k) + Y_S(k) + N_Y(k) \\ &= (G_0(j\omega_k) + G_B(j\omega_k)) \cdot U(k) + Y_S(k) + N_Y(k) \end{aligned} \tag{5.11}$$

  In Eqn. (5.11), input-output DFT spectra is related to the best linear approximation (BLA) $G_{BLA}(j\omega_k)$.

- The stochastic behavior of $G_S(j\omega_k)$ is very similar to those of noise $N_G(k)$. Therefore it is difficult to distinguish between noise and nonlinear distortions.

- In a particular experiment using random phase multisine excitation signal with signal period T_0, the measurement time can be increased, $T \to \infty$. This increase in T allows the number of averages, $M = T/T_0$ grow. But this growth in M

does not help to the reduction of nonlinear distortions. Because $G_B(j\omega_k)$ and $G_S(j\omega_k)$ are $O(M^0)$. This means that nonlinear contributions do not disappear as number of averages increase $M \rightarrow \infty$. On the other hand, output noise source $N_G(k)$ is $O(M^{-1/2})$ which means that the noise is reduced as $1/\sqrt{M}$, asymptotically with averages (see Eqn. 4.8 on page 41).

- $G_{BLA}(j\omega_k)$ does change when the amplitude spectrum of the input signal does change [3, 16]. But $G_{BLA}(j\omega_k)$ does not change when the phase spectrum of the input signal changes (as long as the power spectrum of the input signal is same). This is because, systematic nonlinear contribution part of the best linear approximation, $G_B(j\omega_k)$, is independent of the phases of the input signal while dependent of the amplitude spectrum of the input signal.

5.5 A Robust Method Using Random Phase Multisines

In [3, 21], it is shown that, a robust method which depends on random phase multisine excitations can detect and quantify stochastic nonlinear distortions and disturbing noise. This method relies on the assumption that nonlinear dynamic system operates in open loop and the input signal is known exactly ($m_u(t) = 0$ in Fig. 5.9). The robust method starts with generating a random phase multisine excitation signal with period T_0 (see Eqn. 5.7). This signal is applied to the device under investigation for $T_w + P \times T_0$ seconds. T_w is the waiting time so that system reaches steady state response such that transients are below the disturbing noise level. P is the number of consecutive periods of the steady state response measured. This experiment is repeated for M times, each time generating a different random phase multisine signal $U_0^{[m]}(k)$. In the end, a total of $M \times P$ FRF measurements $\hat{G}^{[m,p]}(j\omega_k)$ are calculated for each frequency $k = 1, 2, \ldots, F$, for each consecutive period $p = 1, 2, \ldots, P$, and for each experiment $m = 1, 2, \ldots, M$ (see Fig. 5.10).

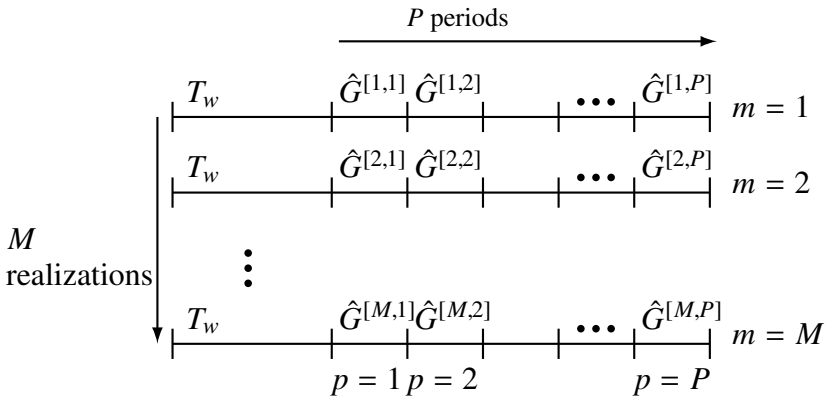

Figure 5.10: *Robust method measurement overview*: Realizing M different (independent) random phase multisine experiments and each time measuring P periods after a waiting time T_w to reduce transient effects.

In each experiment, by averaging the FRFs over the consecutive periods, one can obtain the output noise level (the stochastic nonlinear distortions have the same periodicity as the multisine excitations, so they do not influence the variance over consecutive periods). Averaging of these FRF means over the multiple experiments quantifies the sum of the output noise level and the level of the stochastic nonlinear distortions which depends on the random phases of the multisine excitations. Finally, the difference between the total distortion level (averaging over the experiments) and the noise level (averaging over the consecutive periods) gives the stochastic nonlinear distortions [3]. From Eqn. (5.9), the content of FRF for each period can be illustrated by Eqn. (5.12).

$$\begin{aligned}\hat{G}^{[m,p]}(j\omega_k) &= \frac{Y^{[m,p]}(k)}{U_0^{[m]}(k)} \\ &= G_{BLA}(j\omega_k) + \frac{Y_S^{[m]}(j\omega_k)}{U_0^{[m]}(k)} + \frac{N_Y^{[m,p]}(k)}{U_0^{[m]}(k)} \\ &= G_{BLA}(j\omega_k) + G_S^{[m]}(j\omega_k) + N_G^{[m,p]}(k)\end{aligned} \tag{5.12}$$

Here, please pay attention that, $G_S^{[m]}(j\omega_k)$ does not depend on the period index p. For each independent experiment, the sample mean and sample variance over P

consecutive periods are given in (5.13):

$$\begin{aligned}\hat{G}^{[m]}(j\omega_k) &= \frac{1}{P}\sum_{p=1}^{P}\hat{G}^{[m,p]}(j\omega_k)\\ \hat{\sigma}_n^{2[m]}(k) &= \frac{1}{P(P-1)}\sum_{p=1}^{P}|\hat{G}^{[m,p]}(j\omega_k)-\hat{G}^{[m]}(j\omega_k)|^2\end{aligned} \tag{5.13}$$

Here $\hat{\sigma}_n^{2[m]}(k)$, is the sample noise variance of the sample mean $\hat{G}^{[m]}(j\omega_k)$, which explains the extra factor P. Calculating the mean and variance over M experiments gives the following:

$$\begin{aligned}\hat{G}_{BLA}(j\omega_k) &= \frac{1}{M}\sum_{m=1}^{M}\hat{G}^{[m]}(j\omega_k)\\ \hat{\sigma}^2_{BLA}(k) &= \frac{1}{M(M-1)}\sum_{m=1}^{M}|\hat{G}^{[m]}(j\omega_k)-\hat{G}_{BLA}(j\omega_k)|^2\\ \hat{\sigma}^2_{BLA,n}(k) &= \frac{1}{M^2}\sum_{m=1}^{M}\hat{\sigma}_n^{2[m]}(k)\end{aligned} \tag{5.14}$$

Here, $\hat{\sigma}^2_{BLA}(k)$ represents the total variance and $\hat{\sigma}^2_{BLA,n}(k)$ represents the output noise variance of $\hat{G}_{BLA}(j\omega_k)$ estimate which explains the extra factor M. If the noise variance of each signal period is represented by $\sigma_n^2 = var(N_G^{[m,p]})$ and the nonlinear distortion due to random phases of excitation signal of one experiment is represented by $\sigma_S^2 = var(G_S^{[m]})$, the following equation appears:

$$\begin{aligned}\mathbb{E}\{\hat{\sigma}^2_{BLA}(k)\} &= \frac{\sigma_n^2}{MP}+\frac{\sigma_S^2}{M}\\ \mathbb{E}\{\hat{\sigma}^2_{BLA,n}(k)\} &= \frac{\sigma_n^2}{MP}\end{aligned} \tag{5.15}$$

Equation (5.15) gives a great insight about determining the optimal number of consecutive periods P and number of experiments M according to the experimenter's needs. For a given amount of time $T = M \times P \times T_0$, if the objective is to minimize the total variance of the best linear approximation $\hat{G}_{BLA}(j\omega_k)$, while keeping the ability to distinguish noise from the nonlinear distortions, then one can choose $P = 2$ and $M = T/(P \times T_0)$. If the aim is to maximize nonlinearity detection ability, then output noise should be reduced as much as possible by choosing $M = 2$ and $P = T/(M \times T_0)$. In the experiments realized in this study (see Sections 5.3 and 5.6 for more details), $M = 6$, $P = 40$, $T_w = 6$ and $T_0 = 2$ seconds are chosen.

Finally, the variance of stochastic nonlinear distortions $G_S^{[m]}(k)$ of one multisine experiment σ_S^2 can be derived as follows:

$$\sigma_S^2 = \begin{cases} M(\hat{\sigma}_{BLA}^2(k) - \hat{\sigma}_{BLA,n}^2(k)) & \hat{\sigma}_{BLA}^2(k) > \hat{\sigma}_{BLA,n}^2(k) \\ 0 & \hat{\sigma}_{BLA}^2(k) \leq \hat{\sigma}_{BLA,n}^2(k) \end{cases} \tag{5.16}$$

5.6 Experimental Illustration of the Robust Method

For the experiment of interest, six "Random Phase Multisine" signals are generated. All six random phase multisine signals possess the same magnitude spectrum but with different phase spectra. In Section 5.3, signal properties and experimental settings are explained in detail and two of the six time domain measurements are given. The Robust Method explained in Section 5.5 is applied and the stochastic nonlinearity distortion is quantified as well as the noise level and the best linear approximation of nonlinear system. In Fig. 5.11 the results are given. Figure 5.11 provides a lot of qualitative knowledge about the complexity of the problem, as well as quantitative information about the plant and the measurement quality.

In Fig. 5.11, the blue line corresponds to best linear approximation (BLA) magnitude $|\hat{G}_{BLA}(j\omega_k)|$. The red line gives the output noise level $\hat{\sigma}_{BLA,n}^2(k)$ while the green line shows the total variance (noise + stochastic nonlinear distortion) $\hat{\sigma}_{BLA}^2(k)$. The difference between the green line and the red line gives the magnitude of stochastic nonlinear distortions $G_S(j\omega_k)$ of the best linear approximation measurement $\hat{G}_{BLA}(j\omega_k)$. It is observed that in low frequencies stochastic nonlinear distortions are the dominant error source. As frequency increases, stochastic nonlinear distortions decrease very rapidly. This indicates the strong presence of friction; since friction is expected to be more effective in low frequencies. After 200Hz, stochastic nonlinear distortion drops below the level of the output noise. This means that above 200Hz, dominant error source in $\hat{G}_{BLA}(j\omega_k)$ measurement is the output noise. It is noted from the blue line that there exists a mechanical resonance at around 179 Hz in which the system responds at greater amplitude than it does at other frequencies. At this mechanical resonance frequency 179Hz, it is also observed that stochastic nonlinear distortions create a peak (see the green line). Another interesting point obtained from the experiment is that, at 30Hz, the output noise causes a small peak (see the red line). This is because of the

fact that there is a small cooling fan at the backward of mechanical system, turning at around 30Hz, disturbing the measurements.

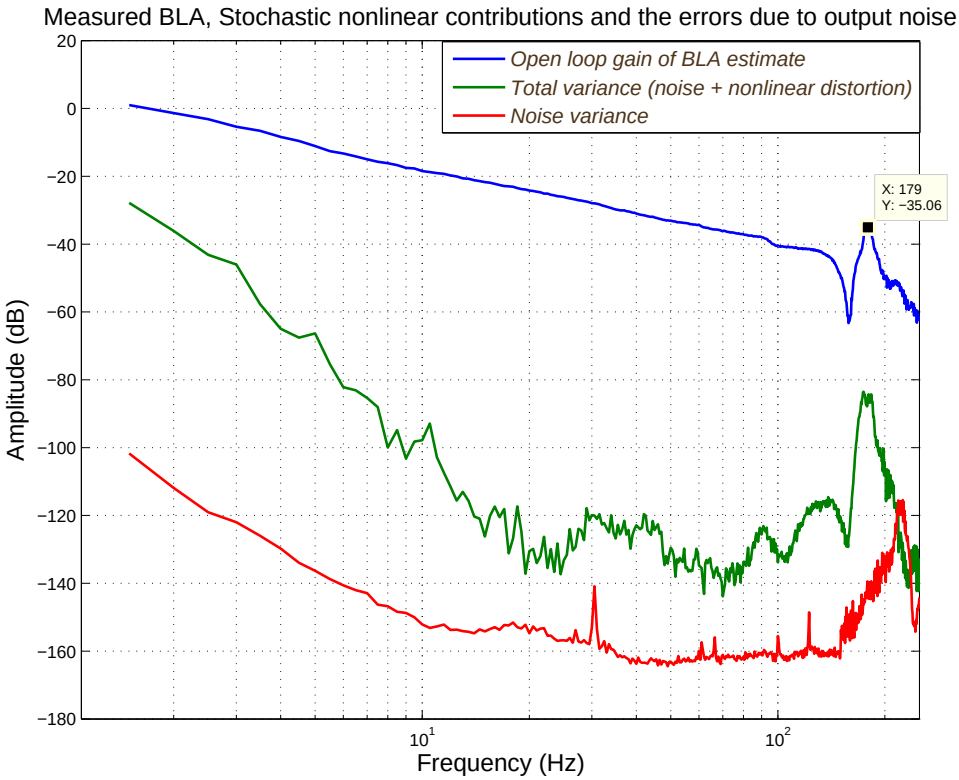

Figure 5.11: Nonlinearity quantification with "Robust Method". Blue line: Best linear approximation (BLA) magnitude $|\hat{G}_{BLA}(j\omega_k)|$. Red line: Noise level $\hat{\sigma}^2_{BLA,n}(k)$. Green line: Total variance (noise + stochastic nonlinear distortion) $\hat{\sigma}^2_{BLA}(k)$.

In Fig. 5.11, there is a contradictory situation between the frequencies 217Hz and 236Hz. The output noise (the red line) σ_n^2 is slightly bigger than the total noise (green line) $\sigma_n^2 + \sigma_S^2$ and hence, the contradictory outcome occurs, $\sigma_S^2 < 0$ (as if stochastic nonlinear distortions are negative). In paper [21], this contradictory situation of $\sigma_S^2 < 0$ is explained. It is claimed that this phenomenon occurs due to the presence of nonstationary distortions σ_t^2 which are not modeled in Section 5.4.

CHAPTER 6

LINEAR TIME-INVARIANT PLANT MODELS

6.1 Introduction

In this study, the primary aim is to obtain a parametric plant model, $G(\Omega, \theta)$ from the noisy nonparametric FRF measurements. The estimation of nonparametric frequency response function is shown in Chapter 4 and the estimation of parametric plant model is shown in Chapter 7. Nonparametric FRF measurements store a vector of frequency points with the corresponding complex frequency responses. The nonparametric model is sufficient for most of the frequency domain analyses and controller designs. However it is not possible to perform time domain simulations with them. On the other hand, parametric LTI plant models are more convenient for frequency domain analyses, controller design and it is possible to perform time domain simulations. Parametric LTI plant model is a basic representation of a system using a finite number of parameters, $\theta = [\theta_1,\ \theta_2,\ \ldots \theta_{n_\theta},\ ]^T$. There are several types of numeric LTI models such as transfer function model and state space model. In this study, the transfer function type of parametric models is preferred.

This chapter explains the parametric plant model used in this study. The parametric model discussed in this chapter is valid only for the systems under periodic excitations. Relation of input and output spectra for periodic signals is given in Section 6.2. The parametric plant model definition with and without time delay, parameter vector and related notations are given in Section 6.3. Lastly, the nonparametric noise model concept is discussed in Section 6.4. The reason of preferring the nonparametric noise model over the parametric noise model is stated.

6.2 Relation of Input and Output Spectra for Periodic Signals

In order to prevent spectral leakage errors, periodic signals are preferred to excite the system and measure input-output pairs are measured at an integer number of signal periods (see Section 3.3 on page 18). As an illustration, assume that a periodic excitation signal $u(t)$ with a signal period $T_0 = 1/f_0$ is given. Signal period is an integer number of the sampling time of the system $T_0 = N \cdot T_s$, $N \in \mathbb{N}$. Let the total measurement time be $T_{total} = T + T_w$ where T is the transient free measurement duration and T_w is the waiting time to reach steady state. Transient free measurement duration is an integer number of signal periods $T = M \cdot T_0$ where $M \in \mathbb{N}$ is also the number of averages (see Section 4.3 on page 39). Independent of whether the excitation is continuous or discrete, the ratio of the output to the input DFT spectra at the excited frequency lines $k = hf_0$, $h \in \mathbb{N}$ gives the true transfer function:

$$Y(k) = G(\Omega_k, \theta)U(k) \tag{6.1}$$

In (6.1), θ is the parameter vector and the transform variable $\Omega = s$ for lumped continuous-time systems, $\Omega = z^{-1}$ for discrete time systems.

Note that, FRF measurements are realized in steady-state (T_w seconds are waited allowing the transient effects to die). Therefore, there is no need to consider the initializations of data record (i.e., the transient effects) in the transfer function model.

6.3 Parametric Plant Model

In this study, the preferred parametric model that is valid for periodic excitations in steady state, is a rational form of a transfer function as given in (6.2):

$$G(\Omega, \theta) = \frac{B(\Omega, \theta)}{A(\Omega, \theta)} = \frac{\sum_{r=0}^{n_b} b_r \Omega^r}{\sum_{r=0}^{n_a} a_r \Omega^r} \tag{6.2}$$

Here, transform variable is $\Omega = s$ for lumped continuous-time systems and $\Omega = z^{-1}$ for discrete time systems. $\theta \in \mathbb{R}^{n_\theta}$ the vector of the plant model parameters with the

size of n_θ.

$$\theta = [a_0,\ a_1,\ \ldots,\ a_{n_a},\ b_0,\ b_1,\ \ldots,\ b_{n_b}]^T \tag{6.3}$$

In every real life application, there exists a time delay (negligible or not). Therefore, it makes sense to add a time delay parameter to the transfer function model (6.2). For continuous-time models ($\Omega = s$), (6.2) becomes

$$G(s,\theta) = e^{-\tau s}\frac{B(s,\theta)}{A(s,\theta)} = e^{-\tau s}\frac{\sum_{r=0}^{n_b} b_r s^r}{\sum_{r=0}^{n_a} a_r s^r} \tag{6.4}$$

For discrete-time models, (6.2) becomes

$$G(z^{-1},\theta) = z^{-\tau/T_s}\frac{B(z^{-1},\theta)}{A(z^{-1},\theta)} = z^{-\tau/T_s}\frac{\sum_{r=0}^{n_b} b_r z^{-r}}{\sum_{r=0}^{n_a} a_r z^{-r}} \tag{6.5}$$

Time delay, $\tau \in \mathbb{R}$ is an arbitrary, nonnegative number. Time delay does not have to be an integer multiple of the sampling period T_s. Then, the vector of the model parameters θ also contains the delay parameter τ.

$$\theta = [a_0,\ a_1,\ \ldots,\ a_{n_a},\ b_0,\ b_1,\ \ldots,\ b_{n_b},\ \tau]^T \tag{6.6}$$

6.4 Nonparametric Noise Model

In (6.7), true (unknown) DFT spectra $U_0(k)$ and $Y_0(k)$, the noise components $N_U(k)$ and $N_Y(k)$, and the measured input-output DFT spectra $U(k)$ and $Y(k)$ relations are given. $N_U(k) = DFT(n_u(t))$ and $N_Y(k) = DFT(n_y(t))$ are functions of the measurement noise, the process noise, and in some cases, the generator noise.

$$\begin{aligned} Y(k) &= Y_0(k) + N_Y(k) \\ U(k) &= U_0(k) + N_U(k) \end{aligned} \tag{6.7}$$

In control applications, input noise is usually zero, since input signal can be stored in the digital memory of a computer (there is no input measurement error). In Fig. 6.1, the DFT relations for the exactly known input case, $N_U(k) = 0$, is displayed in block diagram.

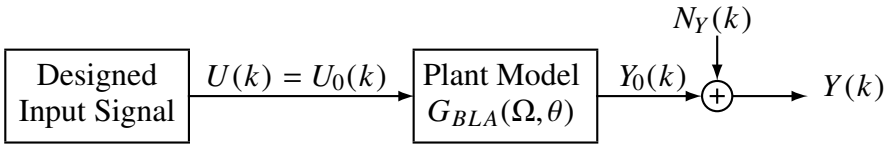

Figure 6.1: DFT relation between input and output spectra with $N_U(k) = 0$

In this study, the aim is to find a parametric plant model using the nonparametric noisy FRF measurements. Estimation of parametric plant model is deeply analyzed in Chapter 7. The noise model provides a good insight about the reliability of FRF measurements and set the uncertainty bounds on a linear model. In addition (possibly more important), in Section 7.9 on page 98, it turns out that the noise model is a highly beneficial item when used as a weighting coefficient in the cost function of the parametric plant model estimation. Using the noise model, an estimator will know how much to trust each FRF measurement at each frequency. Therefore, outcome will be less affected by noisier (large σ_i) measurements.

Disturbing errors $N_U(k)$ and $N_Y(k)$ can be modeled as either nonparametric or parametric noise models. Estimation method of nonparametric noise model is given in Subsection 4.3.2 on page 41. Nonparametric noise model is a vector of uncertainty of the FRF measurements at numerous frequency points (See Eqn. 6.8). As an example for nonparametric noise model, Fig. 4.26 on page 58 can be examined.

$$\sigma_U^2(k) = var(N_U(k)), \quad \sigma_Y^2(k) = var(N_Y(k)), \quad \sigma_{YU}^2(k) = covar(N_Y(k), N_U(k)) \tag{6.8}$$

The choice between nonparametric and parametric noise models becomes an important decision for the estimation of parametric plant model. Parametric noise models are usually combined with one of the model structures such as ARX, ARMAX, ARMA,

OE (Output error), BJ (Box-Jenkins). However, according to [22], parametric noise model has some certain drawbacks. It requires a second model selection for parametric noise model and additional noise model parameters increases the complexity of the problem. [22] states that in practice, parametric noise models are more suitable for time domain identification while nonparametric noise models are preferable for weighting the cost function in the frequency domain identification. In conclusion, [22] strongly advises the nonparametric noise model since it simplifies the estimation of parametric plant models and the quality of the noise model is independent of the parametric plant model. Furthermore, nonparametric noise models are easily obtained in the earlier process of FRF measurements (see Subsection 4.3.2 on page 41). Therefore, this study completely deals with nonparametric noise models.

CHAPTER 7

A CASE STUDY: APPLICATION OF IDENTIFICATION TECHNIQUES

7.1 Introduction

In Chapter 4, the nonparametric FRF measurement and the nonparametric noise model of the system at numerous frequency points are measured and preprocessed. Next, the frequency domain identification problem of finding a parametric model which best represents a dynamic system will be studied. Parametric models are useful for time domain simulation, controller design, stability analysis and prediction purposes. The parametric model and the model parameter vector which will be used in this study are explained in Chapter 6. The parameters of the transfer function (parametric model) can be searched with various estimation techniques. However, before that, the order of transfer function should be decided. In the first trial, the order of transfer function can be chosen small. After an optimization procedure, the estimated plant model and the measured FRF are compared by a visual inspection on a Bode plot or by residual analysis. This comparison step is called "Validation". If the estimated transfer function satisfactorily describes the dynamic system, identification problem is solved. Otherwise, the order of the transfer function (parametric plant model) is gradually increased until a satisfactory parametric model is obtained. Therefore, the system identification can be portrayed as an iterative process. Eventually, an engineer looks for a parametric plant model which best describes the system with minimum complexity (minimum order). In [23], a two-step order selection method is proposed for the numerator and denominator of SISO LTI parametric plant models.

In this system identification problem, the aim is, minimizing a cost function which best fits the parametric model into a nonparametric FRF measurement. Cost function varies from estimator to estimator. However, all cost functions uses a common error function. This error function is explained in Section 7.2. Minimization of the cost function requires a numerical search procedure. The parametric plant model (6.4) on page 79 is highly nonlinear in the parameters θ as it appears both in the numerator and the denominator. This causes lots of undesirable local minimum solutions. Arbitrarily choosing the initial point in the optimization procedure causes the problem of obtaining local minimums. In order to avoid local minimums, sufficiently good starting values of model parameter vector, θ is needed. For the initial system delay estimate, a method is offered in Section 7.3. For the initial model parameters, there is a requirement for self-starting algorithms that generate the starting values from the measured data without user interaction. Global optimization algorithms which do not require starting value can be used for this purpose. The algorithms explained in Sections 7.4 "Linear Least Squares", 7.5 "Iterative Weighted Linear Least Squares" are implemented to calculate the global minimum directly and the algorithm explained in Section 7.6 "Genetic Algorithm" is implemented to find the global minimum stochastically. After generating good starting values with one of the global minimizers, one of the efficient local minimum algorithms explained in Sections 7.7 "Nonlinear Least Squares", 7.8 "Nonlinear Logarithmic Least Squares", 7.9 "Maximum Likelihood" can be used to estimate better parametric plant models. All the identification techniques are implemented for the FRF measurements obtained from the inner azimuth gimbal of an Electro-Optic system. In each identification method, the estimated plant model and the measured FRF are compared by a visual inspection on a Bode plot and by residual analysis. In the end, the performances of all the identification techniques are compared in detail in Section 7.10. It turns out that Maximum Likelihood estimator which uses the additional information, the nonparametric noise model, provides statistically better results. This chapter ends with an explanation of model order selection and validation in Section 7.11.

7.2 Building an Error Function for the System Identification Problem

In this study, the frequency domain identification of the inner azimuth plant model of IR/EO gimbal system with known nonparametric noise model is handled. The identification starts from measured input-output DFT spectra $U(k)$ and $Y(k)$.

$$\begin{aligned} U(k) &= U_0(k) + N_U(k) \\ Y(k) &= Y_0(k) + N_Y(k) \end{aligned} \tag{7.1}$$

In (7.1), $U_0(k)$, $Y_0(k)$ are true unknown values. Alternatively, the identification can start from a measured frequency response function $G(\Omega_k)$.

$$G(\Omega_k) = G_0(\Omega_k) + N_G(k) \tag{7.2}$$

In (7.2), $G_0(\Omega_k)$ is the true unknown FRF. Note that (7.2) is a special case of (7.1) with $Y(k) = G(\Omega_k)$ and $U(k) = 1$. The noise on input and output measurements (See Fig. 7.1) are estimated from the nonparametric noise model using (4.11) on page 42.

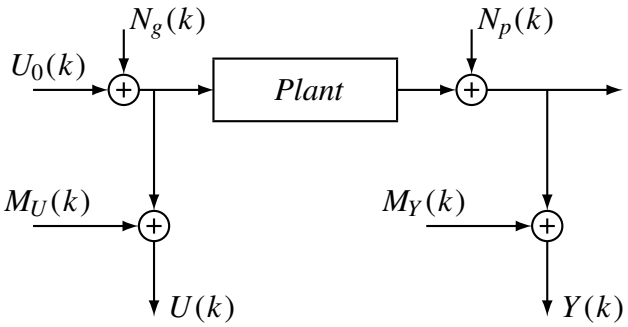

Figure 7.1: Frequency domain experiment measurement process. $N_g(k)$ is generator noise, $M_U(k)$ and $M_Y(k)$ are the input and output measurement errors and $N_p(k)$ is the process noise

In the frequency domain estimation, it is not feasible to use all frequency measurement band, because there may be too much noise at high frequencies and disturbance in low frequencies. In addition to minimizing noise, it is usually better to focus on specific frequency band of interest. For this experiment, plant is supposed to be modeled for controller design applications. In order to enhance frequencies around the desired closed-loop bandwidth, the plant model measurement in Subsection 4.4.2 on page 45

is band-pass filtered between 1 Hz and 120 Hz. In other words, the 1-120 Hz frequency band is taken into account in the optimization problem.

Next, the measurement is approximated by one of the parametric models $G(\Omega_k, \theta)$ given in equations (6.2), (6.4), (6.5) on page 78. The parameter vector θ contains the free parameters of numerator and denominator coefficients of the rational form $G(\Omega_k, \theta) = \dfrac{B(\Omega_k, \theta)}{A(\Omega_k, \theta)}$, except $a_0 = 1$ consraint.

In estimation algorithms for periodic signals ($\Omega = z^{-1}, s$), *output error* $e_{output}(\Omega_k, \theta, Z(k))$ can be used, which is the difference between the observed output $Y(k)$ and the modeled output $Y(\Omega_k, \theta)$, [3].

$$Y(\Omega_k, \theta) = G(\Omega_k, \theta)U(k) \tag{7.3}$$

$$e_{output}(\Omega_k, \theta, Z(k)) = Y(\Omega_k, \theta) - Y(k) \tag{7.4}$$

In estimation algorithms for periodic signals ($\Omega = z^{-1}, s$), another term that can be used is the *equation error* $e(\Omega_k, \theta, Z(k))$ which is the difference between the left and right hand sides of the transfer function model (6.1) on page 78, after multiplication by $A(\Omega_k, \theta)$. Z contains the measured input-output (DFT) spectra where $k = 1, 2, \ldots, F$.

$$Z(k) = \begin{bmatrix} Y(k) & U(k) \end{bmatrix} \tag{7.5}$$

Data vector, Z is related to the true values by $Z = Z_0 + N_Z$, where the disturbing noise N_Z has zero mean and is independent of Z_0, [3].

$$e(\Omega_k, \theta, Z(k)) = A(\Omega_k, \theta)Y(k) - B(\Omega_k, \theta)U(k) \tag{7.6}$$

The quality of the match between measurements and the model is measured by the cost function. There is no unique choice for the cost function. Most algorithms implemented in this experiment, minimize (in each step) a "quadratic-like" cost function $V(\theta, Z)$.

$$V(\theta, Z) = \epsilon^H(\theta, Z)\epsilon(\theta, Z) = \sum_{k=1}^{F} |\epsilon(\Omega_k, \theta, Z(k))|^2 \tag{7.7}$$

$\epsilon(\theta, Z) \in \mathbb{C}^F$ is some kind of measure of the difference between the measurements

and the model. The residual $\epsilon(\theta, Z)$ is either linear or nonlinear vector function of the model parameters θ and the measurements Z.

7.3 Initial Time Delay Estimate

The delay in measurement setup apart from the system being identified should be treated with care, or, at least, to be corrected later. In every real life application, there exist an unknown time delay negligible or not. When it is necessary to deal with unknown delays, delay parameter can be added to parametric plant model (see equations 6.4, 6.5 on page 79). However, this can be very risky since optimization problem becomes very sensitive to delay parameter. Nonlinear Least Squares, Nonlinear Logarithmic Least Squares, Maximum Likelihood cost functions are not global optimization algorithms, therefore a good starting value of the time delay is mandatory in order to avoid converging to a local minimum. In [3], a time delay estimation method as a starting value is suggested (see (7.8)). This method estimates time delay via the mean slope of the unwrapped phase of the measured frequency response function where $[w_{k_1}, w_{k_2}]$ defines the passband of the system.

$$\hat{\tau} = -\frac{1}{k_2 - k_1} \sum_{k=k_1}^{k_2-1} \frac{\angle G(\Omega_{k+1}) - \angle G(\Omega_k)}{w_{k+1} - w_k} \tag{7.8}$$

7.4 Linear Least Squares

"Linear Least Squares" estimator suggested in [3, 24], does not require prior noise knowledge and performs a global minimum procedure. Linear least squares algorithm does not need a priori starting parameter set; it directly calculates the global minimum. The linear least squares (LS) cost function is given below:

$$V_{LS}(\theta, Z) = \sum_{k=1}^{F} |e(\Omega_k, \theta, Z(k))|^2 \tag{7.9}$$

$e(\Omega_k, \theta, Z(k))$ stands for the "equation error" given in (7.6). The linear least squares (LS) estimate $\hat{\theta}_{LS}(Z)$ is found by minimizing (7.9) w.r.t. θ using the constraint $a_{n_a} = 1$.

The measured FRF $G(\Omega_k)$ of the system transfer function at a set of well-chosen frequencies from the multisine experiment in Subsection 4.4.2 on page 45 is used. The continuous time plant model with time delay given in (6.4) on page 79, is identified starting from transfer function measurements (Eqn. 7.9 with equation error (7.6), $\Omega = s$, $Y(k) = G(s_k)$, $U(k) = 1$). The parametric model that is used in the cost function is a rational transfer function with delay. Increasing the complexity of the model may result in closely following noise and unnecessarily complicated transfer function. Lowering the complexity of the model on the other hand may result in poor fit and big errors. For the experiment of interest, the number of poles chosen as $n_a = 3$ and number of zeros chosen as $n_b = 2$.The initial system delay estimate is calculated from mean slope of unwrapped phase in passband from (7.8) to be $\hat{\tau} = 0.0064$ seconds.

The quadratic cost function in the measurements is given below:

$$V_{LS}(\theta, Z) = \epsilon^H(\theta, Z)\epsilon(\theta, Z) = \sum_{k=1}^{F} |\epsilon(\Omega_k, \theta, Z(k))|^2 = \sum_{k=1}^{F} |e(\Omega_k, \theta, Z(k))|^2 \quad (7.10)$$

where $\epsilon(\theta, Z) \in \mathbb{C}^F$ is a kind of measure of the difference between the measurements and the model. The cost function $V_{LS}(\theta, Z)$ is *quadratic-in-the-measurements* Z. The residual $\epsilon(\theta, Z)$ is linear in Z (the measurements). Equation (7.10) is rewritten as $V_{LS}(\theta, Z) = \epsilon_{re}^H(\theta, Z)\epsilon_{re}(\theta, Z)$ where $()_{re}$ stacks the real and imaginary parts on top of each other.

$$\epsilon_{re}(\theta, Z) = \begin{bmatrix} Re(\epsilon_{re}(\theta, Z)) \\ Im(\epsilon_{re}(\theta, Z)) \end{bmatrix} \quad (7.11)$$

"Quadratic programming" setup has been designed for the problem of finding a vector θ (parameter set given in Eqn. 6.3 on page 79) that minimizes a quadratic function $V_{LS}(\theta, Z)$,

$$V_{LS}(\theta, Z) = \epsilon_{re}^H(\theta, Z)\epsilon_{re}(\theta, Z) = \frac{1}{2}\theta^T \cdot H \cdot \theta \quad (7.12)$$

subject to linear constraint $A_{eq} \cdot \theta = b_{eq}$. The number of variables in the parameter set θ is $size(\theta) = 7$ with $\theta(4) = a_{n_a} = a_3 = 1$ constraint for the experiment of interest. The 7x7 sized H matrix has been found for the experiment of interest analytically using the symbolic math toolbox of MATLAB. Since H is a positive definite matrix, this problem is convex; so every local minimum is a global minimum. It is checked

whether H is positive definite by noting all its eigenvalues are positive.

The linear least squares estimate for the experiment of interest results in the following transfer function:

$$\hat{G}(s_k,\theta) = e^{-0.00641s}\frac{5.719s^2 - 3326s + 1.43\text{e}06}{s^3 + 486.3s^2 + 1.898\text{e}05s + 8.547\text{e}05} \tag{7.13}$$

The Bode plot of measured transfer function and estimated transfer function is given in Fig. 7.2

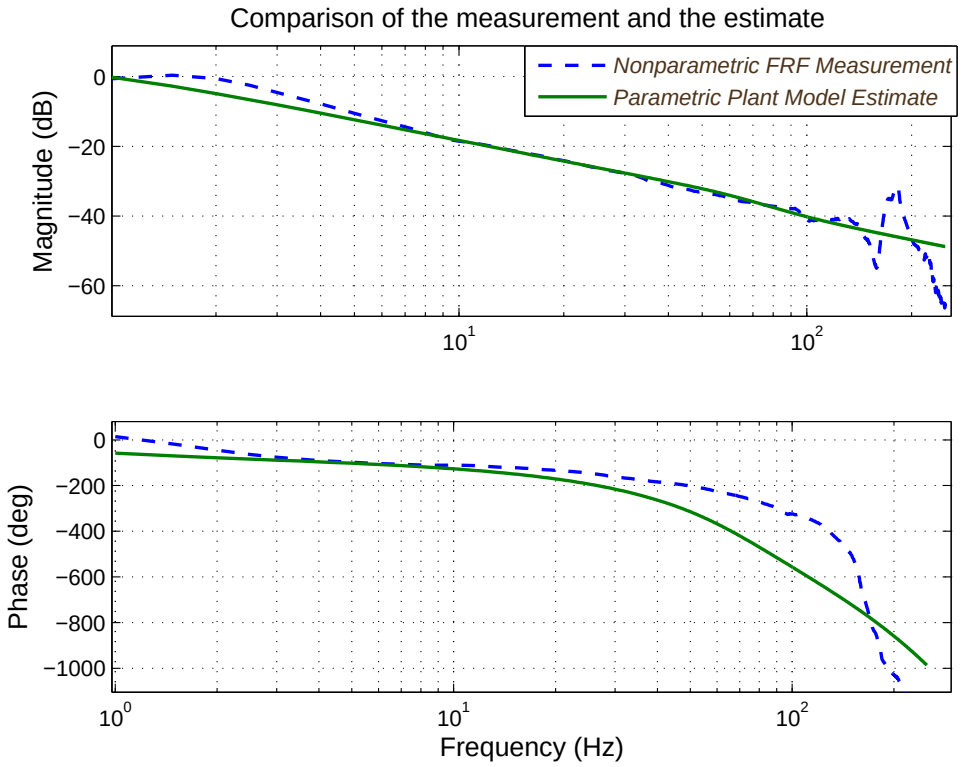

Figure 7.2: Comparison of Linear Least Squares estimation and the measurement

The magnitude of complex residual analysis $|Y(k)/U(k) - G(\Omega_k,\hat{\theta}_{LS})|$ for the measured transfer function and the estimated transfer function is given in Fig. 7.3

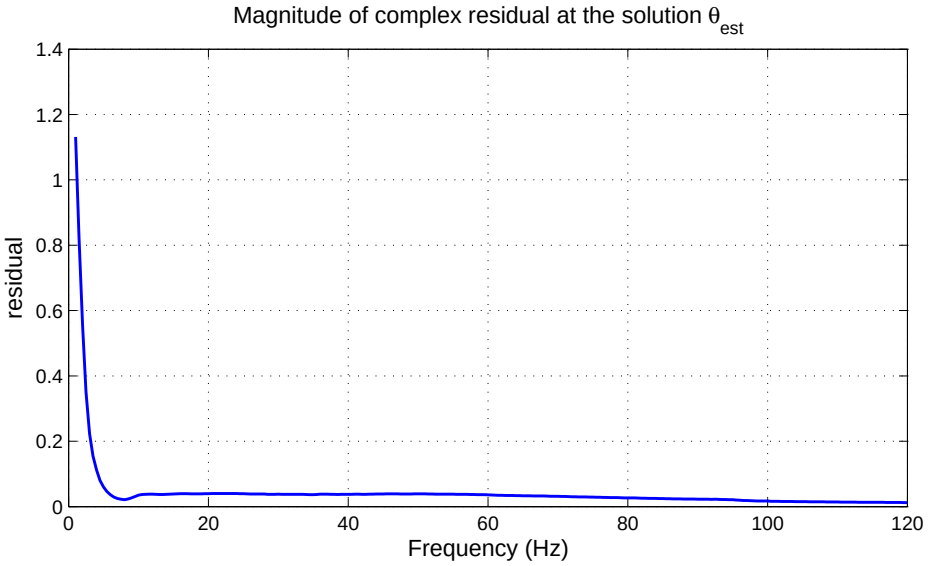

Figure 7.3: The magnitude of complex residual $|Y(k)/U(k) - G(\Omega_k, \hat{\theta}_{LS})|$ analysis of Linear Least Squares Estimation

The linear least squares approach has considerable weakness when identifying continuous time models ($\Omega = s$): the overemphasizing of high-frequency errors in (7.9), [24]. Equation error, $e(\Omega_k, \theta, Z(k))$ is a polynomial in Ω_k and, hence, the contribution of the disturbing noise at a frequency Ω_k to the cost function increases with $|\Omega_k|^{2max(n_a,n_b)}$. This drawback of linear least squares estimation causes poor low frequency fits (see Fig. 7.2).

7.5 Iterative Weighted Linear Least Squares

"Iterative Weighted Linear Least Squares" estimator suggested in [3, 24], does not require prior noise knowledge and performs a global minimum procedure. The "Linear Least Squares" approach explained in Section 7.4, lacks the sensitivity to low-frequency errors. To overcome this drawback, the equation error $e(\Omega_k, \theta, Z(k))$ in (7.9) is divided by an initial guess of the denominator polynomial $A(\Omega_k, \theta^{(0)})$. The obtained weighted linear least squares estimate $\theta^{(1)}$ is used to calculate a better estimate of the denominator polynomial $A(\Omega_k, \theta^{(1)})$, resulting in a better estimate $\theta^{(2)}$, and so on .... The ith step of the iterative procedure consists of minimizing

$$V_{IWLS}^{(i)}(\theta^{(i)}, Z) = \sum_{k=1}^{F} \frac{|e(\Omega_k, \theta^{(i)}, Z(k))|^2}{|A(\Omega_k, \theta^{(i-1)})|^2} \tag{7.14}$$

with $e(\Omega_k, \theta, Z(k))$ stands for the equation error given in (7.6), w.r.t. $\theta^{(i)}$ using the constraint $a_{n_a} = 1$. To get a starting value, "Linear Least Squares" estimate in Section 7.4 is used $\theta^{(0)} = \hat{\theta}_{LS}(Z)$. When iterations converge ($\theta^{(i)} \cong \theta^{(i-1)}$ for i sufficiently large), iterative weighted linear least squares (IWLS) estimate is found, $\hat{\theta}_{IWLS}(Z) = \theta^{(\infty)}$.

More general form of "Iterative Weighted Linear Least Squares" cost function (7.14) can be written as:

$$V_{IWLS}^{(i)}(\theta^{(i)}, Z) = \sum_{k=1}^{F} W^2(\Omega_k, \theta^{(i-1)}) |e(\Omega_k, \theta^{(i)}, Z(k))|^2 \tag{7.15}$$

where $W(\Omega_k, \theta^{(i-1)})$ is a well-chosen real weighting function. One particular weighting is:

$$W(\Omega_k, \theta^{(i-1)}) = \frac{1}{|A(\Omega_k, \theta^{(i-1)})|^r} \quad \text{with } r \in [0, \infty) \tag{7.16}$$

Two special cases of (7.16) are the "linear least squares" method for $r = 0$ and the "iterative weighted linear least squares" method (7.14) for $r = 1$. Powers of r different from one, may result in smaller output errors $Y(k) - Y(k, \theta)$ (7.4). If the iterative scheme (7.14) does not converge, then relaxation ($r < 1$) is helpful, [3].

The measured FRF $G(\Omega_k)$ of the system transfer function at a set of well-chosen frequencies from the multisine experiment in Subsection 4.4.2 on page 45 is used. The continuous time plant model with the time delay given in (6.4) on page 79, is identified starting from transfer function measurements (Eqn. 7.14 with equation error (7.6), $\Omega = s$, $Y(k) = G(s_k)$, $U(k) = 1$). The parametric model that is used in the cost function is a rational transfer function with delay. Increasing the complexity of the model may result in closely following noise and an unnecessarily complicated transfer function. Lowering the complexity of the model on the other hand may result in poor fit and big errors. For the experiment of interest, the number of poles chosen as $n_a = 3$

and number of zeros chosen as $n_b = 2$. The initial system delay estimate is calculated from mean slope of unwrapped phase in passband from (7.8) to be $\hat{\tau} = 0.0064$ seconds.

For the experiment of interest, The "Iterative Weighted Linear Least Squares" estimate found with 8 iterations, results in the following transfer function:

$$\hat{G}(s_k, \theta) = e^{-0.00641s} \frac{-0.47s^2 + 886.3s + 1685}{s^3 + 95.46s^2 + 919.7s + 7326} \tag{7.17}$$

The Bode plot of measured transfer function and estimated transfer function is given in Fig. 7.4

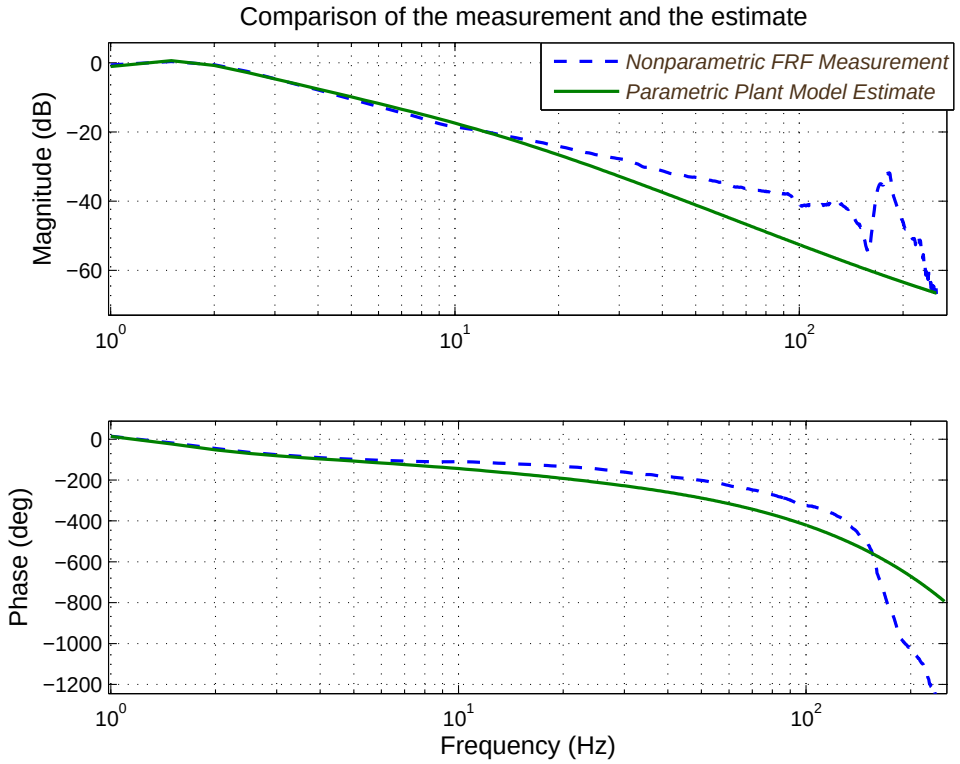

Figure 7.4: Comparison of Iterative Weighted Linear Least Squares estimation and the measurement

The magnitude of complex residual analysis $|Y(k)/U(k) - G(\Omega_k, \hat{\theta}_{IWLS})|$ for the measured transfer function and estimated transfer function is given in Fig. 7.5

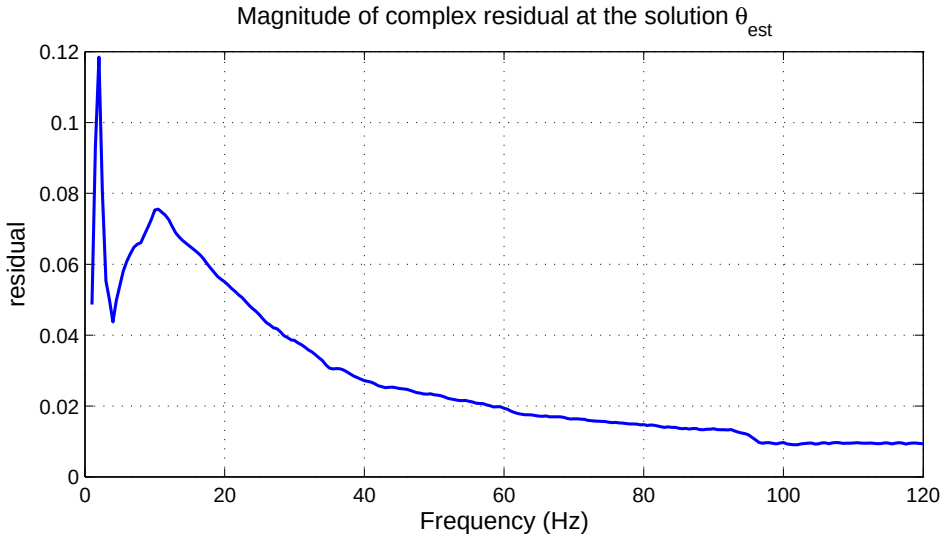

Figure 7.5: The magnitude of complex residual $|Y(k)/U(k) - G(\Omega_k, \hat{\theta}_{IWLS})|$ analysis of Iterative Weighted Linear Least Squares estimation

7.6 Genetic Algorithm

"Genetic algorithm" estimator implemented in this study, does not require prior noise knowledge and performs a global minimum procedure. In reference [25], genetic algorithm optimization technique is thoroughly explained. Genetic algorithm is an optimization method which mimics the process of natural evolution. The cost function used in the genetic algorithm is given in (7.18).

$$V_{GA}(\theta, Z) = \sum_{k=1}^{F} |Y(k)/U(k) - G(\Omega_k, \theta)|^2 \tag{7.18}$$

The measured FRF $G(\Omega_k)$ of the system transfer function at a set of well-chosen frequencies from the multisine experiment in Subsection 4.4.2 on page 45 is used. The continuous time plant model with the time delay given in (6.4) on page 79 is identified starting from transfer function measurements (Eqn. 7.18 with $\Omega = s$, $Y(k) = G(s_k)$, $U(k) = 1$). The parametric model that is used in cost function is a rational transfer function with delay. Increasing the complexity of the model may result in closely following noise and an unnecessarily complicated transfer function. Lowering the complexity of the model on the other hand may result in poor fit and big errors. For the experiment of interest, the number of poles chosen as $n_a = 3$ and number of zeros

chosen as $n_b = 2$. The initial system delay estimate is calculated from mean slope of unwrapped phase in passband from (7.8) to be $\hat{\tau} = 0.0064$ seconds.

The genetic algorithm settings in this experiment are designed as follows. In order to converge a unique solution, the constraint $a_{n_a} = a_3 = 1$ is selected. The size of the parameter vector (the number of variables) is then $n_\theta = n_a + n_b + 1 = 6$. The evolution starts with a population size of 80. Each individual parameter vector, θ, is randomly generated. In each generation (iteration), the fitness of every individual in the population is evaluated according to (7.18) and constraints. The more fit individuals are stochastically chosen from the current population, and each individual's genome is recombined and randomly mutated to form a new generation. The "Genetic Algorithm" estimate found with 100 generations, results in the following transfer function:

$$\hat{G}(s_k, \theta) = e^{-0.00641s} \frac{7.526s^2 - 11.87s + 6.735}{s^3 + 4.929s^2 + 20.84s - 5.463} \tag{7.19}$$

The Bode plot of measured transfer function and estimated transfer function is given in Fig. 7.6

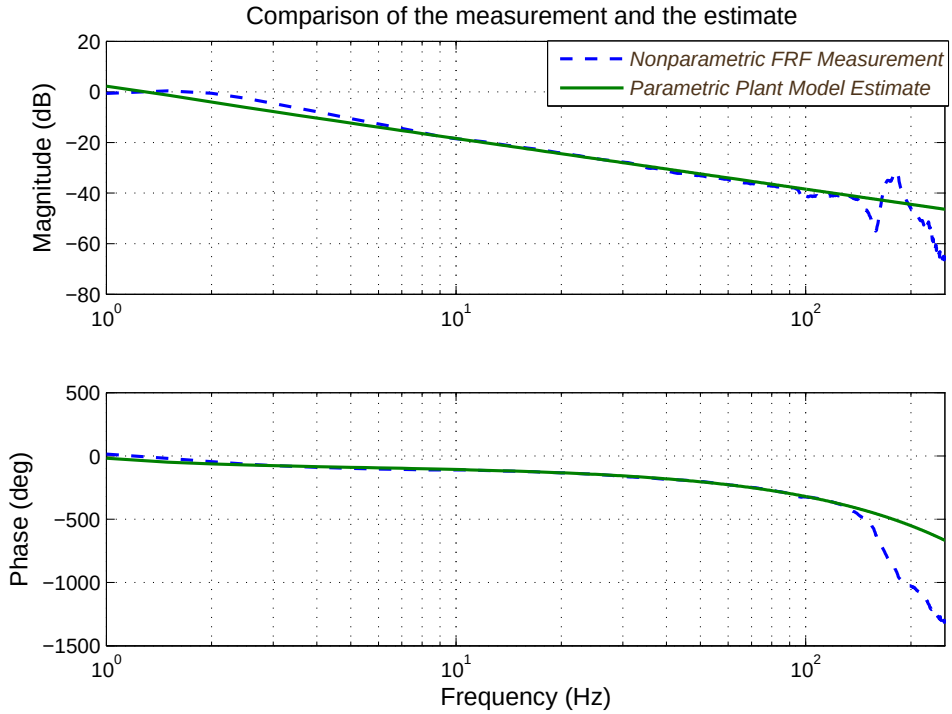

Figure 7.6: Comparison of Genetic Algorithm estimation and the measurement

The magnitude of complex residual analysis $|Y(k)/U(k) - G(\Omega_k, \hat{\theta}_{GA})|$ for the measured transfer function and estimated transfer function is given in Fig. 7.7

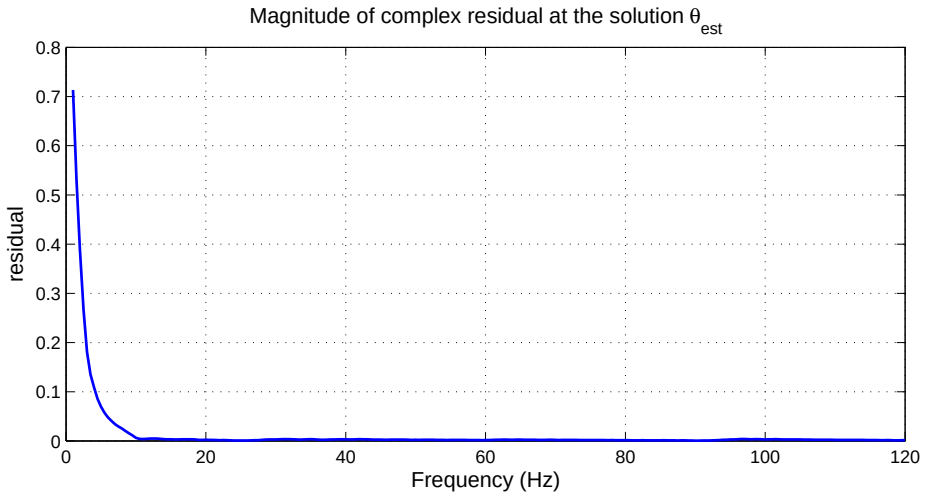

Figure 7.7: The magnitude of complex residual $|Y(k)/U(k) - G(\Omega_k, \hat{\theta}_{GA})|$ analysis of Genetic Algorithm estimation

7.7 Nonlinear Least Squares

"Nonlinear Least Squares" estimator suggested in [3, 24], does not require prior noise knowledge and performs a local minimum procedure. "Nonlinear Least Squares" (NLS) estimator $\hat{\theta}_{NLS}(Z)$ solves the problem of finding a vector θ (one of the parameter sets given in equations 6.3, 6.6 on page 79) that is a local minimizer to a function that is a sum of squares, subject to some constraints.

When "Nonlinear Least Squares" estimator minimizes the sum of the squared residuals between the measured output $Y(k)$ and the modeled output $Y(k, \theta)$ given in "output error" equation (7.4) where $G(\Omega_k, \theta)$ is one of the parametric plant models given in (6.2), (6.4), (6.5), the cost function would be:

$$V_{NLS}(\theta, Z) = \sum_{k=1}^{F} |Y(k) - Y(k, \theta)|^2 \tag{7.20}$$

When "Nonlinear Least Squares" estimator minimizes the sum of the squared residuals between the measured transfer function given in (7.2) calculated as $G(k) = Y(k)/U(k)$ and the parametric plant model $G(\Omega_k, \theta)$ that is one of the parametric plant models

given in (6.2), (6.4), (6.5), the cost function would be:

$$V_{NLS}(\theta, Z) = \sum_{k=1}^{F} |Y(k)/U(k) - G(\Omega_k, \theta)|^2 \tag{7.21}$$

The "Nonlinear Least Squares" method with the cost functions (7.20), (7.21) may converge to local minimum. Therefore, it is critical to have starting parameter sets of "sufficiently high" quality. "Iterative Weighted Linear Least Squares" solution explained in Section 7.5 is a good choice for this purpose.

The measured FRF $G(\Omega_k)$ of the system transfer function at a set of well-chosen frequencies from the multisine experiment in Subsection 4.4.2 on page 45 is used. The continuous time plant model with the time delay given in (6.4) on page 79, is identified starting from transfer function measurements (The cost function (7.21), $\Omega = s, Y(k) = G(s_k), U(k) = 1$). The parametric model that is used in cost function is a rational transfer function with delay. Increasing the complexity of the model may result in closely following noise and an unnecessarily complicated transfer function. Lowering the complexity of the model on the other hand may result in poor fit and big errors. For the experiment of interest, the number of poles chosen as $n_a = 3$ and number of zeros chosen as $n_b = 2$. The initial system delay estimate is calculated from mean slope of unwrapped phase in passband from (7.8) to be $\hat{\tau} = 0.0064$ seconds. The initial parameter set is obtained from "Iterative Weighted Linear Least Squares" solution in Section 7.5

For the experiment of interest, The "Nonlinear Least Squares" estimate results in the following transfer function:

$$\hat{G}(s_k, \theta) = e^{-0.00624s} \frac{7.358s^2 + 186.2s + 9.218}{s^3 + 22.43s^2 + 244s + 956.1} \tag{7.22}$$

The Bode plot of measured transfer function and estimated transfer function is given in Fig. 7.8

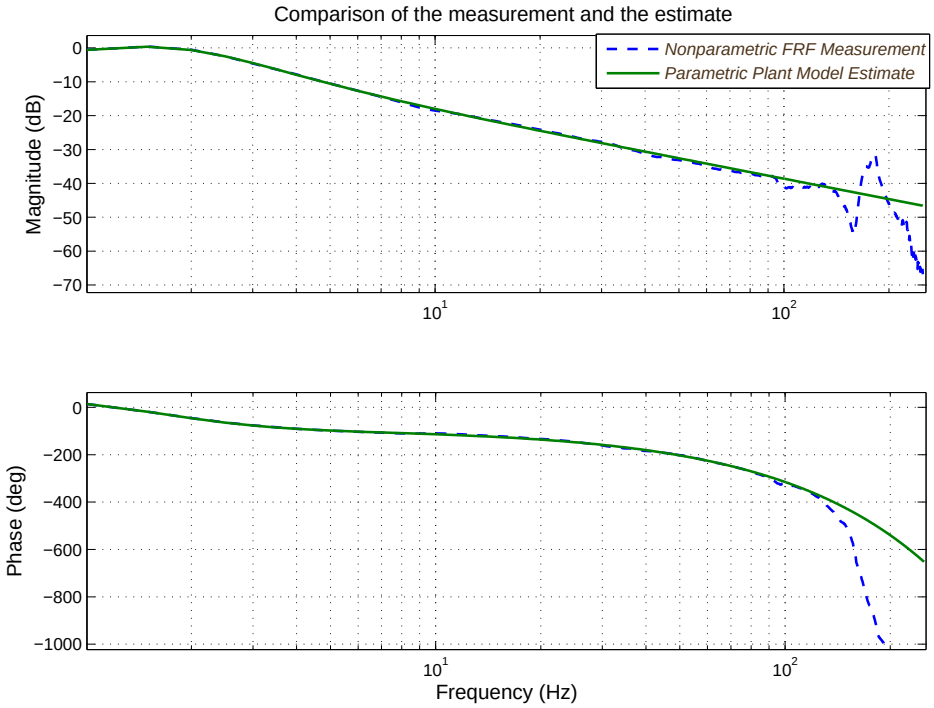

Figure 7.8: Comparison of Nonlinear Least Squares estimation and the measurement

The magnitude of complex residual analysis $|Y(k)/U(k) - G(\Omega_k, \hat{\theta}_{NLS})|$ for the measured transfer function and estimated transfer function is given in Fig. 7.9

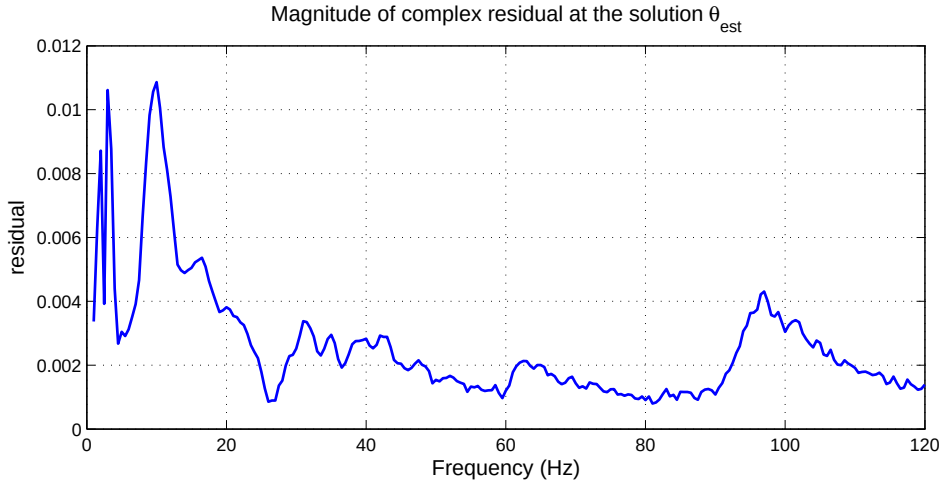

Figure 7.9: The magnitude of complex residual $|Y(k)/U(k) - G(\Omega_k, \hat{\theta}_{NLS})|$ analysis of Nonlinear Least Squares estimation

7.8 Nonlinear Logarithmic Least Squares

"Nonlinear Logarithmic Least Squares" estimator suggested in [3, 24, 26], does not require prior noise knowledge and performs a local minimum procedure. "Nonlinear Logarithmic Least Squares" (LOG) estimator $\hat{\theta}_{LOG}(Z)$ solves the problem of finding a parameter set θ that is a local minimizer to a logarithmic function that is a sum of squares, subject to some constraints.

"Nonlinear Logarithmic Least Squares" estimator is helpful when frequency response function has a large dynamic range, transfer function parameterized in powers of Ω_k (see Eqn. 6.2 on page 78) may become ill conditioned. Estimator limits the dynamic range of the frequency response function by taking the natural logarithm of the model equation $\ln(Y(k)/U(k)) = \ln(G(\Omega_k, \theta))$. That way, $\hat{\theta}_{LOG}(Z)$ improves the numerical stability and estimator is robust with respect to outliers in the measurement.

"Nonlinear Logarithmic Least Squares" estimator minimizes:

$$V_{LOG}(\theta, Z) = \sum_{k=1}^{F} |\ln(Y(k)/U(k)) - \ln(G(\Omega_k, \theta))|^2 \tag{7.23}$$

The "Nonlinear Logarithmic Least Squares" estimator with the cost function (7.23) may converge to a local minimum. Therefore, it is critical to have starting parameter sets of "sufficiently high" quality. "Iterative Weighted Linear Least Squares" solution explained in Section 7.5 is a good choice for this purpose.

Parametric plant model estimation using "Nonlinear Logarithmic Least Squares" method did not produce successful results in this study.

7.9 Maximum Likelihood

"Maximum Likelihood" estimator suggested in [3, 24], requires prior noise knowledge and performs a local minimum procedure. Prior noise knowledge is a probability density function (pdf) of the frequency domain errors $N_Z(k) = [N_Y(k) \quad N_U(k)]^T$, $k = 1, 2, \ldots, F$. The maximum likelihood estimator weights the cost function at each frequency Ω_k with its measurement uncertainty, so that high-quality FRF measure-

ments (small $\sigma_G^2(k)$) contribute more to the ML cost than poor-quality FRF measurements (large $\sigma_G^2(k)$). Hence, the ML estimator trusts more to accurate measurements while it rejects noisy measurements [3].

The maximum likelihood (ML) cost function is

$$V_{ML}(\theta, Z) = \sum_{k=1}^{F} \frac{|e(\Omega_k, \theta, Z(k))|^2}{\sigma_e^2(\Omega_k, \theta)} \tag{7.24}$$

In (7.24), $e(\Omega_k, \theta, Z(k))$ stands for the "equation error" given in (7.6) and $\sigma_e^2(\Omega_k, \theta)$ is the variance of equation error

$$\sigma_e^2(\Omega_k, \theta) = \sigma_Y^2(k)|A(\Omega_k, \theta)|^2 + \sigma_U^2(k)|B(\Omega_k, \theta)|^2 - 2\mathrm{Re}(\sigma_{YU}^2(k)A(\Omega_k, \theta)\bar{B}(\Omega_k, \theta)) \tag{7.25}$$

Dividing the numerator and denominator of each term in the sum (7.24) by $|A(\Omega_k, \theta)|^2$ gives another representation of maximum likelihood cost function:

$$V_{ML}(\theta, Z) = \sum_{k=1}^{F} \frac{|Y(k) - Y(k, \theta)|^2}{\sigma_Y^2(\Omega_k, \theta)} \tag{7.26}$$

Here, $Y(k) - Y(k, \theta)$ is the output error given in (7.4) and $\sigma_Y^2(\Omega_k, \theta)$ is the variance of output error:

$$\sigma_Y^2(\Omega_k, \theta) = \sigma_Y^2(k) + \sigma_U^2(k)|G(\Omega_k, \theta)|^2 - 2\mathrm{Re}(\sigma_{YU}^2(k)\bar{G}(\Omega_k, \theta)) \tag{7.27}$$

Transfer function representation of maximum likelihood cost function (ML) is given by

$$V_{ML}(\theta, Z) = \sum_{k=1}^{F} \frac{|Y(k)/U(k) - G(\Omega_k, \theta)|^2}{\sigma_G^2(k)} \tag{7.28}$$

The weighted least squares distance between the measurement and the model is minimized. $\sigma_G^2(k)$ is the variance (or uncertainty) of transfer function measurement:

$$\sigma_G^2(k) = |G_0(\Omega_k)|^2[\sigma_Y^2(k)/|Y_0(k)|^2 + \sigma_U^2(k)/|U_0(k)|^2 - 2\mathrm{Re}(\sigma_{YU}^2(k)/(Y_0(k)\bar{U}_0(k)))] \tag{7.29}$$

The "Maximum Likelihood" method with the cost functions (7.24), (7.26), (7.28) may converge to local minimum. Therefore, it is critical to have starting parameter sets of "sufficiently high" quality. "Iterative Weighted Linear Least Squares" estimator explained in Section 7.5 is a good candidate for this purpose.

The measured FRF $G(\Omega_k)$ of the system transfer function, input signal frequency spectrum $U(k)$ and nonparametric noise model $\sigma_Y^2(k) = var(N_Y(k))$ at a set of well-chosen frequencies from the multisine experiment in Subsection 4.4.2 on page 45 is used. The continuous time plant model with the time delay given in (6.4) on page 79 is identified starting from transfer function measurements. The cost function is given in (7.28). System is identified in continuous domain $\Omega = s$. Since the input signal $U_0(k)$ is known exactly, $\sigma_U^2(k) = 0$, $\sigma_{YU}^2(k) = 0$, as can be verified from Figures 4.6 and 4.8 on page 47. Therefore Eqn. (7.29) simplifies to $\sigma_G^2(k) = \sigma_Y^2(k)/|U_0(k)|^2$ where $U_0(k) = U(k)$. Output noise variance $\sigma_Y^2(k)$ for this experiment can be examined in Fig. 4.7 on page 47. The parametric model that is used in cost function is a rational transfer function with delay. Increasing the complexity of the model may result in closely following noise and an unnecessarily complicated transfer function. Lowering the complexity of the model on the other hand may result in poor fit and big errors. For the experiment of interest, the number of poles chosen as $n_a = 3$ and number of zeros chosen as $n_b = 2$. The initial system delay estimate is calculated from mean slope of unwrapped phase in passband from Eqn. (7.8) to be $\hat{\tau} = 0.0064$ seconds. The initial parameter set is obtained from "Iterative Weighted Linear Least Squares" solution in Section 7.5

For the experiment of interest, The "Maximum Likelihood" estimate results in the following transfer function:

$$\hat{G}(s_k, \theta) = e^{-0.00543s} \frac{-3.132\mathrm{e}-05s^2 + 7617s + 8.768\mathrm{e}04}{s^3 + 1027s^2 + 1.153\mathrm{e}04s + 1.735\mathrm{e}05} \tag{7.30}$$

The Bode plot of measured transfer function and estimated transfer function is given

in Fig. 7.10

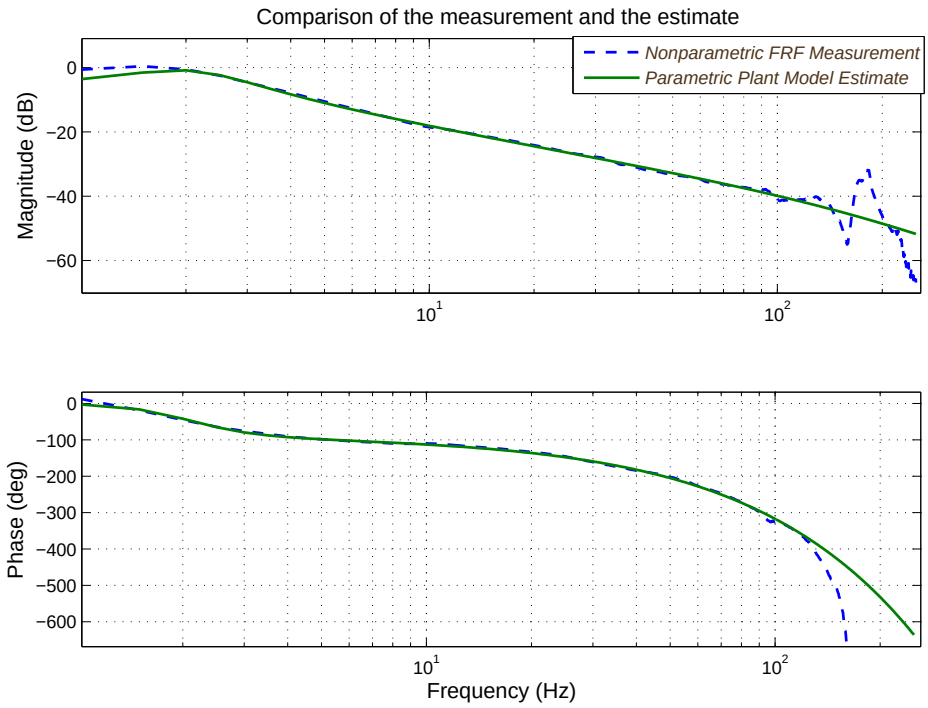

Figure 7.10: Comparison of Maximum Likelihood estimation and the measurement

The magnitude of complex residual analysis $|Y(k)/U(k) - G(\Omega_k, \hat{\theta}_{ML})|$ for the measured transfer function and estimated transfer function is given in Fig. 7.11

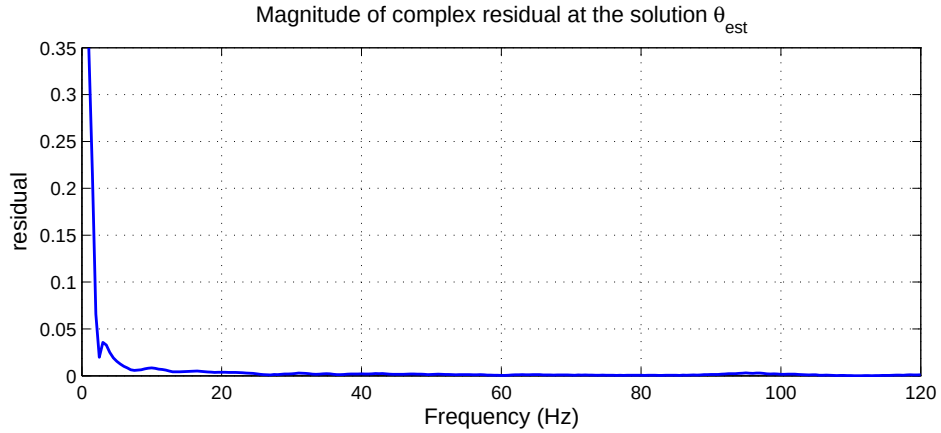

Figure 7.11: The magnitude of complex residual $|Y(k)/U(k) - G(\Omega_k, \hat{\theta}_{ML})|$ analysis of Maximum Likelihood estimation

7.10 Comparisons of Estimates

In system identification, a global minimization procedure is an advantageous property since there might exist many local minimums. It is shown that “Linear Least Squares” (LS), “Iterative Weighted Linear Least Squares” (IWLS) and “Genetic Algorithm” (GA) estimators are self starting (do not necessitate good starting points) and sustain global minimization property. Therefore, the solutions of these estimators can be used as reliable starting values. “Nonlinear Least Squares” (NLS), “Nonlinear Logarithmic Least Squares” (LOG) and “Maximum Likelihood” (ML) estimators are efficient local minimum algorithms which require good initial estimates.

In Fig. 7.12, the frequency responses of measurement (dashed line) and LS, IWLS, GA, NLS, ML parametric model estimates (solid lines) are compared on a Bode plot. In Fig. 7.13, on top, the difference between the estimated parametric model amplitude in dB and the measured amplitude in dB is given. A positive difference of 6 dB in magnitude means that estimated parametric model magnitude is twice the magnitude of measurement. In Fig. 7.13, on below, the difference between the estimated parametric model phase and the measured phase in degree is given. In Fig. 7.14 measured FRF amplitude (dashed line) and absolute value of the complex error between the estimated parametric plant model and measured FRF are given. For instance, a negative difference of -26dB between the dashed line and solid line corresponds to 5% estimate error.

Figures 7.13 and 7.14 show that the LS estimator is poor in the low-frequency range (this is discussed in Section 7.4). LS IWLS and GA have a big advantage as global minimizers and as self starting algorithms, but their efficiency can be low and computationally slower. NLS and ML estimators use the IWLS solution as a starting point. NLS estimator result is pretty successful and fits the FRF measurement very well. On the other hand, ML estimator weights the residuals according to the nonparametric noise model. Therefore ML estimator has better statistical properties than NLS estimate.

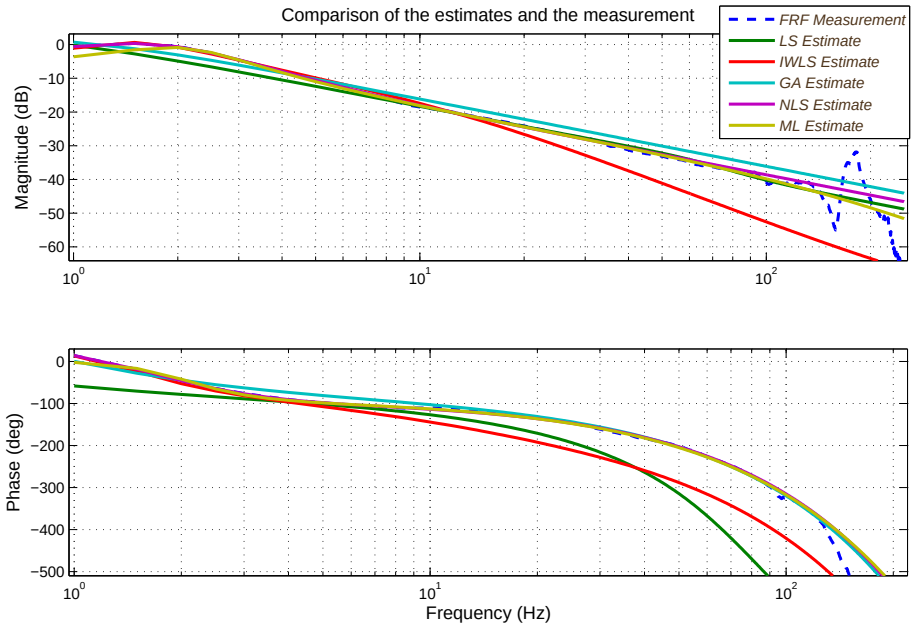

Figure 7.12: Comparisons of the LS, IWLS, NLS, ML solutions and the measurement

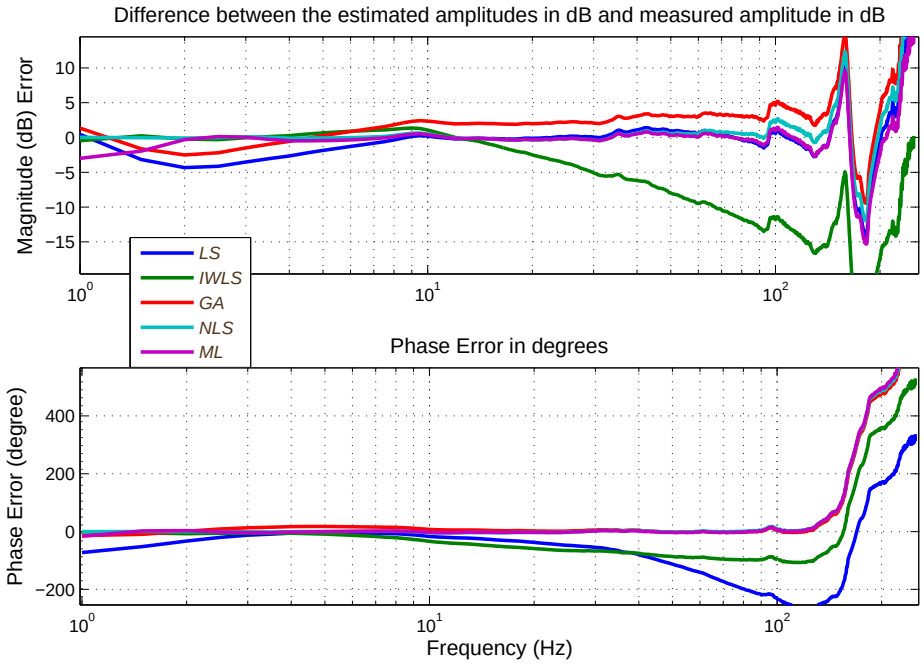

Figure 7.13: On top: difference between the estimated amplitude in dB and measured amplitude in dB. Below: phase error in degrees.

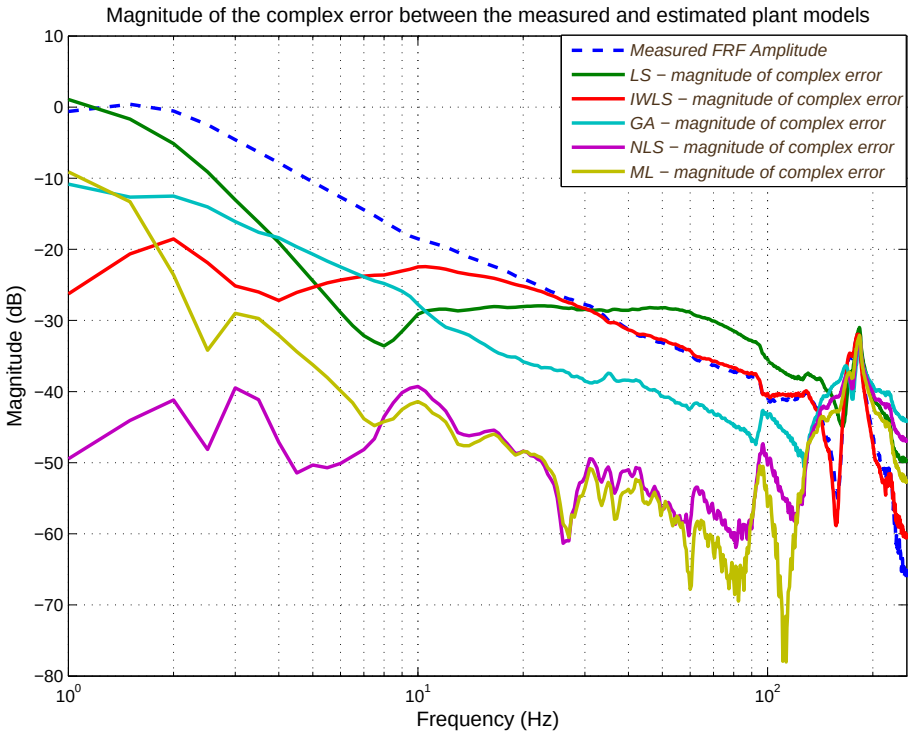

Figure 7.14: Measured plant model amplitude (dashed line) and magnitude of the complex error between the estimated plant model and measured FRF.

7.11 Model Selection and Validation

The system identification can be described as an iterative process. Increasing the complexity of the model may result in closely following noise and unnecessarily complicated transfer function. On the other hand, lowering the complexity of the model may result in poor fit and systematic errors. A control engineer searches for a parametric plant model which best describes the system with minimum complexity (minimum order). In the first trial, the order of transfer function can be chosen small. After an optimization procedure, the estimated plant model and the measured FRF are compared by a visual inspection on a Bode plot or by residual analysis. This comparison step is called “Validation”. If the estimated transfer function satisfactorily describe the dynamic system, identification problem is solved. Otherwise (abnormalities, large errors exist in some frequency bands), the order of transfer function (parametric plant model) is gradually increased until a satisfactory parametric model

is obtained. Model order is increased step-by-step until systematic errors are below an acceptable level. The acceptance level can be determined according to intended application requirements. In this study, the parametric model is intended to be used in a controller design.

In this section, four parametric model estimation is realized. The first parametric model possesses $n_a = 1$ number of poles and $n_b = 0$ number of zeros. The second parametric model has $n_a = 3$ and $n_b = 2$. The third parametric model obtains $n_a = 6$ and $n_b = 5$. The fourth parametric model contains $n_a = 9$ and $n_b = 8$. The whole measured frequency range, 1-250 Hz, is taken into account in the optimization problem. ML estimator is used in the optimization algorithm with starting point coming from IWLS. Note that, as the order of model or number of frequency lines increases, the computational time of the optimization problem grows. The Bode plot of the measured transfer function and the estimated transfer function is given in Fig. 7.10. In Fig. 7.16, it is shown how the systematic errors decrease as the parametric model order is increased. In Fig. 7.16 measured FRF amplitude (dashed line) and absolute value of the complex error between the estimated parametric plant model and measured FRF are given. For instance, a negative difference of -26dB between the dashed line and solid line corresponds to 5% estimate error.

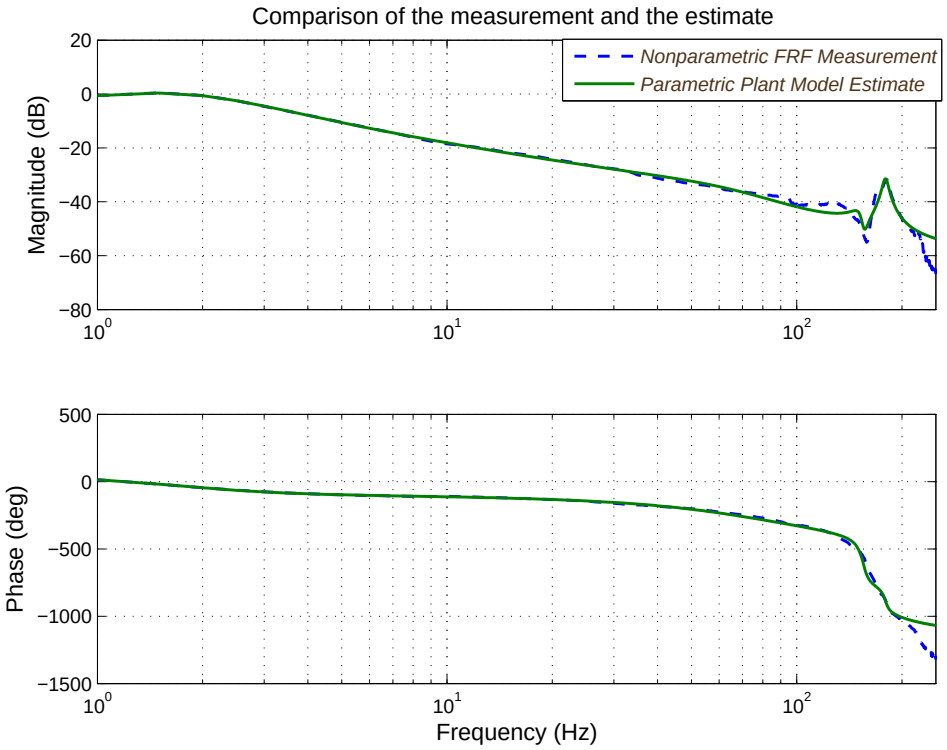

Figure 7.15: Comparison of high order ($n_a = 9$, $n_b = 8$) parametric model estimation and the measurement

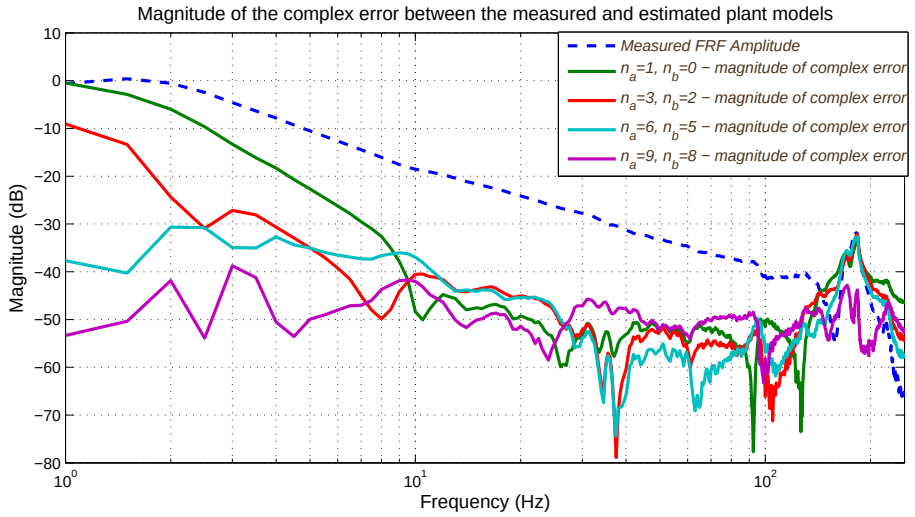

Figure 7.16: Measured plant model amplitude (dashed line) and magnitude of the complex error between the estimated plant model and measured FRF.

CHAPTER 8

DISCUSSION, CONCLUSION AND FUTURE WORK

8.1 Discussion and Conclusion

In this study, the inner azimuth gimbal of four axis gyro stabilized IR/EO gimbal system is modeled step by step in the frequency domain through experimental investigation and the results of this investigation are presented. Various excitation signals and algorithms are studied in order to efficiently measure nonparametric FRF and its uncertainty. The level of nonlinear distortions in the FRF measurement is quantified. A large number of identification techniques are applied and parametric plant model is estimated. The field of system identification takes a fundamental place in control engineering. The estimated parametric plant model allows the control engineer to realize time domain simulations, frequency domain analyses, controller design, stability analysis and prediction.

System identification is an iterative process. When starting the identification, a priori information about the plant is usually limited. At each iteration, the excitation signal is redesigned using the simulations of new and better estimated parametric plant model. For excitation signals, signal to noise ratio (SNR) is a very critical property. In all experiments, the desired signal to be measured is disturbed by undesired background noise. In frequency response function measurements, the time it takes to reach a specified accuracy is inversely proportional to the square of SNR [2, 3]. Even worse than that, in some cases, low SNR would introduce bias errors in frequency response function measurements which can not be compensated by increasing measurement time. By averaging the measurements, the random errors can be reduced, but systematic bias

errors will remain. Therefore, a good excitation signal should provide as high power spectrum as possible without exceeding normal operation conditions. It is desired to inject more power to frequency bands where noise is dominant so that roughly constant SNR in FRF measurement is obtained. General purpose excitation signals are able to excite the system with an almost flat power spectrum in a frequency range of interest. Therefore, general purpose excitation signals are good for a dynamic system with a white noise behavior. At first data collection experiment where a priori information about the plant is limited, one of the periodic general purpose excitation signal can be used. After obtaining the nonparametric noise model of the system, excitation signal can be improved by shaping the magnitude spectrum of multisine signal and inject more power to the noisy frequency bands. Furthermore, it is advised to optimize the phases of multisine excitation signal to achieve enhanced signals while satisfying application specific restrictions (see Section 3.8).

It is crucial that experiments are well designed so that parameters to be estimated through statistical methods result in least possible bias and minimum variance. In this study, various perturbation signals are analyzed and compared. The knowledge and practical experiences are shared about under what conditions broadband excitation signal is superior to stepped sine excitation signal in terms of measurement time to reach a specified accuracy. When input signal is periodic, by averaging techniques, it is possible to reduce the variance of frequency response function measurement and decrease the error. Moreover, the averaging in the frequency domain provides the nonparametric noise model of the system which is not available with averaging methods in the time domain. It is important that no spectral leakage occurs during the analysis of the measurements; therefore periodic excitation signals should be preferred and an integer number of signal periods should be measured.

All mechanical systems are inherently nonlinear in nature. However, nonlinear model building is difficult to accomplish and time consuming while profits are usually small. For this reason, it is appealing to select linear mathematical models around operating points. On the other hand, knowing the nonlinear distortion error contribution on the frequency response function measurement helps the robust controller designer to set the uncertainty bounds on a linear model and improve the existing controller. In this study, experimental illustrations of nonlinear distortion quantification techniques

are given, summarizing their advantages and drawbacks. A robust method to detect and quantify nonlinear distortion on frequency response functions measurements is studied.

The main aim of this study is the estimation of parametric models from nonparametric frequency response function measurements. Various optimization techniques are implemented in order to find a parametric plant model which best represents the dynamic system. The performances of the implemented identification techniques are compared in terms of their efficiencies, convergence properties and bias errors. The problem of parametric plant modeling is quite sensitive to local minimums since parameter set appears both in numerator and denominator of the transfer function. Initial time delay value is also critical in this sense. Therefore, self-starting global optimization algorithms are necessary in order to avoid local minimums. It turns out that "Iterative Weighted Linear Least Squares" (IWLS) estimator provides globally good results without converging local minimums. IWLS estimator is a self-starting algorithm which does not require a good initial point. The result of IWLS estimator can be used as a starting point of other computationally more efficient estimators. The nonparametric noise model obtained in previous steps is invaluable, because, this information allows the estimator to weight the cost function and attain statistically better results (see "Maximum Likelihood" estimator in Section 7.9). In validation step, estimated plant model and nonparametric frequency response function measurement are compared by a visual inspection on a Bode plot and by residual analysis. If any abnormalities are detected, model order can be increased or previous steps can be redesigned. Eventually, the engineer looks for a parametric plant model which best describes the system with minimum complexity (minimum order).

8.2 Publications

The following paper is published and presented in SAVTEK 2014 Ankara.

> Gökhan Özdoğan and Kemal Leblebicioğlu, "Cayro Stabilize Dört Eksen Gimbal Yapılı Elektro Optik Sistemin Modellenmesi", in 7. Savunma Teknolojileri Kongresi, pp. 1061-1072, 2014.

The following paper is accepted to be presented in TOK, in September 2014, Kocaeli.

> Gökhan Özdoğan and Kemal Leblebicioğlu, "Gyro Stabilize Gimbalin Frekans Bölgesinde Modellenmesi ve Analizi", in Otomatik Kontrol Ulusal Toplantısı, 2014.

8.3 Future Work

Although all the experiments are realized using gyro stabilized gimbal system, the measurement techniques explained and identification methods discussed in this study are applicable to all SISO dynamic systems operating in open loop. The algorithm implementations built and programmed in this study will be organized and composed in a single application with a graphical user interface. The author intends to release this application later as a MATLAB toolbox.

As extensions of this study, the following future work will be researched.

- The algorithms studied in this work are applicable only to SISO systems. However, some complex dynamic systems should be modeled as MIMO due to significant coupling effects. As a future study, MIMO system identification will be studied.
- In this study, a dynamic system operating in open loop is handled (direct identification). However, some systems have to be run under linear feedback control. The closed loop identification (indirect identification) can be required due to several reasons. This may be due to safety reasons, an unstable plant that requires control or the plant may contain inherent feedback mechanisms (biological systems). For instance, when the plant is unstable, it is first required to be stabilized with a closed loop controller. Then the FRF of closed loop system can be measured. Since the implemented controller is known exactly, the FRF of unstable plant can be derived from the closed loop FRF measurement. As a future study, the system identification of closed loop systems will be studied.
- Estimating the best linear approximated parametric plant model of a highly nonlinear system is difficult. In order to reduce the systematic errors, the order of

parametric model is required to be very high. The concept of modeling a highly nonlinear system with a combination of several linear low order parametric models active in separate frequency bands will be researched. This is also called piecewise linear modeling.

REFERENCES

[1] M. Verhaegen and V. Verdult, *Filtering and system identification: a least squares approach*. Cambridge university press, 2007.

[2] J. Schoukens, R. Pintelon, E. Van Der Ouderaa, and J. Renneboog, "Survey of excitation signals for fft based signal analyzers," *Instrumentation and Measurement, IEEE Transactions on*, vol. 37, no. 3, pp. 342–352, 1988.

[3] R. Pintelon and J. Schoukens, *System identification: A frequency domain approach*. Wiley. com, 2 ed., 2012.

[4] P. Guillaume, R. Pintelon, and J. Schoukens, "On the use of signals with a constant signal-to-noise ratio in the frequency domain," *Instrumentation and Measurement, IEEE Transactions on*, vol. 39, no. 6, pp. 835–842, 1990.

[5] A. V. Oppenheim, R. W. Schafer, J. R. Buck, *et al.*, *Discrete-time signal processing*, vol. 2. Prentice-hall Englewood Cliffs, 1989.

[6] J. Schoukens, Y. Rolain, and R. Pintelon, "Leakage reduction in frequency-response function measurements," *IEEE transactions on instrumentation and measurement*, vol. 55, no. 6, pp. 2282–2287, 2006.

[7] J. Schoukens, R. M. Pintelon, and Y. J. Rolain, "Broadband versus stepped sine frf measurements," *Instrumentation and Measurement, IEEE Transactions on*, vol. 49, no. 2, pp. 275–278, 2000.

[8] E. Van Der Ouderaa, J. Schoukens, and J. Renneboog, "Peak factor minimization using a time-frequency domain swapping algorithm," *Instrumentation and Measurement, IEEE Transactions on*, vol. 37, pp. 145–147, 1988.

[9] P. Guillaume, J. Schoukens, R. Pintelon, and I. Kollar, "Crest-factor minimization using nonlinear chebyshev approximation methods," *Instrumentation and Measurement, IEEE Transactions on*, vol. 40, no. 6, pp. 982–989, 1991.

[10] G. Simon and J. Schoukens, "Robust broadband periodic excitation design," *Instrumentation and Measurement, IEEE Transactions on*, vol. 49, no. 2, pp. 270–274, 2000.

[11] R. Pintelon, Y. Rolain, and W. Van Moer, "Probability density function for frequency response function measurements using periodic signals," in *Instrumentation and Measurement Technology Conference, 2002. IMTC/2002. Proceedings of the 19th IEEE*, vol. 2, pp. 869–874, IEEE, 2002.

[12] J. Schoukens, R. Pintelon, and J. Renneboog, "A maximum likelihood estimator for linear and nonlinear systems-a practical application of estimation techniques in measurement problems," *Instrumentation and Measurement, IEEE Transactions on*, vol. 37, no. 1, pp. 10–17, 1988.

[13] K. Vanhoenacker, J. Schoukens, J. Swevers, and D. Vaes, "Summary and comparing overview of techniques for the detection of non-linear distortions," in *Proceedings of the International Conference on Noise and Vibration Engineering*, pp. 1241–1256, 2002.

[14] K. Worden and G. R. Tomlinson, *Nonlinearity in structural dynamics: detection, identification and modelling*. CRC Press, 2000.

[15] K. Vanhoenacker, T. Dobrowiecki, and J. Schoukens, "Design of multisine excitations to characterize the nonlinear distortions during frf-measurements," *Instrumentation and Measurement, IEEE Transactions on*, vol. 50, no. 5, pp. 1097–1102, 2001.

[16] J. Schoukens, R. Pintelon, and T. Dobrowiecki, "Linear modelling in the presence of nonlinear distortions," in *Instrumentation and Measurement Technology Conference, 2001. IMTC 2001. Proceedings of the 18th IEEE*, vol. 2, pp. 1332–1338, IEEE, 2001.

[17] R. Pintelon, J. Schoukens, W. Van Moer, and Y. Rolain, "Identification of linear systems in the presence of nonlinear distortions," *Instrumentation and Measurement, IEEE Transactions on*, vol. 50, no. 4, pp. 855–863, 2001.

[18] J. Schoukens, T. Dobrowiecki, and R. Pintelon, "Parametric and nonparametric identification of linear systems in the presence of nonlinear distortions-a frequency domain approach," *Automatic Control, IEEE Transactions on*, vol. 43, no. 2, pp. 176–190, 1998.

[19] J. Schoukens, R. Pintelon, Y. Rolain, and T. Dobrowiecki, "Frequency response function measurements in the presence of nonlinear distortions. a general framework and practical advises," in *Proceedings of the International Seminar on Modal Analysis*, vol. 1, pp. 459–464, Citeseer, 2001.

[20] J. Schoukens, J. Lataire, R. Pintelon, G. Vandersteen, and T. Dobrowiecki, "Robustness issues of the best linear approximation of a nonlinear system," *Instrumentation and Measurement, IEEE Transactions on*, vol. 58, no. 5, pp. 1737–1745, 2009.

[21] T. D'haene, R. Pintelon, J. Schoukens, and E. Van Gheem, "Variance analysis of frequency response function measurements using periodic excitations," *Instrumentation and Measurement, IEEE Transactions on*, vol. 54, no. 4, pp. 1452–1456, 2005.

[22] J. Schoukens, R. Pintelon, G. Vandersteen, and P. Guillaume, "Frequency-domain system identification using non-parametric noise models estimated from a small number of data sets," *Automatica*, vol. 33, no. 6, pp. 1073–1086, 1997.

[23] Y. Rolain, J. Schoukens, and R. Pintelon, "Order estimation for linear time-invariant systems using frequency domain identification methods," *Automatic Control, IEEE Transactions on*, vol. 42, no. 10, pp. 1408–1417, 1997.

[24] R. Pintelon, P. Guillaume, Y. Rolain, J. Schoukens, and H. Van Hamme, "Parametric identification of transfer functions in the frequency domain-a survey," *Automatic Control, IEEE Transactions on*, vol. 39, no. 11, pp. 2245–2260, 1994.

[25] Z. Michalewicz, *Genetic algorithms+ data structures= evolution programs*. springer, 1996.

[26] P. Guillaume, R. Pintelon, and J. Schoukens, "Robust parametric transfer function estimation using complex logarithmic frequency response data," *Automatic Control, IEEE Transactions on*, vol. 40, no. 7, pp. 1180–1190, 1995.